

POLITECNICO DI TORINO
MASTER'S DEGREE IN AEROSPACE ENGINEERING



Thermomechanical calibration of FBG
sensors integrated in aerospace structures

Author:
Gianluca ALLERUZZO

Supervisors:
Prof. Paolo MAGGIORE
Ing. Matteo DALLA VEDOVA
Ing. Alessandro AIMASSO

July 2022

Contents

1	Introduction	3
1.1	RA prototype aircraft	3
1.1.1	Thermomechanical decoupling on RA	5
1.2	Scope and purpose of this thesis	6
2	Optical fibers and FBG sensors	7
2.1	Optical Fibers	7
2.1.1	Working principles	8
2.2	FBG sensors	9
2.2.1	FBG as Mechanical strain and Temperature sensors	11
2.2.2	Thermal compensation techniques	12
3	The experimental test bench	17
3.1	Samples preparation	17
3.1.1	Specimen 1	18
3.1.2	Specimen 2	20
3.2	Climatic chamber	22
3.3	Temperature acquisition	23
3.4	FBG data acquisition	24
3.5	Data post-processing	26
4	Experimental campaign	29
4.1	A simple digital-optical system	31
4.1.1	Thermal characterisation [0 40]°C	31
4.1.2	Bending test at constant temperature	36
4.1.3	Bending test at variable temperature (30°C/h)	40
4.1.4	Bending test at variable temperature (60°C/h)	44
4.1.5	Thermal characterisation [-40 40]°C	47
4.1.6	Determination of K_ϵ and $\Delta\epsilon$	49
4.2	Two independents optical systems	58

CONTENTS

4.2.1	Thermal characterisation [0 40]°C	58
4.2.2	Bending test at variable temperature (45°C/h)	63
4.3	A unique fully-autonomous optical system	69
4.3.1	Determination of K_ε and $\Delta\varepsilon$	70
4.3.2	Bending test at variable temperature (20°C/h)	79
5	Conclusions	85
5.1	Possible improvements and future works	86
5.1.1	A new fully-optical system	86
5.1.2	An improved mechanical calibration phase	86
A	Arduino - SHT85 temperature sketch	89
B	Thermomechanical decoupling using an inaccurate thermal characterization	93

List of Figures

1.1	RA aircraft	3
1.2	FBG sensors arrangement on RA [4],[5]	4
1.3	Thermomechanical decoupling plate [4], [5]	5
1.4	Cantilever beam with decoupling plate	5
2.1	Architecture of an optical fiber [6]	8
2.2	Snell's law	8
2.3	Signal propagation within an optical fiber	9
2.4	FBG working mechanism [1]	10
2.5	Two FBG embedded in a glass tube	13
2.6	Two FBGs embedded in a composite structure	13
2.7	FBG inside a liquid-crystalline polymer tube	14
2.8	Overlapping of two FBGs [3]	14
3.1	Specimen 1, bonding phase: step 1 to 3	18
3.2	Linear translator	18
3.3	Specimen 1	19
3.4	Representation of Specimen 2	20
3.5	FBGs location on specimen 2	21
3.6	KK-50 CHLT [11]	22
3.7	Arduino UNO - SHT85 connection diagram [12]	23
3.8	SmartScan optical interrogator [13]	24
3.9	SmartScan connections [13]	25
3.10	Smartfibres main screen [13]	26
3.11	SmartScan output file	27
4.1	Specimen 1 setup for thermal characterization	32
4.2	λ -time for T.C. of specimen 1 between [0 40]°C	33
4.3	λ -temperature for T.C. of specimen 1 between [0 40]°C	33
4.4	Comparison between SHT85 and FBG for specimen 1	35
4.5	Representation of the bending test for specimen 1	36

LIST OF FIGURES

4.6	λ-time for bending test at constant temperature	37
4.7	Specimen oscillation when applying a load	38
4.8	λ-load for bending test at constant temperature	38
4.9	Climatic chamber setup for bending test	40
4.10	λ-time-load evolution for bending test at 30°C/h	41
4.11	λ-time-T evolution for bending test at 30°C/h	42
4.12	Thermal compensation for 30°C/h load test	43
4.13	λ-time-load evolution for bending test at 60°C/h	45
4.14	λ-time-T evolution for bending test at 60°C/h	45
4.15	Thermal compensation for 60°C/h load test	46
4.16	λ-time T.C. Specimen1 [-40 40]°C	47
4.17	λ-Temperature T.C. Specimen1 [-40 40]°C	48
4.18	An example of strain gauge [14]	49
4.19	Strain Gauge configuration on Specimen 1	50
4.20	Specimen1 setup for bending test with strain gauge	51
4.21	λ-time trend for bending test	52
4.22	Specimen1: correlation between $\Delta\lambda_\epsilon$ and $\Delta\epsilon$	52
4.23	$\Delta\lambda_\epsilon$ -load- $\Delta\epsilon$ trend for bending test	53
4.24	Specimen 1: $\Delta\epsilon$ -time FBG vs SG	54
4.25	Specimen1: Overall strain comparison	55
4.26	Specimen 2 setup for thermal characterization	59
4.27	Specimen2 FBGs numbering	60
4.28	Specimen2 Channel 1 λ-Temperature	61
4.29	Specimen2 Channel 2 λ-Temperature	61
4.30	Specimen2 SHT85 vs FBG	62
4.31	Climatic chamber setup for bending test	63
4.32	λ-time-load evolution for bending test at 45°C/h	64
4.33	λ-time-T evolution for bending test at 45°C/h	65
4.34	Temperature comparison: FBGs vs SHT85	66
4.35	Thermal compensation: channel 1	67
4.36	Thermal compensation: channel 2	68
4.37	Strain Gauge configuration on Specimen 2	71
4.38	Specimen2 setup for bending test with strain gauge	72
4.39	Specimen2 FBGs numbering	72
4.40	Specimen 2: Ch1Gr1 λ-time trend	73
4.41	Specimen 2: Ch2Gr2 λ-time trend	73
4.42	Ch1Gr1: correlation between $\Delta\lambda_\epsilon$ and $\Delta\epsilon$	74
4.43	Ch2Gr2: correlation between $\Delta\lambda_\epsilon$ and $\Delta\epsilon$	75
4.44	K_ϵ vs pre-load trend for both Specimens	76
4.45	$\Delta\lambda_\epsilon$ -load- $\Delta\epsilon$ trend for Specimen2	77

LIST OF FIGURES

4.46	Specimen 2: overall strain comparison	78
4.47	Climatic chamber setup for bending test	79
4.48	λ/λ_{mean} - time - temperature evolution	81
4.49	λ/λ_{mean} - time - load evolution	81
4.50	Temperature comparison: FBGs vs SHT85	82
4.51	FBGs mechanical strain time-evolution	83
5.1	Fully-optical system improvement	86
B.1	Specimen 2 setup for thermal characterization	94
B.2	Specimen2 Channel 1 λ -Temperature	95
B.3	Specimen2 Channel 2 λ -Temperature	95
B.4	Specimen2 SHT85 vs FBG	96
B.5	Temperature comparison: FBGs vs SHT85	97
B.6	Thermal compensation: channel 1	98
B.7	Thermal compensation: channel 2	98

List of Tables

2.1	Characteristics of not glued FBG [2]	12
3.1	Tenax UTS50 Properties [5]	17
3.2	FBG characteristics of Specimen 1	19
3.3	FBGs characteristics of Specimen 2	20
3.4	Climatic chamber characteristics	22
3.5	SmartScan characteristics [13]	24
4.1	Specimen 1 T.C. between 0°C and +40°C	34
4.2	Characteristics of Specimen 1 bending test (30°/h)	41
4.3	Characteristics of Specimen 1 bending test (60°/h)	44
4.4	Specimen 1 T.C. between -40°C and +40°C	47
4.5	Specimen 1: comparison between mechanical strain	56
4.6	Specimen 1: K_ϵ comparison	56
4.7	Specimen 2: T.C. [0 40]°C	62
4.8	Characteristics of Specimen 1 bending test (30°/h)	64
4.9	Temperature comparison: RMSE	66
4.10	Specimen 2: K_ϵ and $\Delta\lambda_{\epsilon,0}$	75
4.11	Specimen 2: comparison between mechanical strain	78
4.12	Characteristics of Specimen 1 bending test (20°/h)	80
B.1	Specimen 2: T.C. [-40 40]°C	96
B.2	Temperature comparison: RMSE	97

Abstract

Optical fibers have found widespread use in a multitude of areas over the last decades. Their main application field is communication, but they are gaining interest and their implementation is spreading even in the medical sector, as well as the infrastructure and engineering. Other than being utilized for signal transmission, optical fibers can also be used to house specific types of sensors, such as *Fiber Bragg Grating (FBG) sensors*. This type of sensor is capable of reflecting a wavelength, known as *Bragg wavelength*, which can be influenced by the physical deformations of the sensor itself and by variations in ambient conditions, allowing FBGs to be used for the measurement of deformations, vibrations, temperature and humidity variations. These features, combined with their reduced size and weight, insensitivity to electromagnetic interference, and the possibility of being easily integrated into composite structures, make them great candidates as sensing elements also for aerospace applications. The investigation of the behavior of FBGs integrated in composite material structures as temperature and mechanical strain sensors is the main subject of this work. The activity discussed in this project starts with the experimental determination of the K_T and K_ε coefficients of the sensors. Then, in order to isolate the thermal effects from the mechanical ones, alternative approaches in this regard will be proposed and experimentally tested. The issue of thermal decoupling is addressed, first, using a hybrid system of digital and optical sensors, then with an intermediate solution composed by two optical-only systems, mechanically decoupled from each other, and lastly, a single, completely autonomous optical configuration is analysed. Finally, the experimental results will be compared to reference values to verify the validity and practical application possibilities of FBGs adopting such thermal decoupling methodologies.

Chapter 1

Introduction

1.1 RA prototype aircraft

In a world that is moving to the zero-emissions target, decarbonization became a priority in every industry, including aerospace. Many strategies can be used to achieve this goal in aeronautics, but one of the most promising is certainly the development of All-Electric Aircrafts (AEA).

Within the ICARUS Polito student team, at the Polytechnic of Turin, the RA project was born with the goal of creating a completely autonomous aircraft (UAV) powered by solar energy only, characterized by unlimited autonomy and capable of crossing the Atlantic Ocean.



Figure 1.1: RA aircraft

General features		Wing parameters	
Cruise speed	15 m/s	Wing surface	1.484 m ²
MTOW	15 kg	Aspect ratio	16.8
Max ROC	1 m/s	Wingspan	5 m
Max Efficiency	25.8	Root chord	0.372 m
Min battery autonomy	3h	Tip chord	0.146
Solar panel surface	0.796 m ²	Angle of incidence	3°

The prototypical nature of RA makes it particularly suitable as an experimental platform for innovative and under-development technologies.

Among these, the prototype was equipped with Fiber Bragg Grating (FBG) optical sensors, which would allow real-time monitoring of the deformation state and temperature of the structure, providing useful information for both diagnostic and prognostic purposes.

In the present case, the aircraft left half-wing was equipped with 3 optical fibers lines, each including 3 FBG sensors equally spaced with each other, as shown in Figure 1.2. This process of sensorisation the aircraft has been the main subject of two previous master's thesis projects^{1, 2}, wherein we refer for further details on the subject.

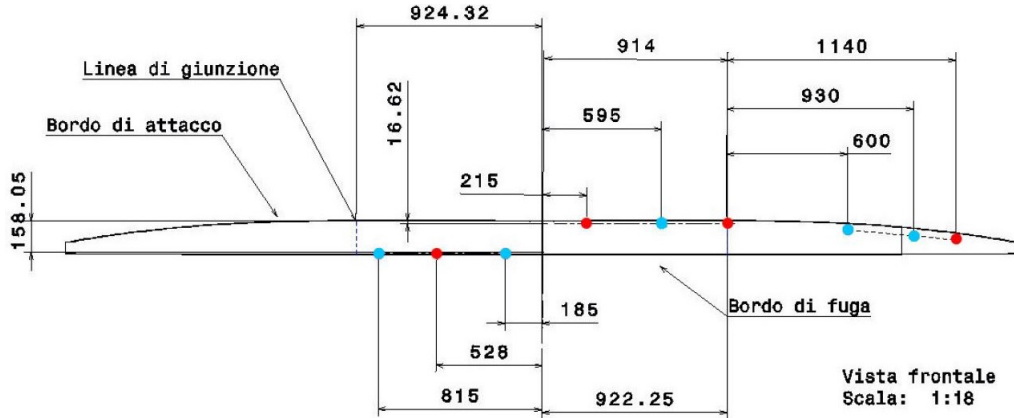


Figure 1.2: FBG sensors arrangement on RA [4],[5]

¹"Monitoraggio termico con sensori Fiber Bragg Grating", Marco Bertuccelli [4]

²"Implementazione di sensori FBG per il monitoraggio strutturale di un velivolo sperimentale", Giuseppe Impicciatore [5]

In Figure 1.2, red dots refer to FBG in direct contact with the wing, while blue ones refer to FBG mounted on the platelets, working as temperature sensors only.

1.1.1 Thermomechanical decoupling on RA

The characteristics of FBG sensors, which will be discussed in the next chapters, are such that they measure a deformation of the sensor, which can be caused either by a mechanical stress, such as a tensile load, or by a temperature change.

As a result, the problem of decoupling thermal phenomena from mechanical phenomena arises, with the aim of quantifying the mechanical strain and the temperature (change in temperature from a reference state).

In order to measure the structural deformation of RA, the optical sensors were bonded in direct contact with the structure using two-component epoxy resin.

To guarantee a thermomechanical decoupling, a system based on carbon fibre plates was added between the structure and the fibre itself. Then, the FBGs were glued upon those plates using two-component epoxy resin.



Figure 1.3: Thermomechanical decoupling plate [4], [5]

This system works by constraining the plate only on one side in order to separate it from the wing structure when the latter is subjected to a deformation. By doing that, a wing deformation does not affect the plate which remains undeformed.



Figure 1.4: Cantilever beam with decoupling plate

For a better understanding of how the plate should work, in Figure 1.4 a cantilever beam in two different conditions is represented: (1) unloaded, and (2) under a concentrated load applied at the free end.

In condition ① the beam and plate lengths are: L_b and L_p , while in configuration ② they become $L_b + \Delta L_b$ and L_p respectively. In this way, the FBG sensors mounted on the plates would be immune to the mechanical deformations of the structure and would only measure temperature changes.

1.2 Scope and purpose of this thesis

Although from a theoretical point of view the thermomechanical decoupling strategy implemented on RA seemed promising, a multitude of load tests revealed a lack of accuracy in the results. With the aim of being able to implement FBG sensors as strain and temperature sensors in aerospace structures, it was necessary to study a new methodology.

Learning from the experience on RA, this time it was decided to develop and test a new decoupling strategy using laboratory specimens instead of implementing it directly on a real structure. In this way, the difficulty of working with large structures would be prevented, thus speeding up the entire process and avoiding the risk of compromising a real structure with a non-functional solution. Finally, if the results will be sufficiently satisfactory, the implementation on more complex structures would be possible.

Three different systems will be considered in the course of this project, in order to verify the applicability of a decoupling strategy based on a *thermal characterisation* phase (determination of the K_T and λ_0 coefficients) and a *mechanical calibration* (determination of the K_ϵ coefficient). The thermal characterisation allows to find a correlation between the FBG's reflected wavelength and the temperature, while a mechanical calibration aims to find a correlation between a mechanical deformation and the reflected wavelength. Then, if an appropriate system-of-sensors is appropriately designed, the FBGs will be able to operate as mechanical strain and temperature sensors.

The first system will be the simplest yet the least autonomous, and will be composed by an FBG and a digital temperature-sensor. The second, on the other hand, will consist exclusively of optical sensors installed on two physical supports, mechanically decoupled from each other. The last one, finally, will be composed exclusively of optical sensors installed on a single physical support and will represent the most interesting solution for real applications as it will be independent of external supports and sensors, and will be able to guarantee a high degree of integration within the structure being analysed.

Chapter 2

Optical fibers and FBG sensors

The optical fiber is a material that is made up of a cylindrical glass structure that can conduct light into itself. In recent decades, they have transformed multiple technology sectors, most notably communication, and have also found several uses in the medical, lighting engineering, and infrastructure fields.

However, due to their complete insensitivity to electromagnetic interference (EMI), the ease of multiplexing different signals on a single line, the excellent resilience to hostile environments, the very compact dimensions, and the significant overall weight savings resulting from signal cable reduction, optical fiber-based technological solutions are a compelling alternative to traditional sensing elements, also for the aerospace sector.

In this paper, we will study optical sensors based on Fiber Bragg Gratings (FBG), which can replace a variety of existing sensors providing temperature, vibration, and mechanical deformation measurements.

2.1 Optical Fibers

An optical fiber presents a cylindrical structure with several concentric layers. The most internal one is known as *core* with a refractive index n_1 and a diameter ranging from 5 and 50 μm . It is surrounded by an outer layer called *cladding*, which is appropriately doped to achieve a refractive index $n_2 < n_1$ with a thickness of 125 μm , and a final protective layer, the *coating* (figure 2.1) which is placed to preserve the structure from eventual damages, caused by the fiber's extremely low bending resistance.

Because of its high fragility, several additional exterior layers could be added to enhance mechanical strength.

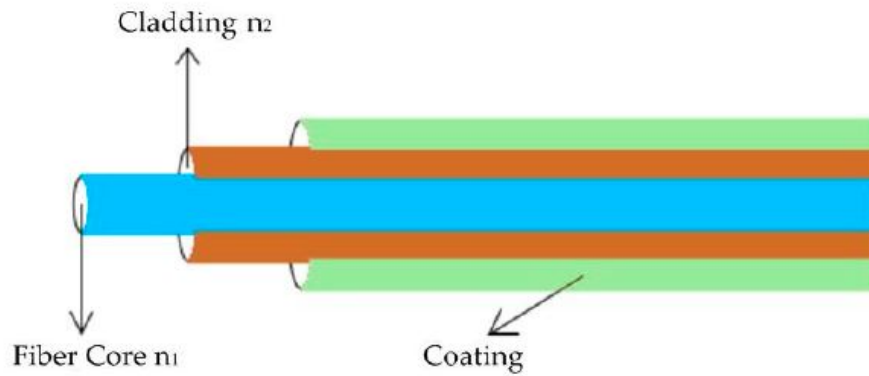


Figure 2.1: Architecture of an optical fiber [6]

2.1.1 Working principles

The signal transmission process within the fibre obeys the principle of total reflection. In fact, since the refractive index of the core n_1 is greater than that of the cladding n_2 , according to Snell's Law:

$$n_1 \sin \theta_1 = n_2 \sin \theta_2$$

where:

- θ_1 is the angle of incidence
- θ_2 is the refraction angle

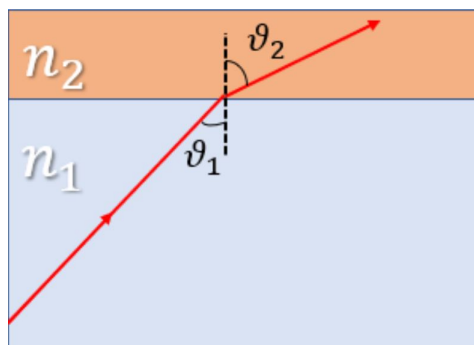


Figure 2.2: Snell's law

It turns out that for an angle of incidence θ_1 greater than:

$$\theta_c = \arcsin \frac{n_2}{n_1}$$

the light beam introduced into the core will undergo total reflection ($\theta_2 = \frac{\pi}{2}$) at the interface between core and cladding, resulting confined within the optical fiber and allowing the signal transmission. This condition is always verified in optical fibers.

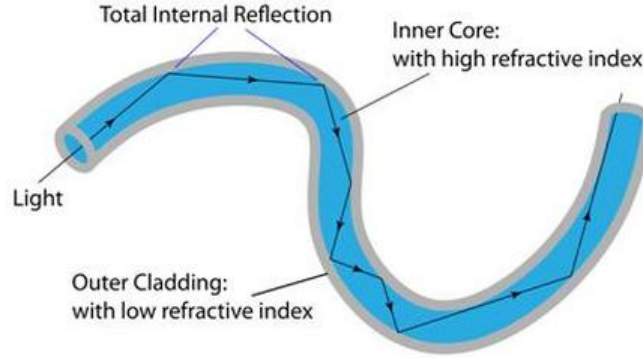


Figure 2.3: Signal propagation within an optical fiber

2.2 FBG sensors

Optical fiber can only transmit signals. FBG sensors can be used as a sensor for mechanical deformations and temperature variations. There are various benefits from using them:

- They are unobtrusive due to their light weight and compact size
- They do not require power to operate
- They can be easily integrated into composite materials during the lamination phase, as well as being bonded to the surface like conventional sensors
- They are also suitable for application in highly stressed structures
- A large number of sensors can be installed on a single optical line

However, they also have a list of drawbacks, including the difficulty in compensating the temperature effect on measurements, the high fragility of the fiber which necessitates large curvature radii to minimize signal loss or attenuation, and ultimately the high costs of both sensors and optical interrogators necessary for measurement.

Fiber Bragg Gratings are, so, the sensors employed in this project (FBG). They are generated in the fiber by using a laser method to create a periodical variation in the core refractive index. At the end of this process, in a fiber trait of about 1 cm, there are some core bands with a changed refractive index. Each of the bands with the modified refractive index is separated by a particular distance, which is known as *grating period* Λ_G .

Now, when the light crosses through it, the sensor is able to reflect a certain wavelength called *Bragg frequency*, described by the following equation:

$$\lambda_B = 2n_{eff}\Lambda_G \quad (2.1)$$

where λ_B is the wavelength reflected by the FBG, n_{eff} is the refractive index of the fiber (after the remodulation), Λ_G is the pitch of the grating as shown in Figure 2.4. The sensor output is represented by the Bragg frequency.

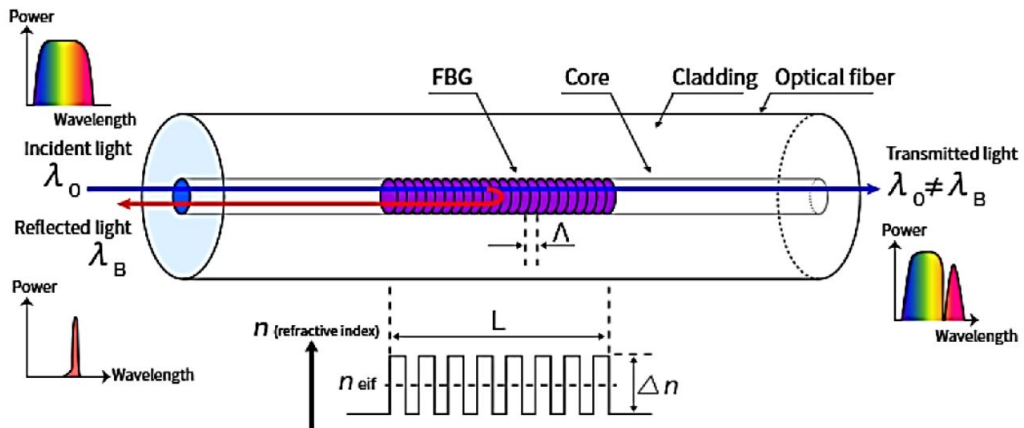


Figure 2.4: FBG working mechanism [1]

The equation 2.1 reveals the dependence of the Bragg frequency on the grating pitch, which is a physical distance. This means that the variation in the reflected wavelength is always related with a mechanical strain generated on the grating period by an external factor.

As a result, the FBG can measure a change in the Bragg wavelength caused by multiple effects (mechanical deformation, temperature, humidity), but it is not able to quantify the distinct contributions, at least in a first instance.

In the case of constant temperature and humidity (or defined by very little fluctuations or extremely slow temporal evolutions), their effect on the accuracy of the mechanical deformation measurements of the FBG can be assumed minimal.

On the contrary, as the above-mentioned variations increase, this strategy will become less and less effective (i.e. when their effect is no longer negligible compared to the mechanical deformations to be measured).

As a consequence, in the event of significant variations in temperature or environmental humidity, it is essential to examine the impact these changes have on FBGs measurements and formulate an appropriate approach for filtering the raw values provided by the optical sensors affected by such disturbances.

Therefore, when using FBGs as mechanical strain sensors, it is essential to establish an effective compensating technique (2.2.2).

2.2.1 FBG as Mechanical strain and Temperature sensors

The grating works as a wavelength-specific dielectric mirror: the FBG reflects a particular wavelength while transmits the others. The reflected wavelength λ_B is associated to the grating pitch Λ_G and refraction index n_{eff} by equation 2.1.

FBGs work on the basis of Fresnel reflection. This physical phenomena allows for the development of temperature and strain sensors.

Mechanical deformation $\Delta\varepsilon$ and temperature variation ΔT influence both the effective refractive index and the axial pitch of the fiber, resulting in a change in the reflected wavelength.

Therefore, the variation of the reflected wavelength $\Delta\lambda_B$ can be expressed as follows:

$$\Delta\lambda_B = \lambda_B(1 - p_e)\Delta\varepsilon + \lambda_B(\alpha_\Lambda + \alpha_n)\Delta T \quad (2.2)$$

where:

- λ_B is the nominal reflected wavelength;
- p_e is the strain-optic or photoelastic coefficient of the fiber;
- $\Delta\varepsilon$ is the variation of fiber strain;
- α_Λ is the thermal expansion coefficient of the fiber;
- α_n is the thermo-optic coefficient of the fiber;
- ΔT is the variation of the temperature;

Equation 2.2 can be reformulated as:

$$\Delta\lambda_B = K_\varepsilon\Delta\varepsilon + K_T\Delta T \quad (2.3)$$

where the terms $K_\varepsilon = \lambda_B(1 - p_E)$ and $K_T = \lambda_B(\alpha_\Lambda + \alpha_n)$ are defined as *coefficient of strain* and *coefficient of temperature*, respectively. These coefficients are derived considering an optical fiber which is stressed but not bonded to other materials (Table 2.1).

More specifically, K_ε is a function of the strain-optic coefficient: it depends from the material of the fiber and describes the variation of the refraction index induced by a normal stress.

Instead, the K_T is composed by two different contributes:

- the thermo-optic coefficient α_n which represents the variation of the refraction index caused by the temperature
- the thermal expansion coefficient α_Λ , which is related to the effect of temperature on the physical disposition of the Bragg grating.

Their values, in the case of fiber not glued to any support, are summarised in the following table:

p_e	$\alpha_\Lambda \left[\frac{1}{^\circ C}\right]$	$\alpha_n \left[\frac{1}{^\circ C}\right]$
2.12×10^{-1}	5.5×10^{-7}	5.77×10^{-6}

Table 2.1: Characteristics of not glued FBG [2]

2.2.2 Thermal compensation techniques

Temperature compensation plays a key role in the application of FBGs as mechanical strain sensors. Over the years several approaches have been developed to address this problem, and some of them are proposed below.

FBGs embedded in a capillary glass tube

A first decoupling method consists of inserting two FBGs inside a capillary tube. One of the two sensors (G1) is firmly attached to a glass tube through epoxy resin, as shown in Figure 2.5 [7].

In this way, the constrained sensor does not undergo mechanical deformation due to stresses, but is sensitive only to temperature variations, while the second grating

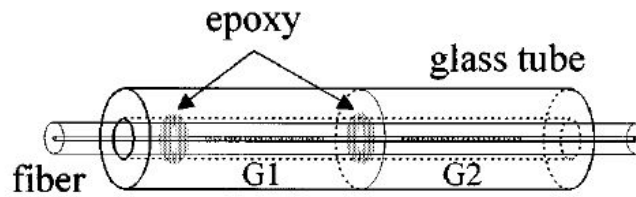


Figure 2.5: Two FBG embedded in a glass tube

(G2) is sensitive to both variations. In this way, by comparing the wavelength variations of G1 and G2, it is possible to determine the thermal and mechanical contribution and decouple their effects.

FBGs embedded in a composite structure

This method is a variant of the previous technique. In this case, the capillary is placed at the end of the fibre and incorporates a single FBG. The optical sensor is insulated similarly to the previous case with epoxy resin inside the capillary, in order to let it perceive only temperature variations. The mechanical strain measurement will be carried out by means of a second FBG, which will be positioned close to the first to avoid possible temperature gradients between their positions [8].

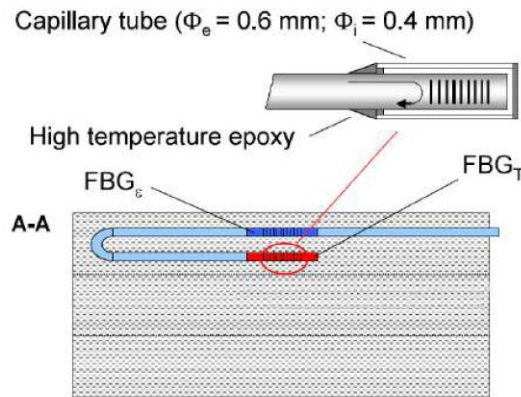


Figure 2.6: Two FBGs embedded in a composite structure

This strategy is designed for integration into composite structures, although, like the previous one, it is particularly intrusive.

Direct compensation of the thermal expansion coefficient

This technique allows to determine the mechanical deformation acting on the sensor by performing direct temperature compensation, making the grating insensitive to temperature variations. This is accomplished by nullifying the proportionality coefficient K_T (eq. 2.3).

To achieve this, the FBG sensor is embedded inside a tube of a liquid-crystalline polymer material and epoxy resin (Figure 2.7). The polymer has a negative thermal expansion coefficient, which balances the one of the fiber, resulting in a temperature-insensitive system [9].

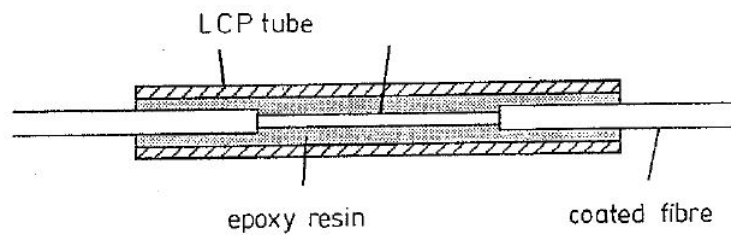


Figure 2.7: FBG inside a liquid-crystalline polymer tube

Overlapping of FBGs

The method works by overlapping two FBGs which have the gratings in the same section of the fiber [10].

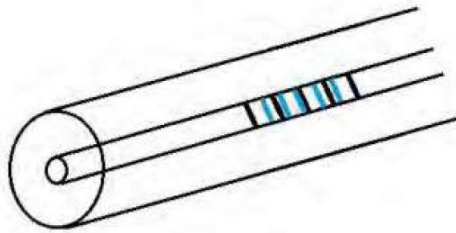


Figure 2.8: Overlapping of two FBGs [3]

It is based on solving the linear system:

$$\begin{Bmatrix} \Delta\lambda_1 \\ \Delta\lambda_2 \end{Bmatrix} = \begin{bmatrix} K_{\varepsilon_1} & K_{T_1} \\ K_{\varepsilon_2} & K_{T_2} \end{bmatrix} \cdot \begin{Bmatrix} \Delta\varepsilon \\ \Delta T \end{Bmatrix}$$

In fact, the two optical sensors are subjected to the same $\Delta\varepsilon$ and ΔT . Since the $\Delta\lambda_1$ and $\Delta\lambda_2$ are known, if the coefficients $K_{\varepsilon_{1,2}}$ and $K_{T_{1,2}}$ are also known and if the FBGs have significantly different Bragg wavelengths, such that:

$$\begin{cases} K_{\varepsilon_1} \neq K_{\varepsilon_2} \\ K_{T_1} \neq K_{T_2} \end{cases}$$

it is possible to solve the system and to measure the temperature and mechanical strain variations.

Chapter 3

The experimental test bench

This thesis project is based on a series of experimental studies intended to validate a thermomechanical calibration method presented and discussed in the following chapters. Since the validity of the suggested approach was unknown a priori, it was decided to build in laboratory a series of test specimens to conduct the tests on, in order to benefit from the convenience of dealing with tiny and easy-to-build structures. Then, if the results will be promising, they will potentially be extended to the scenario of more complex structures, such as RA aircraft.

3.1 Samples preparation

There were built *two samples*, which share the same rectangular shape (260x35x 1.6 mm) and are composed of 14 layers of unidirectional carbon fibre. They were cut from a single block of composite material made of Tenax UTS 50 carbon fibre and, as matrix, "Epoxi ResinL" produced by Cyttox.

Tenax UTS50	
E_{11}	54000 [MPa]
E_{22}	54000 [MPa]
ν	0.068
σ_{max}	509
G	4200 [MPa]
Ply thickness	0.11 [mm]

Table 3.1: Tenax UTS50 Properties [5]

3.1.1 Specimen 1

The first sample, called "*Specimen 1*", has been equipped with a single optical line containing 1 FBG and positioned along the elastic axis (in the centreline) and approximately at mid-length.

This optical line was pre-stretched (i.e. pre-loaded) during the bonding phase.

The bonding phase was divided into several steps:

- 1 Positioning and clamping of the specimen on two 3D-printed supports, anchored to an optical breadboard (Figure 3.1)
- 2 Positioning of the fibre and FBG sensor in the desired position
- 3 Initial fixing of one end of the fibre: by means of adhesive tape on the portion of the fibre equipped with a heat-shrink sleeve (yellow), and by means of cyano-acrylic glue on a portion immediately downstream (darker portion to the right in figure)

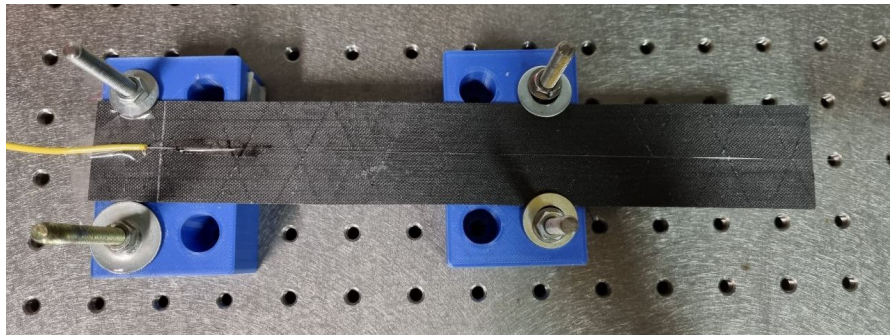


Figure 3.1: Specimen 1, bonding phase: step 1 to 3

- 4 Anchoring the free end of the fibre to a plate, which is constrained on a linear-translator



Figure 3.2: Linear translator

- 5 Pre-loading the fibre by translation of the linear-translator
- 6 Deposition of an epoxy resin layer over the entire line (Figure 3.3)

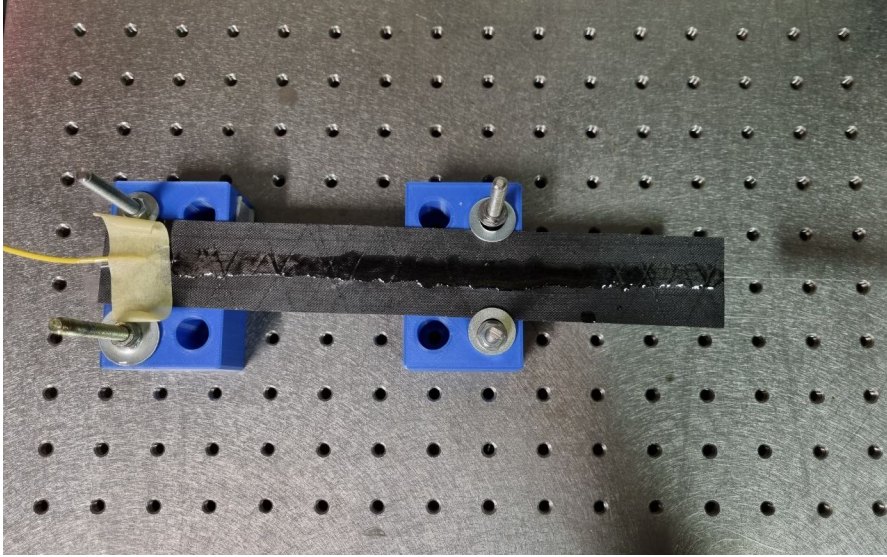


Figure 3.3: Specimen 1

- 7 Wait for the end of the resin curing process (approx. 7 days)
- 8 Release and cut of the free extreme

The characteristics are summarized in the following table:

Specimen 1	
$\Delta\varepsilon$	1500 [$\mu\varepsilon$]
$\lambda_{B,0}$	1540.457 [nm]
$\lambda_{B,final}$	1542.277 [nm]

Table 3.2: FBG characteristics of Specimen 1

Where, under the hypothesis of constant temperature:

$$\lambda_{B,final} = \lambda_{B,0} + K_\varepsilon \cdot \Delta\varepsilon$$

and in first approximation, from Table 2.1:

$$K_\varepsilon = \lambda_{B,0} \cdot (1 - p_E) = 1540.457 \cdot 0.788 = 1213.88 [nm]$$

3.1.2 Specimen 2

The second sample, called "*Specimen 2*", shares the same dimensions of the previous one, and is equipped with 2 optical lines, each containing 2 FBG of 1546 and 1538 [nm] nominal Bragg wavelength. Both lines are symmetrically placed with regard to the central axes (elastic axes).

As a peculiarity, only one optical line is pre-loaded ($3500 \mu\epsilon$). The bonding and pre-loading procedure is the same as for Specimen 1. The second line, instead, is simply placed on the specimen and then bonded with epoxy resin.

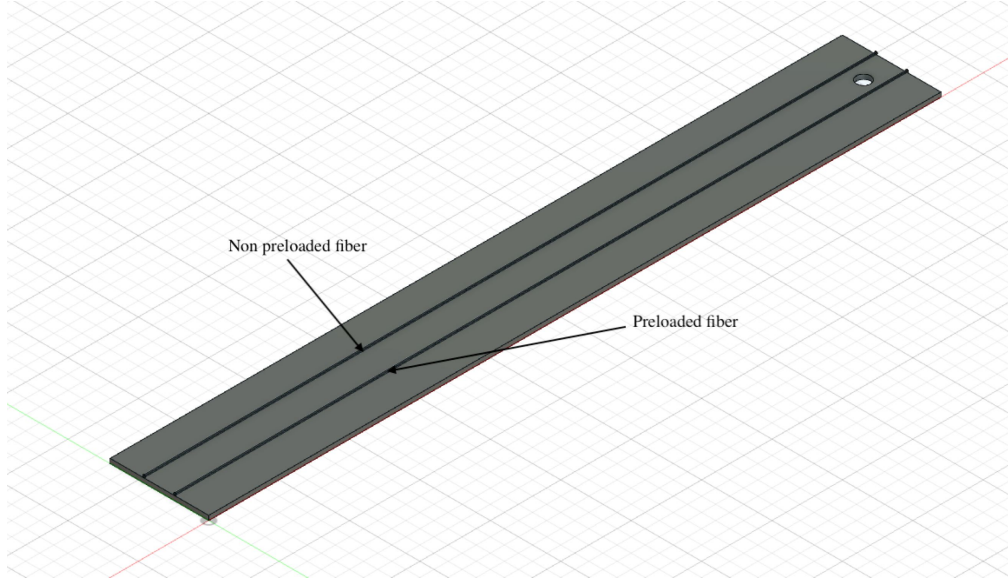


Figure 3.4: Representation of Specimen 2

The characteristics of the FBGs are summarized below:

Specimen 2				
		$\Delta\epsilon$ [$\mu\epsilon$]	$\lambda_{B,0}$ [nm]	$\lambda_{B,final}$ [nm]
Line 1	FBG1	3500	1546	1550.2638
	FBG2	3500	1538	1542.1987
Line 2	FBG1	0	1546	1546
	FBG2	0	1538	1538

Table 3.3: FBGs characteristics of Specimen 2

And their disposition is illustrated in Figure 3.5.

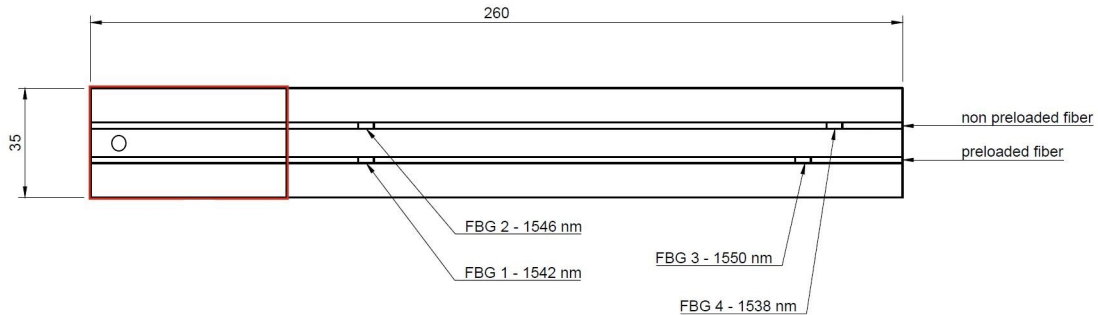


Figure 3.5: FBGs location on specimen 2

As can be seen from the picture, the sample has also a circular hole at a free end, approximately in the elastic axes, which will be useful for applying a load and conduct bending tests.

3.2 Climatic chamber

In the thermomechanical calibration phase, temperature plays a fundamental role, therefore an instrument that allows its values to be monitored and modified has taken on a central role in carrying out the experimental tests: the *climatic chamber*.



Figure 3.6: KK-50 CHLT [11]

The one used in the course of this project is the KK-50CHLT model produced by Kambic, which allowed both specimens (Specimen 1 and Specimen 2) to be housed inside it, making it possible to vary and/or maintain their temperature to a desired value, in order to conduct the required tests.

The characteristics of the instrument are summarised in the table below:

KK-50 CHLT	
Ext. dimensions	570 × 1035 × 645 mm
Int. dimensions	400 × 375 × 350 mm
Volume	50 L
Temp. range	-40 +180 °C
Temp. resolution	0.1 °C
Heating rate	5.3 °C/min
Cooling rate	2.1 °C/min

Table 3.4: Climatic chamber characteristics

3.3 Temperature acquisition

When carrying out time-varying temperature tests, as well as constant-temperature tests, it is important to know the value at well-defined intervals, be they one second or even a few minutes.

To do this, a Sensirion SHT85 sensor, capable of measuring both temperature and humidity, was used in this project. In order to work, it needs to be interfaced to a microcontroller, such as, in our case, an Arduino UNO, which in turn is connected via USB cable to a computer in order to read the output values.

The connection diagram between the SHT85 sensor and the Arduino UNO microcontroller is shown below:

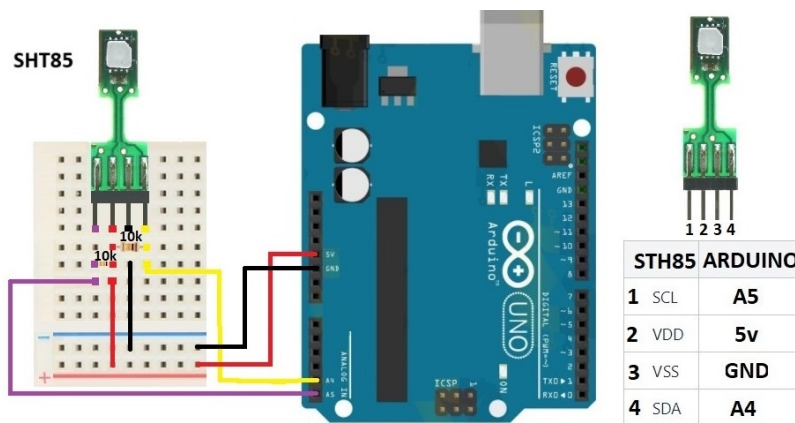


Figure 3.7: Arduino UNO - SHT85 connection diagram [12]

Furthermore, in order to work, a specially written code must be loaded onto the microcontroller board via a PC, which in the case of this project can be found at [Appendix A].

This script permits printing on the serial monitor the temperature value (and if desired also humidity) measured by the sensor at well-defined time intervals, for example one second. Once the measurement is complete, the serial monitor data can be saved in a ".txt" file and made accessible for post-processing.

3.4 FBG data acquisition

The procedure for acquiring data produced by FBG sensors (in terms of reflected wavelength) essentially requires two components: a *computer* and an *optical interrogator*. The optical interrogator is an instrument capable of both emitting a light signal and receiving the reflected signals from the gratings.

The instrument used for this work is a *SmartScan* manufactured by *SmartFibres* (Figure 3.8), which is a Wavelength Division Multiplexing (WDM) instrument, based on an agile, tuneable laser source that enables high-resolution interrogation at multi-kHz frequencies.



Figure 3.8: SmartScan optical interrogator [13]

Its main characteristics are summarized in the following table:

Wavelengths	Channels	Max Sensors per Channel	Max scan frequency
1528 – 1568 nm	4	16	2.5 kHz

Table 3.5: SmartScan characteristics [13]

The interrogator, in addition to being powered from an electrical outlet, needs to be interfaced with a computer via LAN connection, on which the Smartfibres software must be installed.

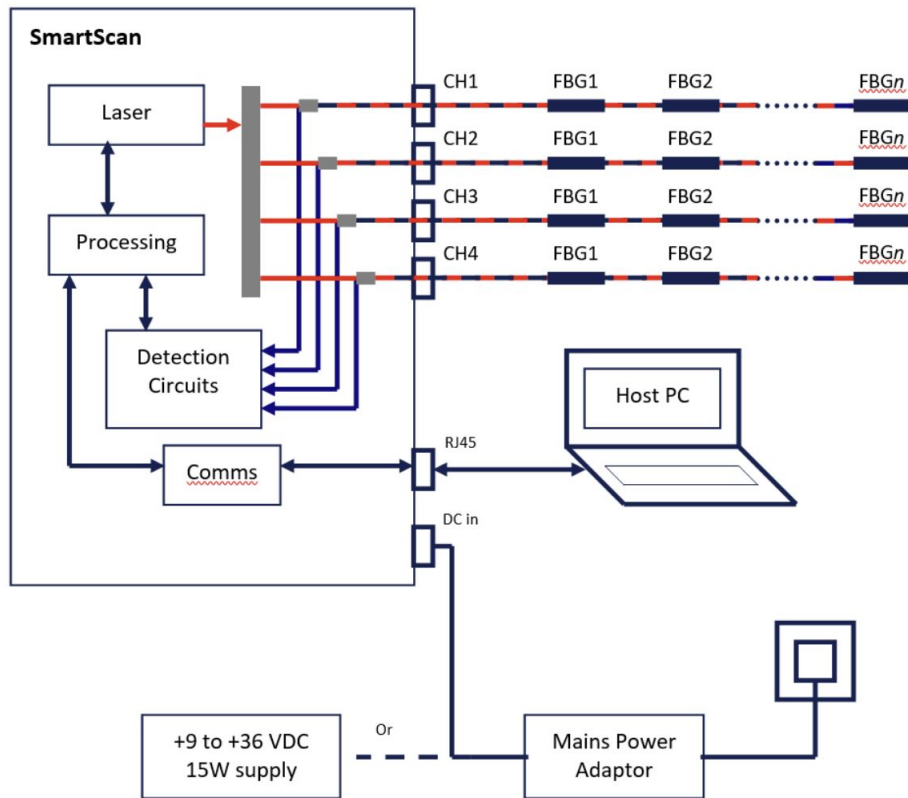


Figure 3.9: SmartScan connections [13]

The main screen of the software (Figure 3.10) consists of a real time graph showing the response of the fibre, i.e. the intensity and wavelength of the peaks due to the signal reflected by the FBG sensors. At the top left, it is possible to choose the number of channels, and therefore the number of fibres to be used.

In addition, it is possible to specify how many sensors per channel are present. From this screen is also possible to set other parameters, such as the acquisition frequency, the intensity threshold below which the peak is no longer detectable, the size of the sampling interval and the transmission frequency.

To start an acquisition it is necessary to go to the "Basic Acquisition" or "Enhanced Acquisition" screen (Figure 3.10), where it is possible to specify the path to the output file, i.e. a text file containing the wavelength values of the various peaks, corresponding to the single FBG sensors, for each sampling time interval.

These files were then imported into Matlab for the necessary post-processing operations.

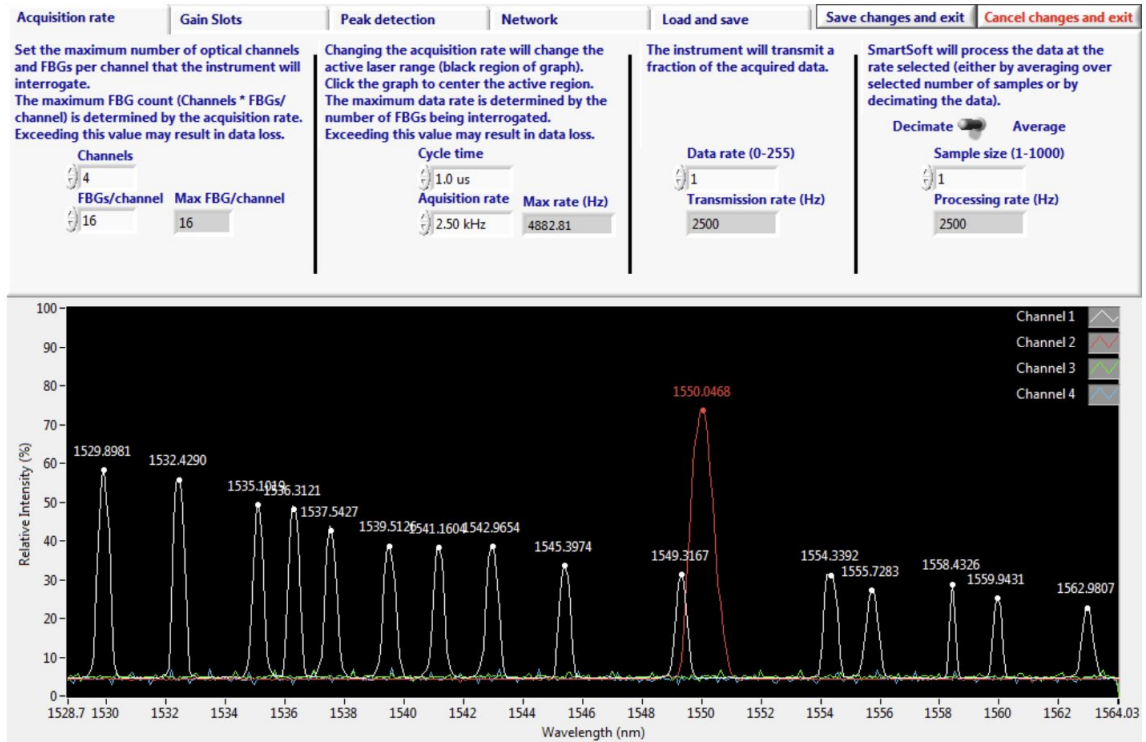


Figure 3.10: Smartfibres main screen [13]

3.5 Data post-processing

Once the data acquisition from the SmartScan and the SHT85 is done, the post-processing phase begins.

The interrogator's output is represented by a '.log' file (Figure 3.11), which contains the following information:

- In the first two lines are reported the acquisition start time and the time intervals between two measurements. In our case, for a 25 Hz acquisition frequency, the time interval is 40000 μs
- A column division starts from the fourth line. The same line shows the names of the sensors detected, and in the first column the 'Time' entry indicating the acquisition time
- Finally, the data acquired by each sensor at the specific time instant are saved beginning with the sixth line

Esempio_file_log.log - Blocco note di Wi... - □ ×

File Modifica Formato Visualizza ?

Start Time (UTC) = 1652096079,900698
Time interval = 40000 us

Time	Ch01Gr01 Wavelength (nm)	Ch01Gr02 Wavelength (nm)
0,000000	1545,7857	1537,6937
0,040000	1545,7857	1537,6945
0,080000	1545,7865	1537,6937
0,120000	1545,7865	1537,6929
0,160000	1545,7873	1537,6929
0,200000	1545,7873	1537,6929
0,240000	1545,7873	1537,6929
0,280000	1545,7865	1537,6937
0,320000	1545,7873	1537,6929
0,360000	1545,7873	1537,6937
0,400000	1545,7865	1537,6937
0,440000	1545,7888	1537,6929
0,480000	1545,7880	1537,6937
0,520000	1545,7880	1537,6929
0,560000	1545,7880	1537,6929
0,600000	1545,7873	1537,6937
0,640000	1545,7880	1537,6929
0,680000	1545,7880	1537,6937
0,720000	1545,7888	1537,6937
0,760000	1545,7888	1537,6929
0,800000	1545,7880	1537,6929
0,840000	1545,7888	1537,6937
0,880000	1545,7880	1537,6922
0,920000	1545,7880	1537,6937
0,960000	1545,7888	1537,6922

Linea 4, colonna 100% Windows (CRLF) UTF-8

Figure 3.11: SmartScan output file

The SmartScan interrogator can read up to 4 optical channels, each with up to 16 sensors. In the output file, each sensor is sorted by the channel to which it is linked, and the numbering for each grating decreases with wavelength. For example, the FBG sensor attached to the first channel with the longest wavelength will be reported as *Ch01Gr01*, whereas the sensor with the next shortest wavelength will be shown as *Ch01Gr02*. This sorting is noteworthy since it ignores the spatial arrangement of the sensors and instead is focused exclusively on their wavelengths.

Once it is clear how to handle the file, it is possible to start processing it. To this end, special Matlab scripts have been created for each type of experimental test, which allow the files generated by both the interrogator and the Arduino to be read and processed, depending on the purpose of the test itself. Thus, the wavelengths, the time elapsed since the start of the acquisition and the name of each FBG sensor are saved in a structure, while the temperature data of the SHT85 are saved in a vector to make them easily accessible.

Chapter 4

Experimental campaign

As far as utilizing FBG as mechanical and thermal sensors is concerned, the issue of thermomechanical decoupling must be addressed. The thermomechanical decoupling issue consists in the ability to distinguish and quantify the thermal contribution (temperature variation) from a mechanical strain (of the sensor and/or of the surface to which it is bonded), and vice-versa.

The FBGs allow such effects to be measured by means of a change in the reflected wavelength, and, as mentioned in 2.2.1, the relationship linking these phenomena is:

$$\Delta\lambda_B = K_\varepsilon\Delta\varepsilon + K_T\Delta T \quad (4.1)$$

Where $\Delta\lambda_B$ generally refers to the difference between the measured wavelength λ_m and the Bragg wavelength λ_B . It is possible to rearrange *the mechanical and thermal contribution* in the compact form:

- $\Delta\lambda_\varepsilon = K_\varepsilon\Delta\varepsilon$; i.e. the wavelength variation due to a mechanical strain
- $\Delta\lambda_T = K_T\Delta T$; i.e. the wavelength variation due to a temperature change

Assuming, at first, that the coefficients K_ε and K_T are known, it is easy to understand that the decoupling problem is highly dependent on the number of optical lines and FBG sensors involved. In fact, equation 4.1 shows 2 unknowns quantities: $\Delta\varepsilon$ and ΔT , so, if only one FBG is used, the corresponding linear system of equations would be underdetermined and impossible to solve. This is the case for Specimen 1.

Anyway, there are several possibilities to solve this problem. The first one considered in this work, consists in the employment of a single FBG and a second

not-optical sensor to determine one of the two unknowns, such as the temperature.

A further possibility is to replace the digital sensor with an optical one to determine the remaining unknown, obtaining in this way a full optical system. This procedure will be addressed twice in the following chapter. To this end, two separate and mechanically independent optical lines will initially be considered, while later on, the procedure will be extended to a single structure upon which two optical lines are installed, in order to solve the linear system in a completely autonomous way.

Although it is merely a matter of solving a linear system, this problem is far from simple to solve as the K_ε and K_T coefficients are not known for either of the two specimens. In fact, since the considered FBG sensors are bonded (and pre-tensioned) to a carbon fiber composite structure, known values from literature, such as those in table 2.1, lose validity and must be specifically determined. All of these topics will be examined in the following paragraphs, beginning with the simplest case and progressing to the most complex yet promising.

4.1 A simple digital-optical system

The experiment begins with the most basic configuration, which consists of using only Specimen 1 and a digital temperature sensor, the SHT85.

The first stage of this activity is to determine the K_T coefficient of the FBG installed on Specimen 1; this is referred to as *thermal characterization*. Following that, two bending load tests will be performed on the specimen, one maintaining a constant temperature and one at variable temperature.

4.1.1 Thermal characterisation [0 40]°C

The thermal characterisation of Specimen 1 consists determining the K_T coefficient of the FBG through a direct correlation between wavelength variation and temperature variation. This procedure is feasible if the FBG is not subject to mechanical deformation, i.e. if the applied load is zero.

In fact, in case of no load applied to the sample, equation 4.1 takes the following form:

$$\Delta\lambda_B = K_T\Delta T$$

And since the ΔT is known from the temperature sensor, as is the $\Delta\lambda_B$ from the SmartScan, it is immediate to determine the K_T .

The experimental activity was carried out according to the following steps:

- Setting up Specimen 1 on a flat surface inside the climatic chamber
- Connecting the FBG with the SmartScan
- Positioning the SHT85 sensor in close proximity to the FBG, in order to capture as accurately as possible the same temperature perceived by the optical sensor
- Setting the temperature interval in the climatic chamber and its rate of change (°C/h)
- Simultaneous start of the climate chamber cycle and the acquisition of the temperature and the FBG wavelengths
- End of acquisitions and temperature cycle
- Data storage and post-processing

The climatic chamber setup is shown below:

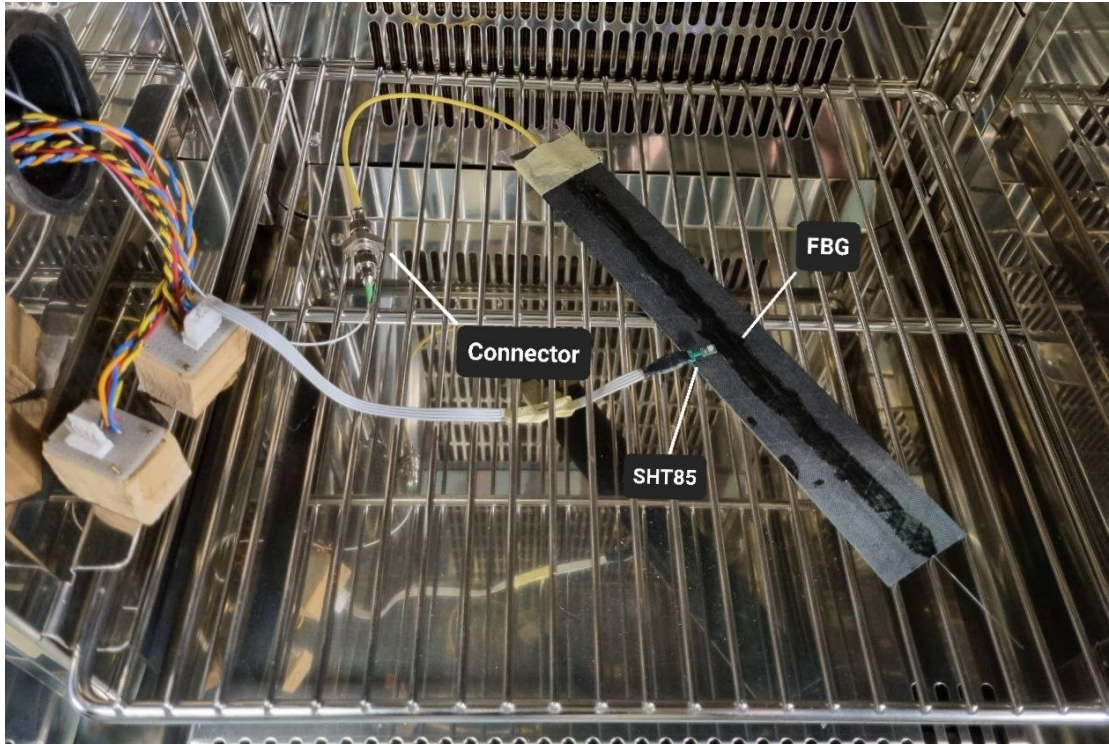


Figure 4.1: Specimen 1 setup for thermal characterization

An initial thermal characterization was performed in the temperature range from 0°C to +40 °C with a slope of 20°C/h. Since it was the first test in a climatic chamber, a conservative temperature range was chosen to ensure that no elements were damaged or the instruments malfunctioned.

Previous experiments conducted on free FBG sensors (not bonded to any structure) had demonstrated abnormal behavior (a change in the slope of the λ -Temperature line) when negative temperatures were reached¹. Hence, it was chosen to retain the temperature at values greater than or equal to 0°C, while the upper limit of 40°C was established with the purpose of staying far below the operational limits of the resin and to avoid bonding leaks.

¹This topic will be documented in a forthcoming master thesis, which is currently unavailable

The results of the test is shown in the following figures:

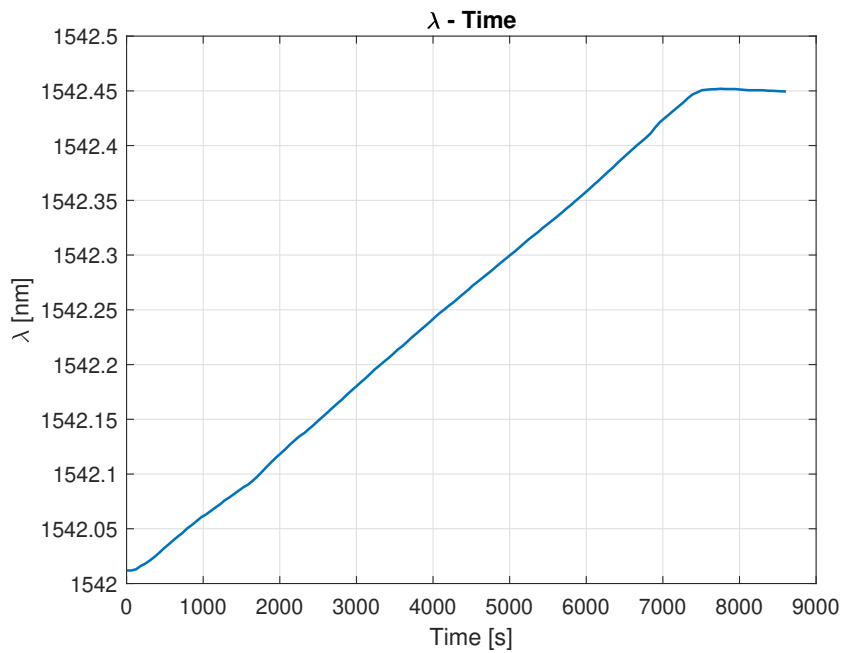


Figure 4.2: λ -time for T.C. of specimen 1 between [0 40] $^{\circ}$ C

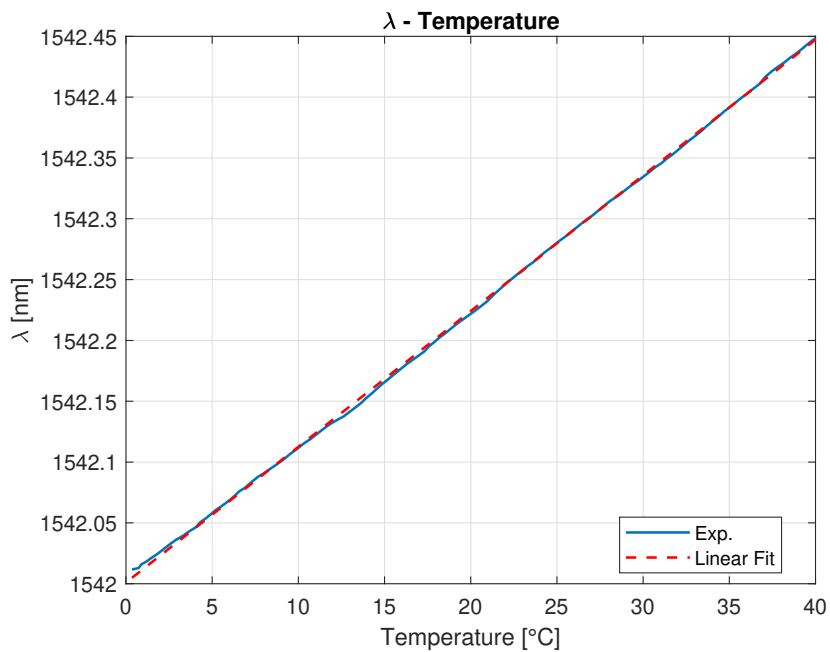


Figure 4.3: λ -temperature for T.C. of specimen 1 between [0 40] $^{\circ}$ C

Figure 4.2 shows the evolution of the wavelengths as a function of time. Horizontal lines at the top-right part are present since the acquisition of wavelengths was interrupted a few minutes after temperature target (40°C) was reached, therefore, as the temperature remained constant and no load was applied, the wavelength measured by the sensor remained constant over time. Considering that the rate of temperature change in the climatic chamber is constant and equal to 20°C/h, a linear correlation between what is measured by the FBG sensor and the temperature can already be appreciated from this image. These considerations are confirmed by what is shown in Figure 4.3, in which the measured wavelengths are directly correlated with the temperature perceived by the SHT85 sensor, that is also the one perceived by the FBG sensor.

As can be seen, the deviation of the actual values (indicated as "Exp." in the graph) from those obtained by a linear interpolation is almost negligible and constitutes a verification of the linearity of the relationship between λ and temperature. In fact, a *Root Mean Square Error (RMSE)* of 0.002 has been calculated.

Using linear interpolation, the K_T coefficient and the wavelength corresponding to 0°C, defined as λ_0 , can be determined. In fact, it is possible to fit the λ -Temperature trend with a line of equation: $\lambda = \lambda_0 + K_T \cdot \Delta T$.

For this test, the values are shown below:

Specimen 1: [0 40] °C	
K_T	0.0112
λ_0	1542.00097 [nm]

Table 4.1: Specimen 1 T.C. between 0°C and +40°C

Introducing the λ_0 coefficient offers several benefits. One of them concerns the pre-tensioning of the optical line. In fact, the rest-wavelength of a pre-tensioned FBG differs from the initial λ_B , becoming a $\lambda_{B,final}$ (see Table 3.2). Considering a pre-loaded FBG sensor, in a general case where $\Delta\varepsilon \neq 0$, what measured by the interrogator is:

$$\lambda_m = \underbrace{\lambda_B + K_\varepsilon \cdot \Delta\varepsilon_0}_{\lambda_{B,final}} + K_\varepsilon \cdot \Delta\varepsilon + K_T \cdot \Delta T \quad (4.2)$$

where $K_\varepsilon \cdot \Delta\varepsilon_0$ is the pre-loading contribution, i.e. the wavelength shift due to pre-tensioning.

By performing the thermal characterisation for the pre-tensioned Specimen, the pre-loading effects are included in the λ_0 coefficient and the relationship is simplified as:

$$\lambda_m = \lambda_0 + K_\varepsilon \cdot \Delta\varepsilon + K_T \cdot \Delta T \quad (4.3)$$

The differences between equations 4.2 and 4.3 not only concerns the pre-loading contribution. In fact, the λ_0 coefficient is referred to a 0°C temperature, which means that in eq. 4.3 the $\Delta T \equiv T$ [°C]. The λ_B , instead, is referred to a different temperature (between 25°C and 35°C), and the ΔT represents the difference between that temperature and the one captured by the sensor.

Finally, it is possible to estimate the temperature perceived by the FBG as:

$$T = \frac{\lambda_m - \lambda_0}{K_T}$$

and compare it with the real value directly sensed by the SHT85:

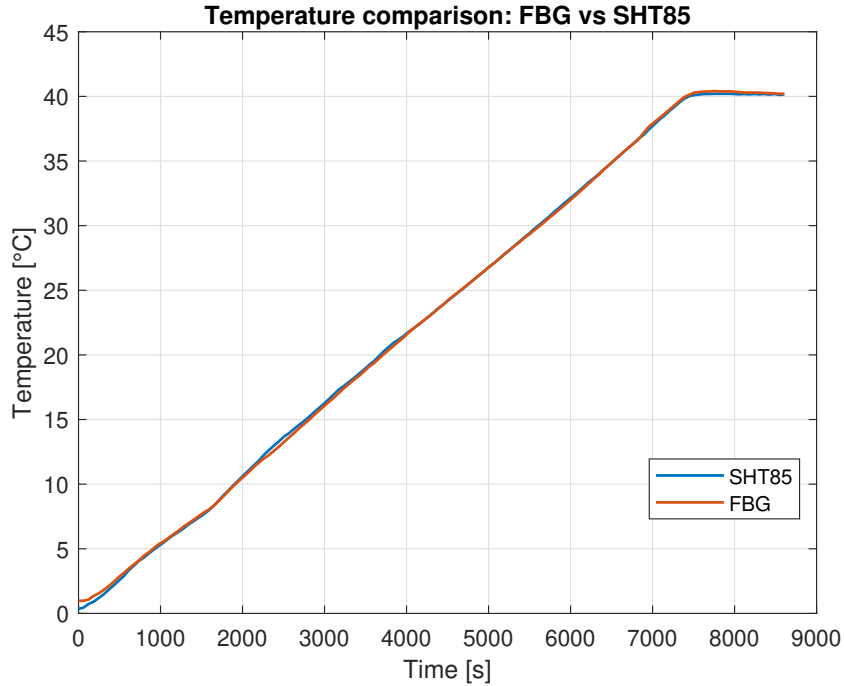


Figure 4.4: Comparison between SHT85 and FBG for specimen 1

The graph clearly shows that the data are almost identical, and demonstrates the effectiveness of this procedure and the high quality of the output provided by the optical sensor.

4.1.2 Bending test at constant temperature

Once the thermal characterisation yielded the K_T and λ_0 coefficients, a bending stress test campaign was carried out to evaluate the thermal decoupling strategy. The intent is to determine the mechanical deformation contribution induced by an external load by subtracting the thermal contribution from the raw data.

The first load test, conducted at constant temperature, consists of applying a time-varying load that induces bending in the specimen and a tensile state in the optical fibre. In order to apply a pure-bending load, Specimen1 was drilled in proximity of the elastic axis so that the weight could be applied as close as possible to the shear centre.

As regards the constraint conditions, the structure was clamped at one end and loaded at the opposite one, as shown in Figure 4.5.

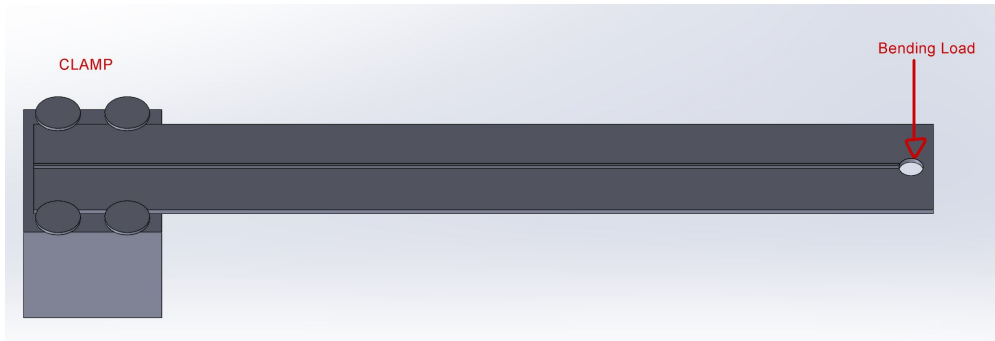


Figure 4.5: Representation of the bending test for specimen 1

The load was applied via a support that was mechanically linked to the test specimen, allowing the use of different weights. The load sequence was established by the availability of weights in the laboratory and was the following: 0, 85g, 130.3g, 175.6g, 225.4g, 275.2g, 325.4g and 375.2g.

In order to measure the deformation state caused by the application of a static load, a time interval of 1 minute was chosen between each load step to wait until the oscillations of the specimen were entirely damped.

The temperature was kept approximately constant ($T=22.5^{\circ}\text{C}$) and was acquired via the SHT85, which was placed close to the FBG sensor.

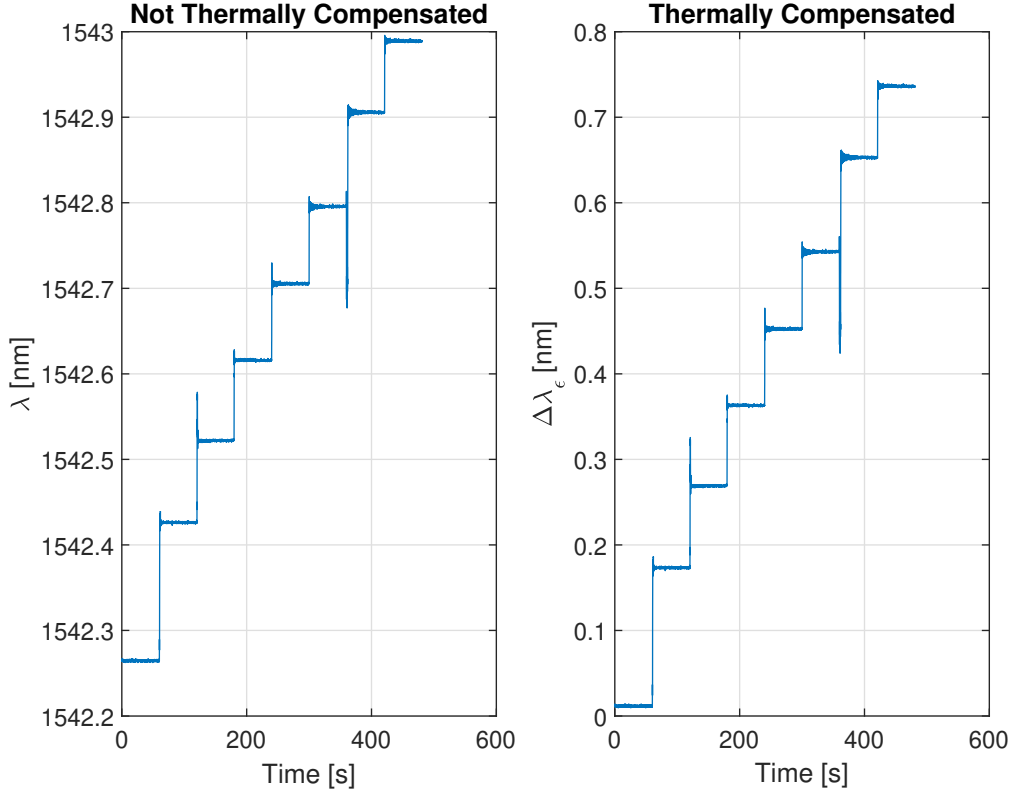


Figure 4.6: λ -time for bending test at constant temperature

The left image of Figure 4.6 shows the time evolution of the raw data measured by the sensor, while the right part shows the values obtained by thermal compensation, i.e. the raw data from which the thermal contribution was removed:

$$\Delta\lambda_\epsilon = \Delta\lambda_B - \Delta\lambda_T \quad (4.4)$$

Because of the discrete application of loads, the wavelengths have a stepped pattern. As shown in the graph, not all steps are equal which is due to the usage of different weights (1x85g, 2x45.3g, 2x49.8g, 1x100g) based on laboratory availability. A peculiar pattern is noticeable at the time when the load is applied: peaks of wavelengths are recorded as a result of the manual and inevitable clumsy introduction of the weight. This is visible especially at the beginning of the third and seventh steps. In the latter case, a decrease in wavelength is recorded because of the removal of a 49.8g weight (followed by the addition of a 100g weight).

The oscillations caused by the weights highlights the FBG sensor's excellent sensitivity, despite the acquisition frequency being limited to 25Hz. Figure 4.7 details the application of the sixth load.

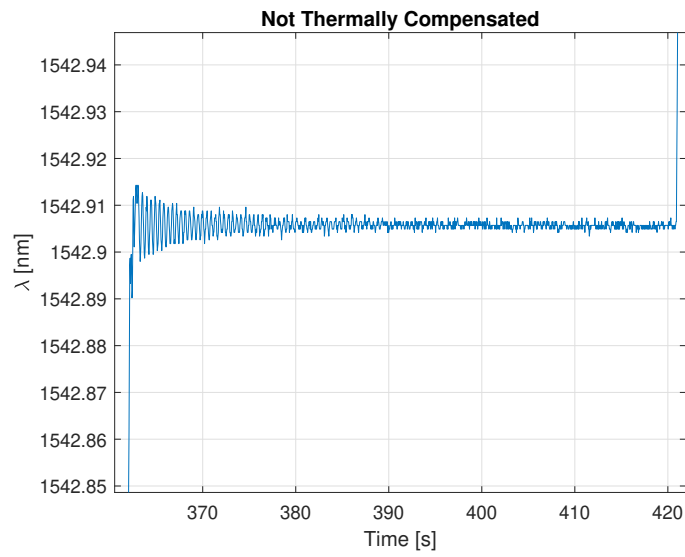


Figure 4.7: Specimen oscillation when applying a load

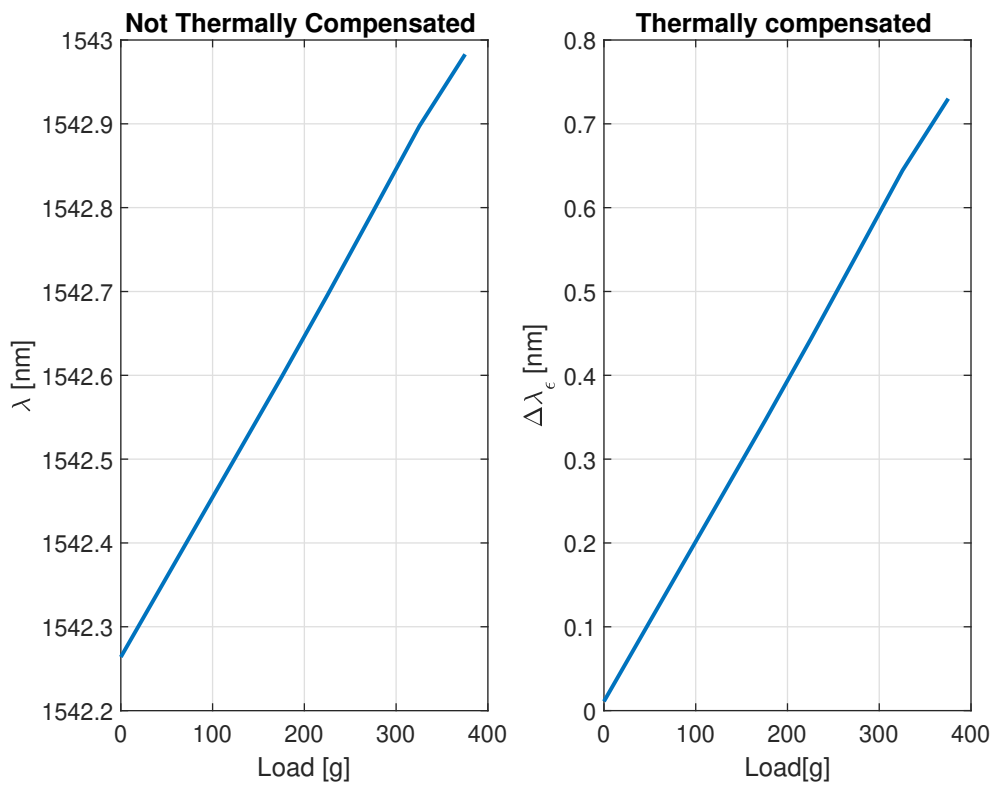


Figure 4.8: λ -load for bending test at constant temperature

Figure 4.8 depicts the relationship between raw and thermally compensated wavelengths as a function of applied load. It is clear that there is a linear relationship between measured wavelength and applied load, i.e. specimen deformation. An analysis of the compensated data reveals that, contrary to expectations, the residual mechanical deformation obtained is not exactly zero at zero load. This anomaly, although almost negligible, could be caused by interpolation error during the thermal characterization (λ_0 is an interpolated value), or could be due to the limited accuracy of the optical interrogator. Nevertheless, since this is an experimental activity, a small margin of error must always be taken into account.

By looking at the results obtained so far, this thermal decoupling strategy seems to work very well, at least in the case of constant temperature.

4.1.3 Bending test at variable temperature (30°C/h)

The purpose of the test activity is to expose the Specimen 1 to 5 increasing load steps while letting the temperature vary cyclically, in order to examine if the temperature-induced effects on the FBG sensor can be effectively removed.

In order to submit the test specimen to a controlled temperature variation, it was placed inside the climatic chamber. The test setup, similar to what used for the thermal characterisation, consists of the use of the optical interrogator for reading the FBG wavelengths, the SHT85 sensor positioned in proximity of the optical sensor to detect the temperature useful for the compensation, and the climatic chamber, as well as a PC for data acquisition. In contrast to the thermal characterisation test, this time the specimen was clamped at one end on a 3D-printed support, and positioned inside the climatic chamber in a useful position for load application.

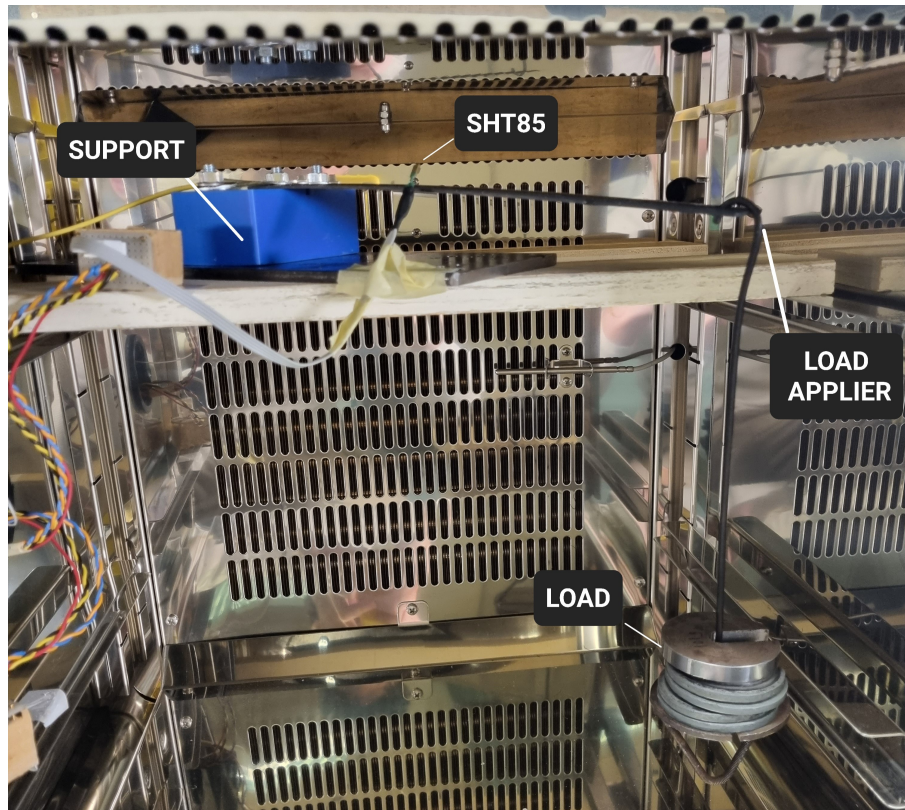


Figure 4.9: Climatic chamber setup for bending test

The test was designed so that the temperature varied by 15° for each load step and with a slope of $30^\circ\text{C}/\text{h}$, so 30 minutes of acquisition time was collected for each load step, for an overall duration of roughly 2h 30min. Considering that the specimen was thermally characterised between 0°C and 40°C , a temperature range from $+5^\circ\text{C}$ to $+35^\circ\text{C}$ was chosen. The load steps were: 0, 85, 180.2, 275.4, 376.4 [g], each applied close to the shear centre in order to lead a pure-bending in the specimen. The latter was oriented to induce a tensile stress on the optical line.

The time evolution of temperature and loads is shown below:

Static bending test - $30^\circ\text{C}/\text{h}$		
Load [g]	Temperature [$^\circ\text{C}$]	Duration [min]
0	$20 \rightarrow 35$	30
85	$35 \rightarrow 20$	30
180.2	$20 \rightarrow 5$	30
275.4	$5 \rightarrow 20$	30
376.4	$20 \rightarrow 35$	30

Table 4.2: Characteristics of Specimen 1 bending test ($30^\circ/\text{h}$)

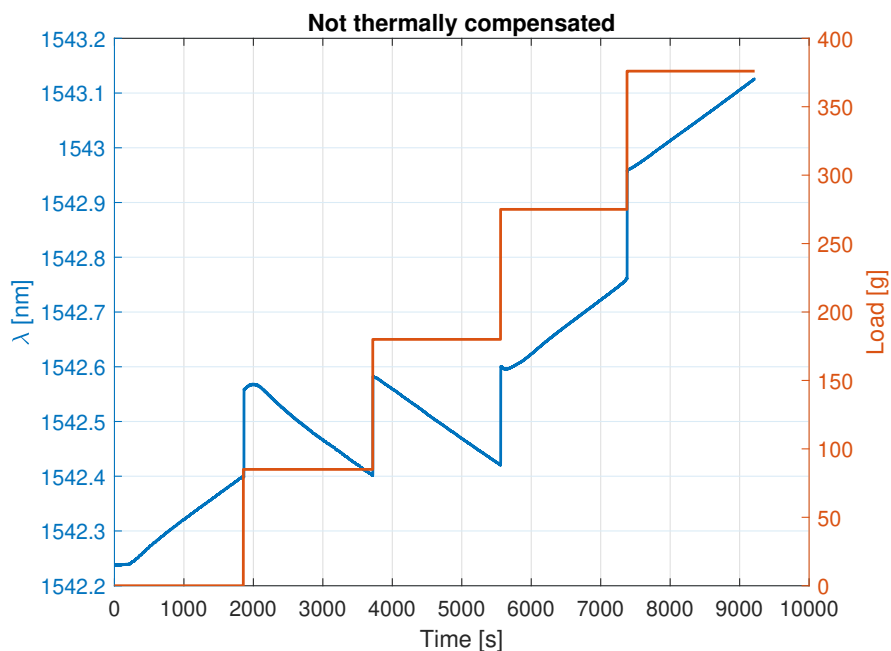


Figure 4.10: λ -time-load evolution for bending test at $30^\circ\text{C}/\text{h}$

In Figure 4.11 are plotted the time-evolution of: the measured wavelength (blue) and the temperature (red), while in Figure 4.10 the evolution of the wavelengths (blue) is correlated with the load steps (red).

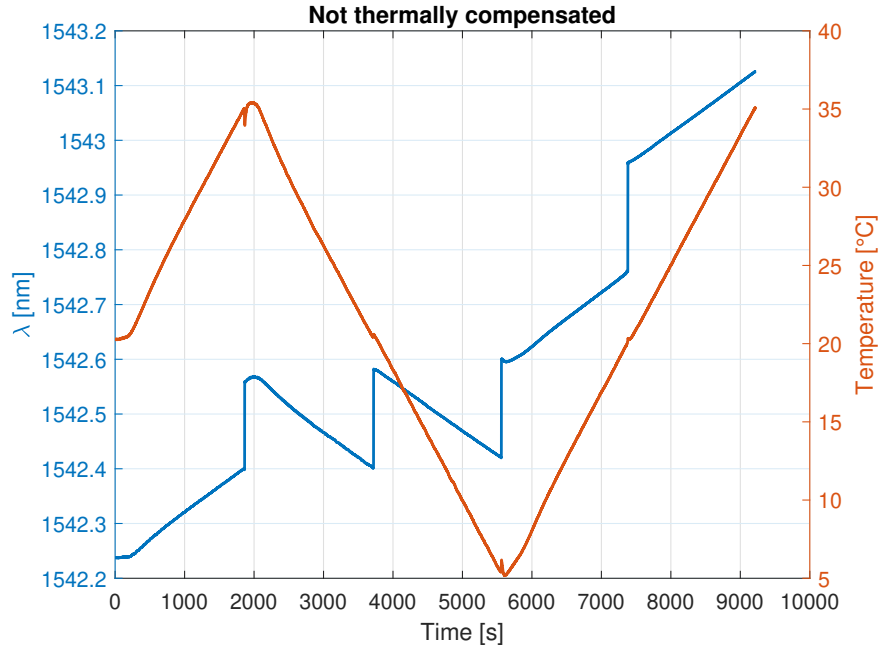


Figure 4.11: λ -time-T evolution for bending test at 30°C/h

When the load is still zero, the temperature increases (from 20 to 35°C), as does the wavelength. Once 35°C is reached, a load of 85 g is immediately applied and the temperature begins to decrease, so that an initial increase in wavelength is followed by a constant decrease due to the reduction in temperature. The same behaviour occurs during the third loading step.

When a temperature of 5°C is reached, on the other hand, a load is applied instantaneously but the temperature starts to increase. Thus, the FBG begins to experience not only an instantaneous increment in the reflected wavelength but also a constant increase in it due to the growing temperature, until it reaches 20°C. When this happens, a load is newly applied but the temperature continues to rise, so the same trend as just described is repeated. Once 35°C is reached, however, the acquisition ends.

There are also anomalous patterns near the temperature values at which a load is applied. This tendency is explained by the fact that, in order to physically apply a load to the specimen, it is necessary to open the climatic chamber door and manually insert the weight. Temperature fluctuations are greater the greater the temperature difference between the inside of the climate chamber and the outside

environment. At 20°C they are barely perceptible as the outside temperature was very similar.

As described before, known the temperature values it is possible to decouple the mechanical strain related contribute from the temperature one. Indeed, using the simple yet effective equation 4.10, it is possible to quantify the mechanical contribution $\Delta\lambda_\epsilon$.

Its time trend is reported below:

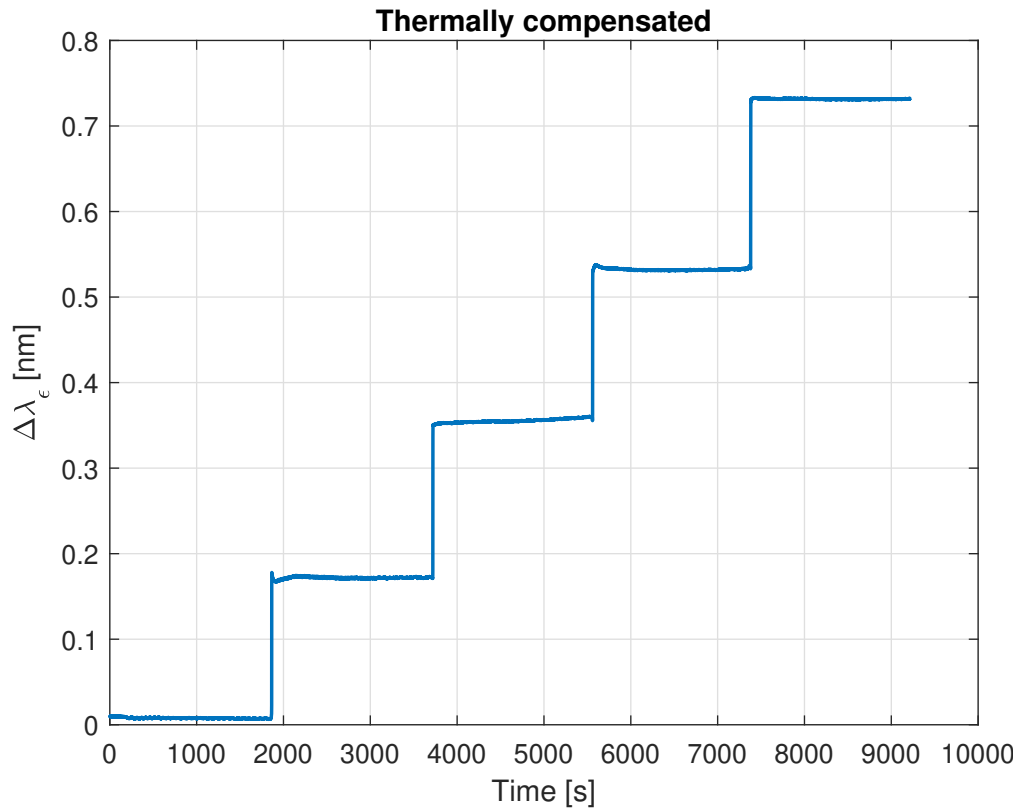


Figure 4.12: Thermal compensation for 30°C/h load test

The image above unequivocally demonstrates how the thermomechanical decoupling method works for the simple digital-optical system considered. The desired step-by-step pattern has been successfully derived from the raw data in Figure 4.11.

4.1.4 Bending test at variable temperature (60°C/h)

The purpose of the test is to verify if the thermal decoupling approach can be used also when the temperature variation increases. Theoretically, no differences should be expected in comparison to the previous situation. However, because we are considering an FBG sensor bonded to a composite structure and covered with a thick layer of epoxy resin, it was considered that testing its true sensitivity even at temperature variations of 60°C/h could be useful.

The test structure and setup are identical to the previous one: 5 load steps are applied to the specimen subjected to a purely bending load, and for each of them the temperature is varied by 15°C, for a total of 15 minutes of acquisition for each step. The overall duration of the test is approximately 1h 15 minutes and the temperature variation interval is kept between 5°C and 35°C. The load steps and the temperature interval are kept the same as the previous test also to increase the statistical validity of the results.

This characteristics are summarized below:

Static bending test - 60°C/h		
Load [g]	Temperature [°C]	Duration [min]
0	20 → 35	15
85	35 → 20	15
180.2	20 → 5	15
275.4	5 → 20	15
376.4	20 → 35	15

Table 4.3: Characteristics of Specimen 1 bending test (60°/h)

From Figures 4.14 and 4.13 no significant differences can be discerned compared to the previous test: the evolution of the measured wavelength is almost identical and is explained at 4.1.3

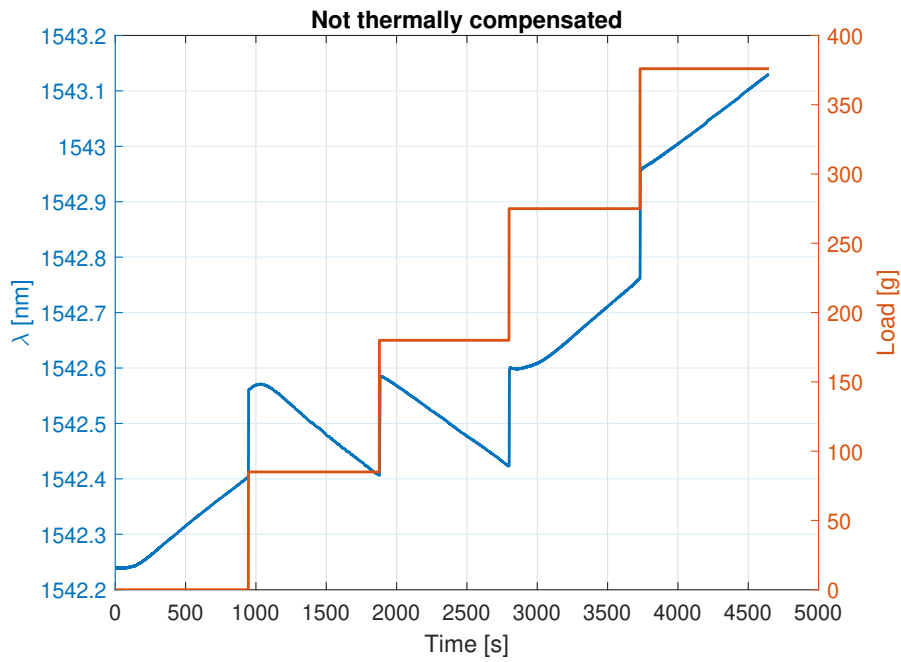


Figure 4.13: λ -time-load evolution for bending test at 60°C/h

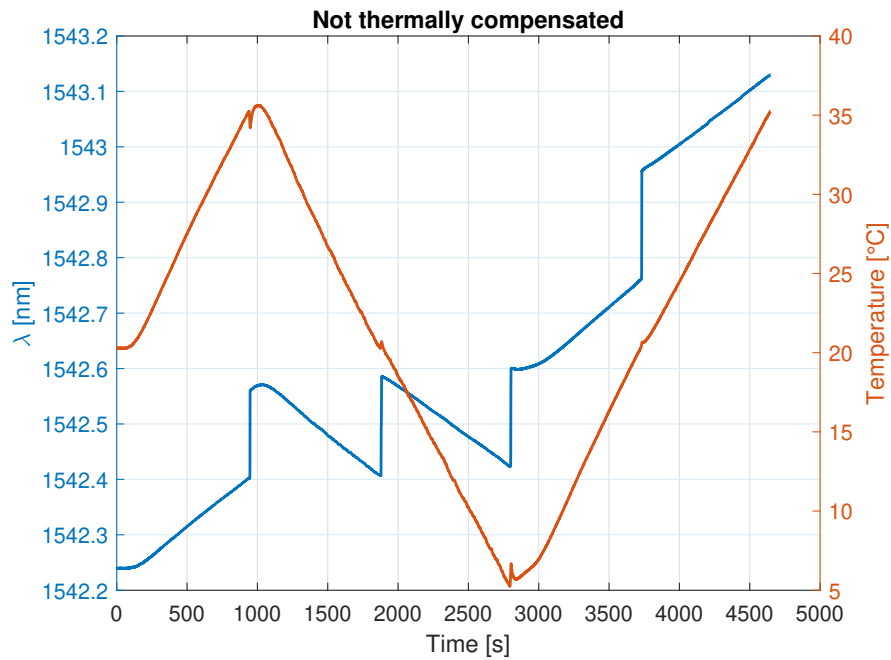


Figure 4.14: λ -time-T evolution for bending test at 60°C/h

By looking at the time evolution of the mechanical contribution $\Delta\lambda_\epsilon$ reported in Figure 4.15, seems to be a slight difference compared to previous case.

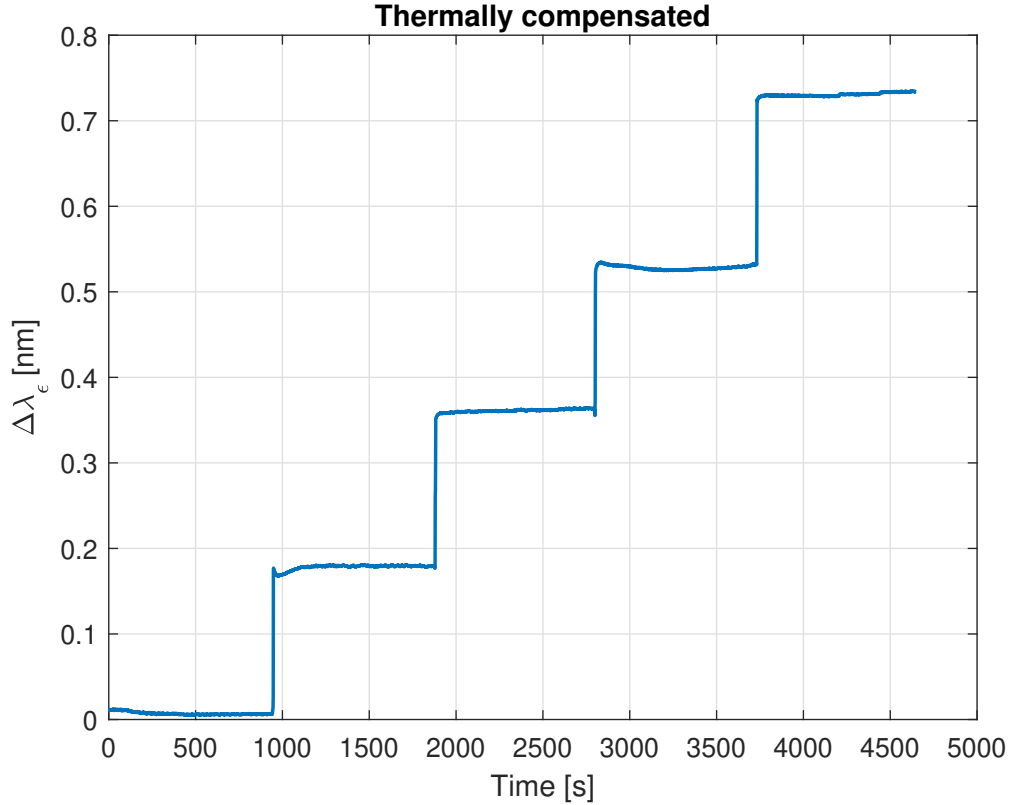


Figure 4.15: Thermal compensation for 60°C/h load test

From a comparison between this trend and the one shown in Figure 4.12, it would appear that in this latter test the stepped trend of the wavelengths is less regular, especially in relation to the second and fourth load steps. In reality, the not perfectly constant time trend of the $\Delta\lambda_\epsilon$ contribution recalls the oscillatory behaviour already highlighted in section 4.1.2 and relative to the constant temperature load test. In fact, by manually applying the load, it is almost inevitable to induce the specimen to a damped oscillatory phase. This phenomenon is encountered in the test carried out with a slope of 30°C/h as well, but in that case the wavelength acquisition interval had been 30 minutes and an oscillation of a few minutes was almost unnoticeable.

As a result, even with temperature oscillations of 60°C/h, the FBG can detect the temperature effects, and by using the thermal decoupling approach the two contributions $\Delta\lambda_\epsilon$ and $\Delta\lambda_T$ may be distinguished and quantified.

4.1.5 Thermal characterisation [-40 40]°C

A first thermal characterisation test was carried out for Specimen 1 in the temperature range [0 40]°C (section 4.1.1). The aim of this new activity is to verify whether it is possible to obtain reliable K_T and λ_0 coefficients, even if the temperature is varied between -40°C and +40°C.

The test setup remains unchanged from the previous one, while the temperature rate of change was set at 30°C/h. The structure of the test consisted of initially bringing the climatic chamber to 40°C and then starting data acquisition and temperature variation until -40°C.

The coefficients obtained through linear interpolation are summarized below, and compared to the results of the previous test:

Specimen 1		
	[-40 40] °C	[0 40] °C
K_T	0.0112	0.0112
λ_0	1542.0028 [nm]	1542.00097 [nm]

Table 4.4: Specimen 1 T.C. between -40°C and +40°C

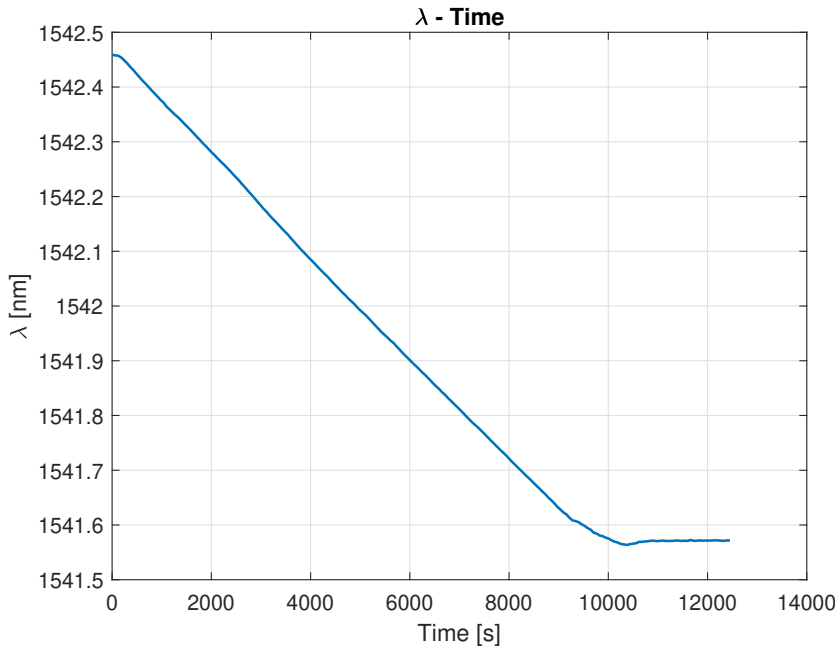


Figure 4.16: λ -time T.C. Specimen1 [-40 40]°C

A comparison of the data in Table 4.4 shows that the K_T remains unchanged, while there is an almost-imperceptible increase in λ_0 compared to the previous test ($1.19 \cdot 10^{-4} \%$).

Figure 4.16 shows the time evolution of the measured wavelengths. The existence of horizontal lines at the beginning and at the end indicates two time frames where the temperature was maintained (almost) constant. In fact, the climatic chamber took some time at the beginning of the test before starting the temperature decrease, while when -40°C was reached, few minutes passed before stopping the FBG data acquisition.

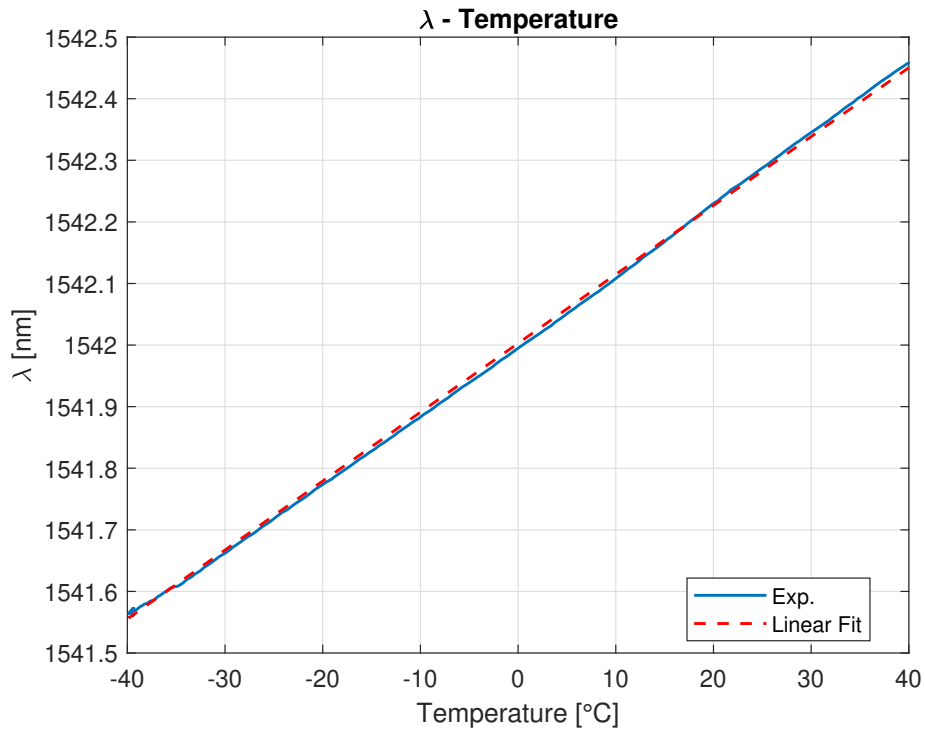


Figure 4.17: λ -Temperature T.C. Specimen1 [-40 40] $^\circ\text{C}$

The trend reported in Figure 4.17 unequivocally shows that there is no change in the slope of λ -Temperature line for an FBG bonded to a composite structure and covered by a layer of epoxy resin. As a result, even extending the temperature interval to negative values, a linear interpolation provides an excellent approximation of the real data and justifies the introduction of the linear coefficients previously discussed. In fact, a *Root Mean Square Error (RMSE)* of 0.007 has been calculated for the considered fit.

4.1.6 Determination of K_ε and $\Delta\varepsilon$

To be able to use the FBG sensor installed on Specimen1 as a mechanical strain sensor, it is necessary to know, in addition to the temperature and the related coefficients λ_0 and K_T , also the $K_\varepsilon = \lambda_B(1 - p_E)$ coefficient.

For an FBG sensor installed on a polymethyl methacrylate optical fibre, which is not installed on any surface and not pre-loaded, the strain-optic coefficient p_e is reported in Table 2.1. Considering Specimen1, however, the use of this term would involve a consistent margin of error due to both the installation on a surface and the pre-loading of the optical line. Hence it was decided to proceed with an experimental determination of the K_ε . The approach is to repeat the same bending load tests performed before and use a strain gauge to measure the deformation to which the FBG sensor is subjected as a function of the applied load.

Knowing that only pure-bending load-tests would be carried out, it was decided to mount a single strain gauge next to the FBG sensor, with the intention of measuring the (almost) same deformations as the optical sensor. A representation of the selected strain gauge is shown below:

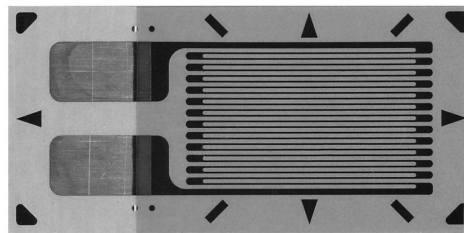


Figure 4.18: An example of strain gauge [14]

The following steps outline the sensor installation procedure:

- Identification of the optimal sensor location
- Cleaning of the installation surface
- Adhesive gluing of the sensor with a specific glue
- Wire soldering
- Application of a protective layer of epoxy resin
- Setting up the connection to the control unit

The final result is shown in Figure 4.19:

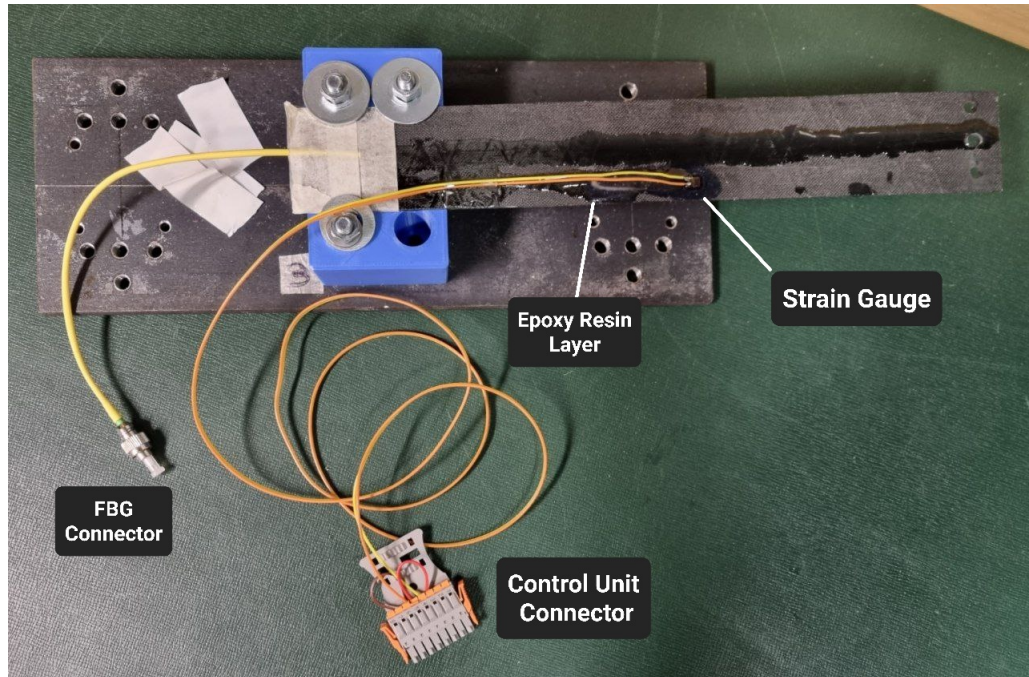


Figure 4.19: Strain Gauge configuration on Specimen 1

To carry out the experimental test activities, the strain gauge was powered by an HBM QuantumX MX1615B control unit which constituted an interface between the sensor and the computer. Data acquisition was carried out using HBM's catman@Easy program and the acquisition frequency was set to 20 Hz, as close as possible to the FBG sensor one (25Hz).

Bending test at constant temperature

The test was structured in much the same way as the previous ones carried out on Specimen 1 and consists of the application of 5 different load steps (0, 85, 180.2, 275.4, 376.4 [g]) at a constant temperature.

By placing the SHT85 sensor near the FBG, it is possible to know the temperature and remove its effect from the overall contribution measured by the SmartScan, as described in 4.1.2. Once the $\Delta\lambda_\epsilon$ is known, i.e. the relative contribution to the mechanical deformation, it is possible to exploit the deformations measured by the strain gauge ($\Delta\epsilon$) for each load step and find a correlation between $\Delta\lambda_\epsilon$ and the relative deformation.

Then the K_ε coefficient can be determined according to the following relationship:

$$K_\varepsilon = \frac{\Delta\lambda_B - \Delta\lambda_T}{\Delta\varepsilon} \quad (4.5)$$

The test setup is shown below:

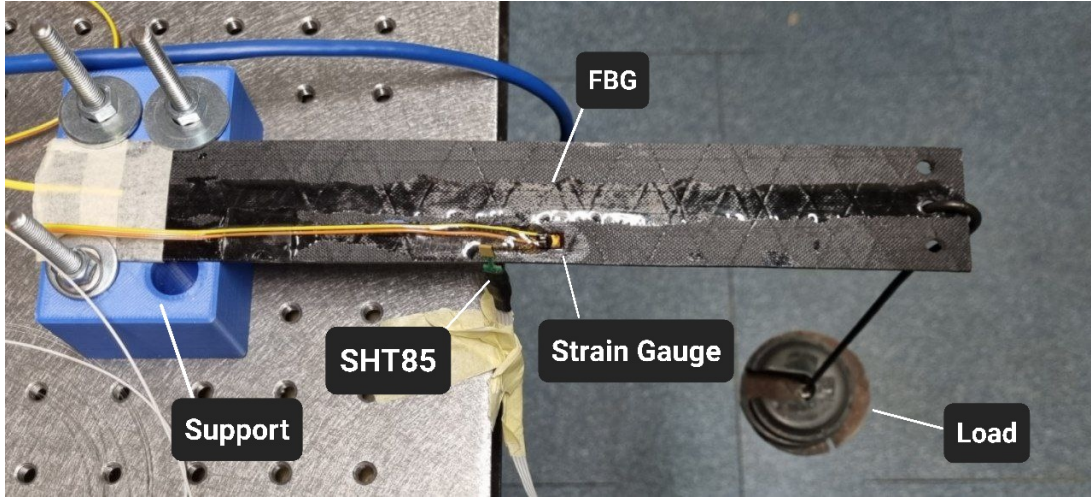


Figure 4.20: Specimen1 setup for bending test with strain gauge

As a first result in Figure 4.21 is shown the time-evolution of the measured wavelength (on the left) and the mechanical contribution $\Delta\lambda_\varepsilon$ (on the right). Even if this trend is almost the same as the one shown in 4.1.2, it is reported because it helps for a better understanding of the test's structure and constitutes an additional reference of the FBG behaviour.

The relationship between the mechanical contribution $\Delta\lambda_\varepsilon$ and the strain measured by the strain gauge is shown in Figure 4.22. The data provided by a linear interpolation between those quantities has been included as a dashed straight line. A comparison between the two curves, real and interpolated, shows that no appreciable differences can be noticed. The linearity of the relationship between the two quantities is confirmed by a *Root Mean Square Error (RMSE)* of 0.0126. This trend confirms that the K_ε remains constant as a function of the strain.

This characteristic justifies the introduction of the K_ε coefficient resulting from the linear interpolation:

$$\Delta\lambda_\varepsilon = \Delta\lambda_{\varepsilon,0} + K_\varepsilon \cdot \Delta\varepsilon \quad (4.6)$$

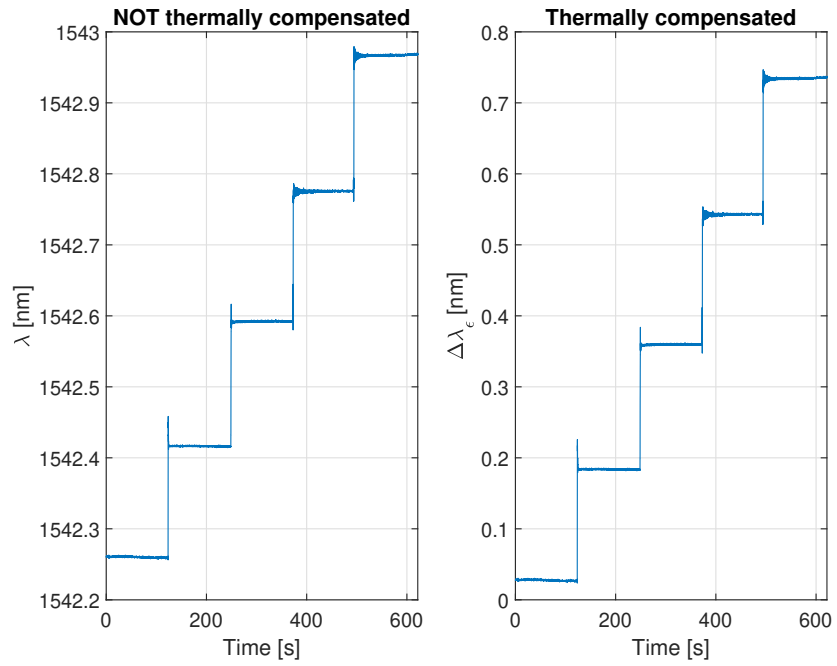


Figure 4.21: λ -time trend for bending test

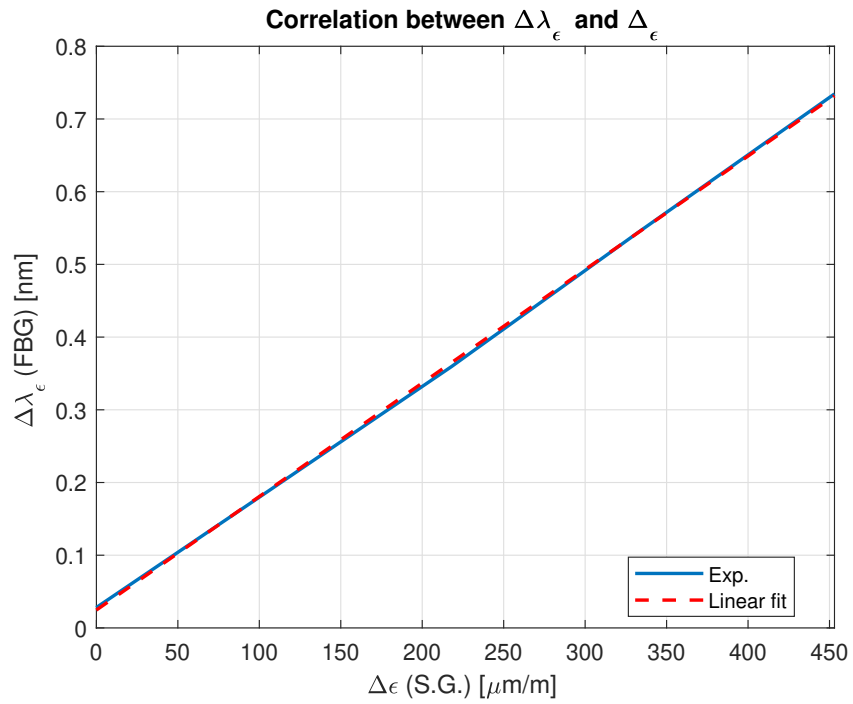


Figure 4.22: Specimen1: correlation between $\Delta\lambda_\epsilon$ and $\Delta\epsilon$

For Specimen1's FBG the following results have been obtained:

$$\begin{cases} K_\epsilon = 1561 \text{ [nm]} \\ \Delta\lambda_{\epsilon,0} = 0.0246 \text{ [nm]} \end{cases}$$

Ideally, $\Delta\lambda_{\epsilon,0}$ should be zero, since at zero strain the mechanical strain contribution detected by the FBG should be zero. In reality, this does not happen probably due to measurement and/or thermal characterisation errors.

In Figure 4.23 is represented the trend between the mechanical contribution $\Delta\lambda_\epsilon$, the applied load and the physical deformation sensed by the strain gauge $\Delta\epsilon$.

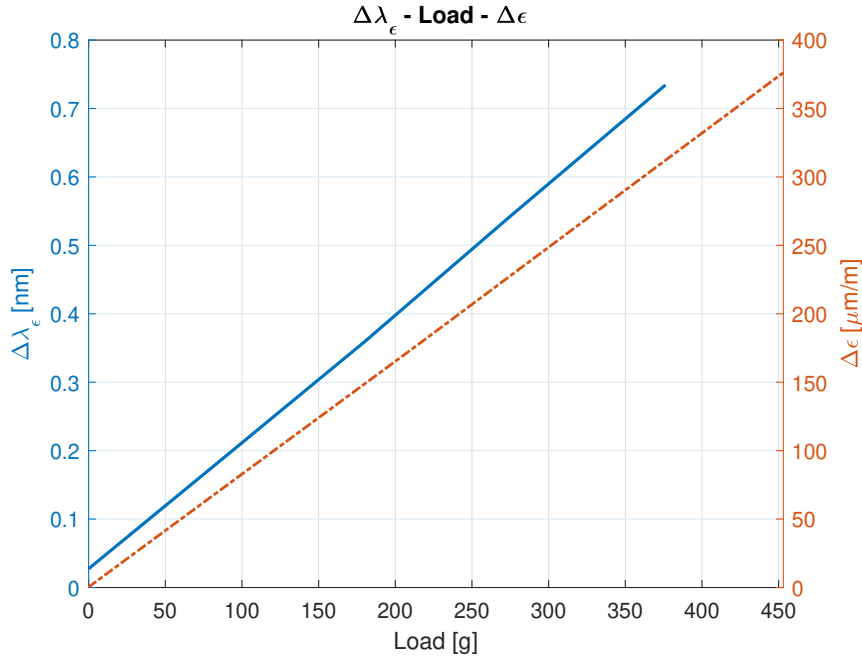


Figure 4.23: $\Delta\lambda_\epsilon$ -load- $\Delta\epsilon$ trend for bending test

As can be seen, the line relating to the mechanical contribution of the FBG starts from the non-zero value $\Delta\lambda_{\epsilon,0}$, unlike the strain gauge one. A difference in the slope between the two curves can be appreciated as well, which can be explained by the presence of the K_ϵ coefficient. In fact, according to 4.10:

$$\Delta\epsilon = \frac{\Delta\lambda_\epsilon - \Delta\lambda_{\epsilon,0}}{K_\epsilon} \quad (4.7)$$

since $K_\epsilon \neq 1$ the two lines must have different slopes.

Once the K_ε is known, it is possible to compute the strain measured by the FBG sensor. For this purpose, two different approaches are possible:

- 1 To calculate the deformation considering the raw value without removing the residual $\Delta\lambda_{\varepsilon,0}$, so using the relation: $\Delta\varepsilon = \frac{\Delta\lambda_\varepsilon}{K_\varepsilon}$
- 2 To calculate the deformation removing the residual $\Delta\lambda_{\varepsilon,0}$, by using equation 4.7

The first strategy provides an accurate measurement of what the sensor captures, as the data is not altered in any way. However, the second approach compensates for errors that cause the presence of a residual strain and, in this way, provides an output that is more consistent with the real deformations.

Being aware that every experimental activity involves a certain margin of error and because in this case it can be easily quantified, it was decided to choose the second approach to verify the quality of the output provided by the FBG, net of the errors.

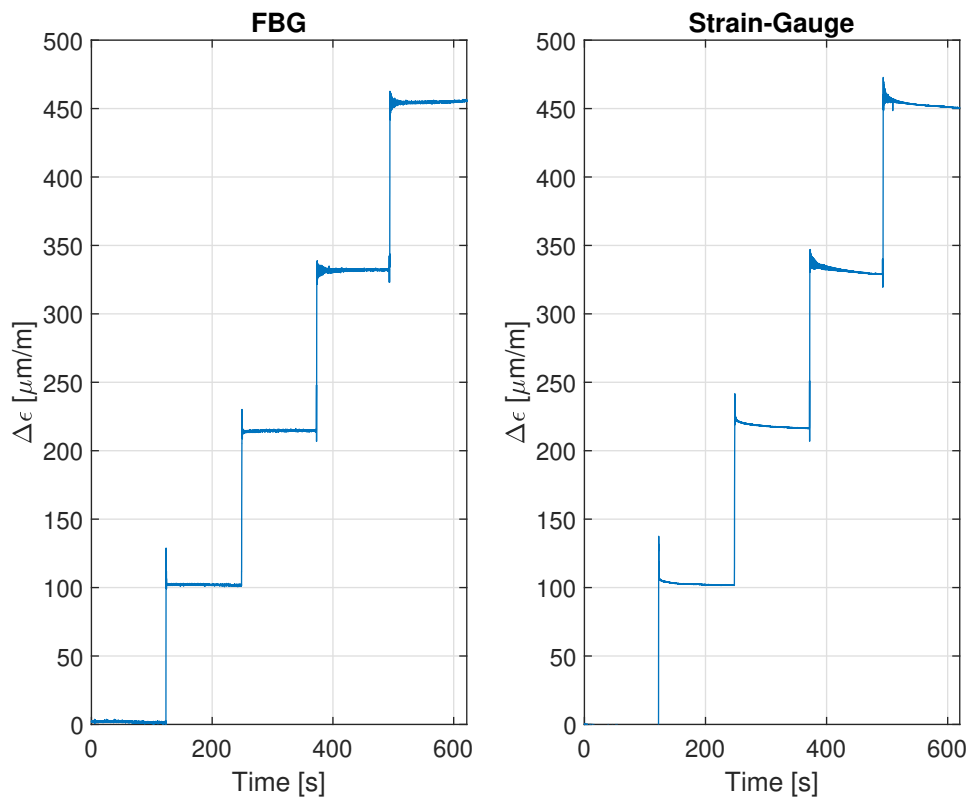


Figure 4.24: Specimen 1: $\Delta\varepsilon$ -time FBG vs SG

A graphical comparison with the strain trend measured by the strain gauge reveals that the results are very similar. However, the trend of what measured by the optical sensor is more stable compared to the strain gauge's one. Since a static load test has been conducted, in which the applied load did not vary over time, it would be expected a constant deformations for each load step (after the initial oscillatory phase). The trend which is closest to this behaviour is the FBG's one, that appears to be more reliable than the strain gauge.

In order to validate what has been measured in the constant-temperature test, a comparison between the deformation obtained for the different load tests was carried out. The aim was to check whether, by subjecting the specimen to the same load conditions but at different temperatures, the deformations captured by the FBG were the same.

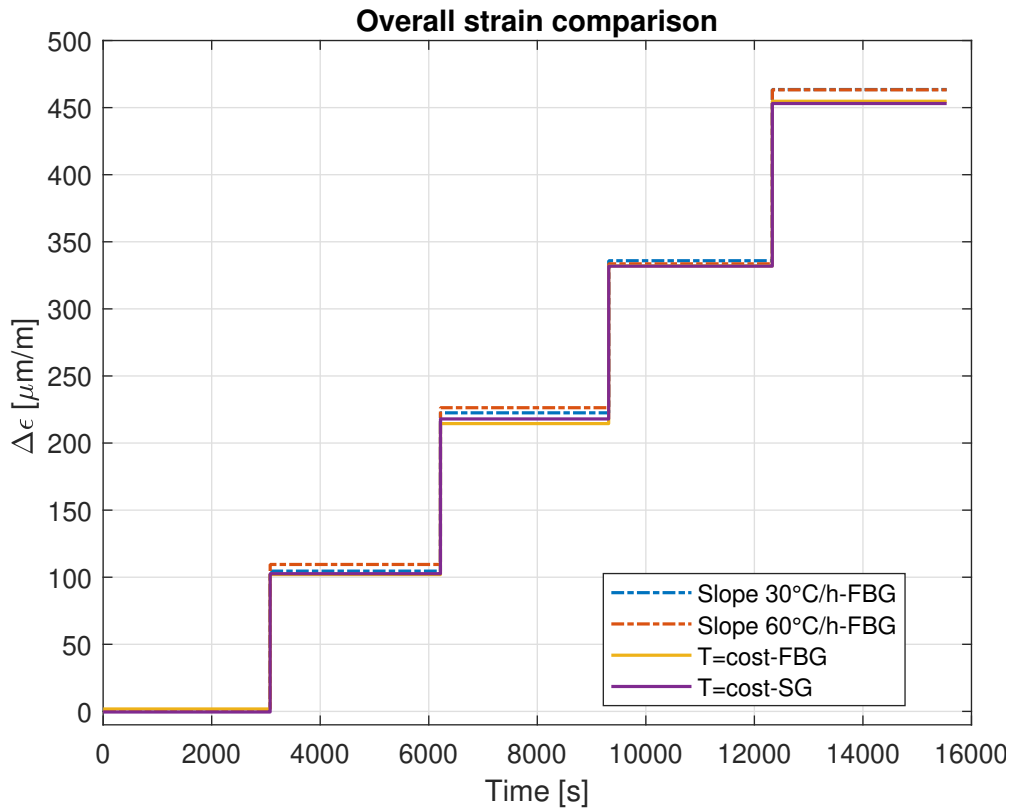


Figure 4.25: Specimen1: Overall strain comparison

In particular, Figure 4.25 shows the average deformations for each load step, measured by the:

- Strain gauge in load test at constant temperature

- FBG in load test at constant temperature
- FBG in load test at variable temperature with a slope of 30°C/h
- FBG in load test at variable temperature with a slope of 60°C/h

The same quantities are reported in the following table:

Specimen 1: $\Delta\varepsilon$ [$\mu\text{m}/\text{m}$]				
Load	SG 0°C/h	FBG 0°C/h	FBG 30°C/h	FBG 60°C/h
0g	-0.44	1.80	0	0
85g	102.63	101.99	104.54	109.51
180.2g	217.98	214.5	222.52	226.34
275.4g	331.84	332.03	335.88	333.57
376.4g	453.06	454.74	463.48	463.27

Table 4.5: Specimen 1: comparison between mechanical strain

The maximum absolute difference occurs for the second load step and is equal to 12 [$\mu\text{m}/\text{m}$], corresponding to about 5% of relative difference, which means that the results are consistent each other.

In light of what has been obtained, this thermomechanical decoupling strategy, allows the FBG sensor to provide reliable measurements of both temperature and mechanical strain.

On the other hand, a negative note is highlighted by a comparison with literature values for the strain coefficient K_ε . Table 4.6 shows a comparison between the experimental results and the theoretical expectations.

Specimen 1			
	Theoretical	Real	$\Delta\%$
K_ε [nm]	1215.3	1561	+28

Table 4.6: Specimen 1: K_ε comparison

When compared to the theoretical value, the K_ε undergoes an increase of 28%.

The results shown in Figure 4.22 revealed that the K_ε coefficient remains constant as a function of applied load, which means that a similar value would have been expected between the theoretical coefficient (obtained in the case of unloaded fiber) and the experimental one. Anyway, considering that the reference value is related

to an optical sensors which is not installed on any surface nor pre-loaded, such difference can be justified.

However, this difference can be influenced by other factors as well. One of them could be the imperfect alignment between FBG sensor and strain gauge, which causes the digital sensor to read a greater strain than the one perceived by the optical sensor. Another creditable hypothesis concerns the possibility that the specimen is subjected to torsion + bending instead of a pure-bending. In this way, since the strain gauge is positioned at a non-zero distance from the FBG, it would measure a strain component which can differ to FBGs one.

In conclusion, it can be affirmed that this thermomechanical decoupling methodology leads to very promising results.

4.2 Two independents optical systems

A key feature of using FBG sensors is the possibility of replacing conventional temperature and strain sensors, integrating both within a single one. In the previous chapter, an hybrid digital-optical system was analysed, which required a digital temperature sensor in order to be functional. With the aim of moving towards a complete independence from non-optical sensor and exploiting FBGs to their full potential, a system consisting solely of optical sensors will be presented in this chapter, comprising both Specimen1 and Specimen2.

The idea is to replicate the test activities carried out in the previous chapter by replacing the SHT85 sensor with an optical one. Since the FBG on Specimen1 has already been thermally characterised, and its strain coefficient K_ϵ has been determined experimentally, the plan is to use the FBGs installed on Specimen2 to measure the temperature, and to apply a load only on Specimen1.

In this way, by placing the Specimens close to each other, by using equation 4.3 it will be possible to determine the temperature and the mechanical strain to which Specimen1 is subjected. The equation is given below:

$$\Delta\lambda_{B_{Sp1}} = K_{\epsilon_{Sp1}} \Delta\epsilon_{Sp1} + K_{T_{Sp1}} \Delta T_{Sp2}$$

subscript $Sp1$ denotes a quantity relative to Specimen 1, while $Sp2$ indicates a quantity obtained from Specimen 2.

4.2.1 Thermal characterisation [0 40]°C

Since it is required to use Specimen 2 as a temperature sensor, a thermal characterisation needs to be carried out. It consists in determining the K_T coefficients of the FBGs through a direct correlation between wavelength variation and temperature variation. This procedure is feasible if the FBGs are not subject to mechanical deformation, i.e. if the applied load is zero.

In fact, in case of no load applied to the sample, equation 4.1 takes the following form:

$$\Delta\lambda_B = K_T \Delta T$$

The SHT85 was used to acquire the temperature. In this way, the ΔT is known, as is the $\Delta\lambda_B$ from the SmartScan and it is immediate to determine the K_T .

The experimental activity was carried out according to the following steps:

- Setting up Specimen 2 inside the climatic chamber
- Connecting the FBGs with the SmartScan
- Positioning two SHT85 sensors in close proximity to the FBGs, in order to capture as accurately as possible the same temperature perceived by the optical sensors
- Setting the temperature interval in the climatic chamber and its rate of change ($^{\circ}\text{C}/\text{h}$)
- Simultaneous start of the climate chamber cycle and the acquisition of the temperature and the FBG wavelengths
- End of acquisitions and temperature cycle
- Data storage and post-processing

The climatic chamber setup is shown below:

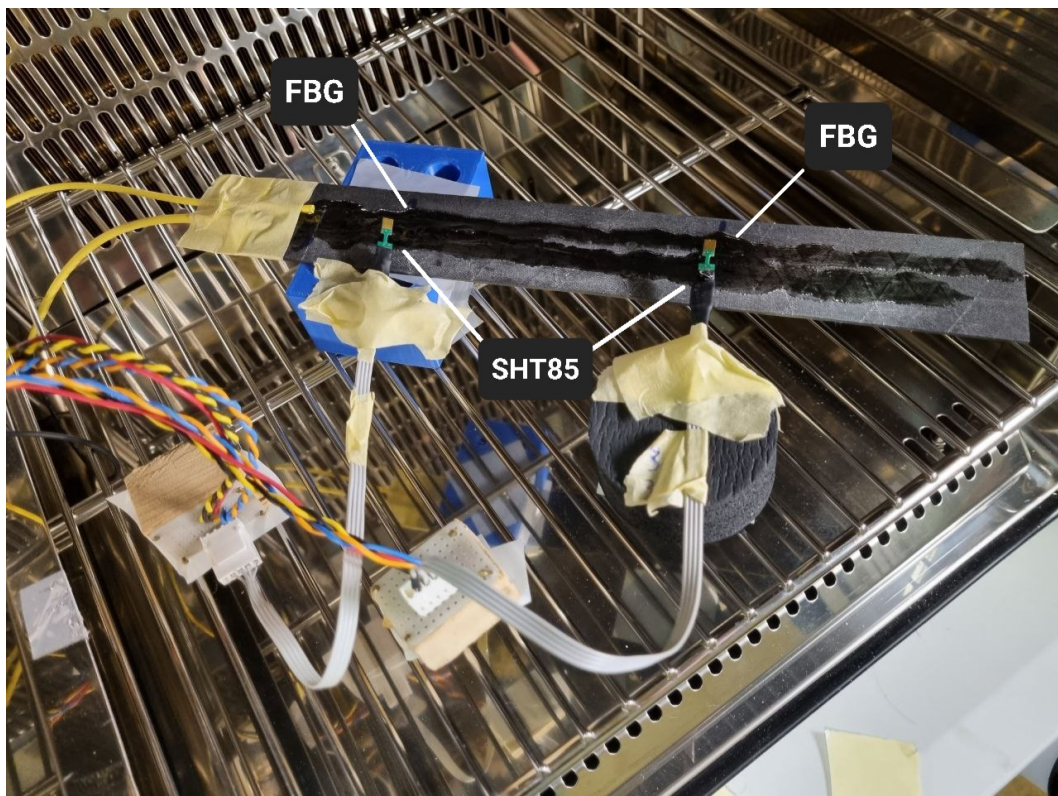


Figure 4.26: Specimen 2 setup for thermal characterization

In order to acquire as accurately as possible the temperature perceived by the FBGs, two SHT85 sensors have been employed. One of them has been positioned near the sensors in the root section of the sample, and the second one close to the remaining two, located near the free end of the specimen.

Since the variable temperature load tests will be performed in a positive $[5\ 35]^{\circ}\text{C}$ temperature range, the thermal characterisation has been carried out in the interval of 0°C to $+40^{\circ}\text{C}$, with a moderate rate of change of $20^{\circ}\text{C}/\text{h}$. The results of a thermal characterization carried out in the interval of $[-40\ +40]^{\circ}\text{C}$, with a slope of $30^{\circ}\text{C}/\text{h}$ can be found in [Appendix B].

The connection between the FBGs and the optical interrogator was made according to the following scheme:

- Channel 1 non-pretensioned optical line
- Channel 2 pre-tensioned optical line

The sensors are numbered in descending order according to the wavelengths, as illustrated in the image below:

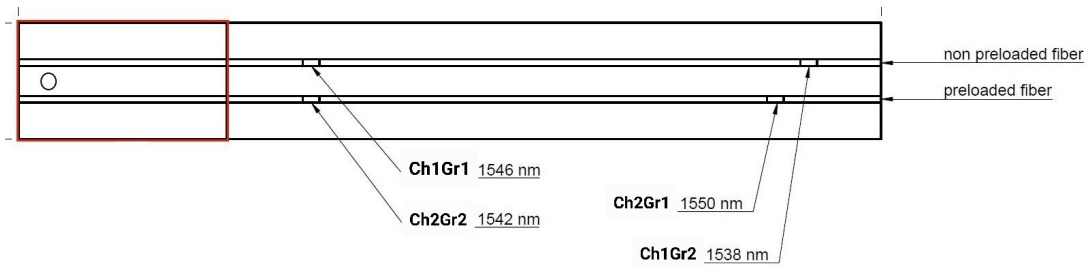


Figure 4.27: Specimen2 FBGs numbering

In Figure 4.28 and 4.29 are represented the λ -Temperature trends for both channels, and a linear fit is included for comparison as well. An almost-perfect linear correlation between the two quantities can be observed for Ch1Gr1 and Ch2Gr2 FBGs, and can be confirmed by the extremely low *Root Mean Square Error (RMSE)* of 0.0057 and 0.0060 respectively. A small deviation from the linear trend occurs near the upper limit of 40°C .

A slightly worst behaviour can be observed for sensors Ch1Gr2 and Ch2Gr1, for which the linear fit leads to a less faithful approximation of the real data, especially near the upper and lower temperature limits of -40°C and $+40^{\circ}\text{C}$. Anyway, the overall *Root Mean Square Error (RMSE)* of 0.0067 and 0.0077, indicates that even in this case, the linear fit represents a good approximation of the real data.

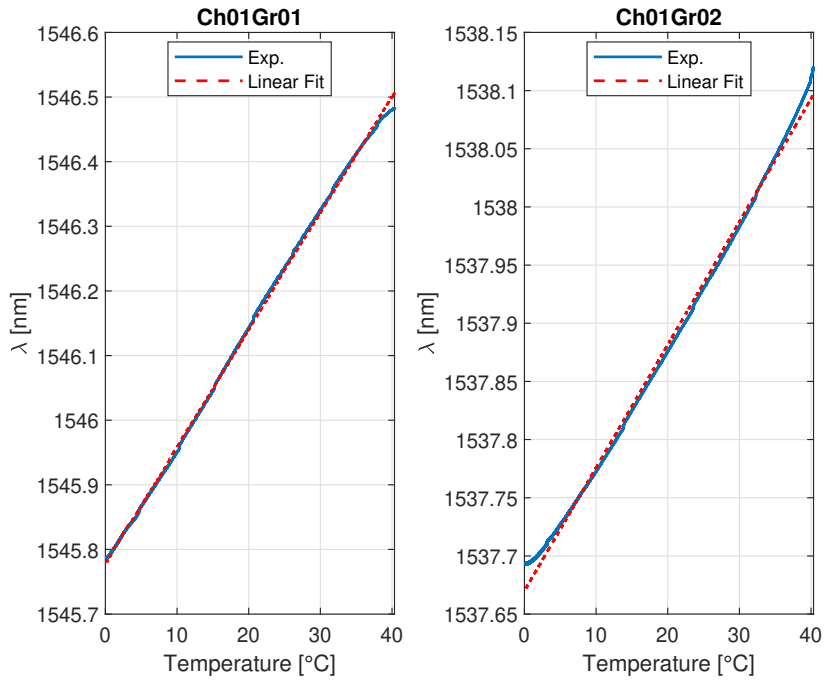


Figure 4.28: Specimen2 Channel 1 λ -Temperature

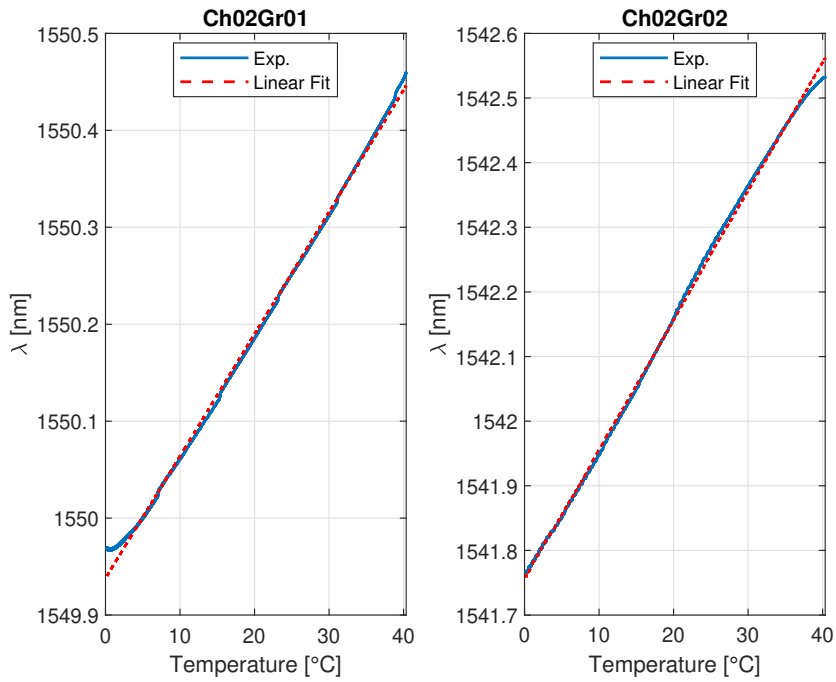


Figure 4.29: Specimen2 Channel 2 λ -Temperature

The linear interpolation leads to the following coefficients:

Specimen 2: T.C. [0 40]°C				
	Ch1Gr1	Ch1Gr2	Ch2Gr1	Ch2Gr2
K_T	0.0179	0.0106	0.0126	0.0198
λ_0 [nm]	1545.78	1537.67	1549.94	1541.76

Table 4.7: Specimen 2: T.C. [0 40]°C

Finally, it is possible to estimate the temperature perceived by the FBG as:

$$T = \frac{\lambda_m - \lambda_0}{K_T}$$

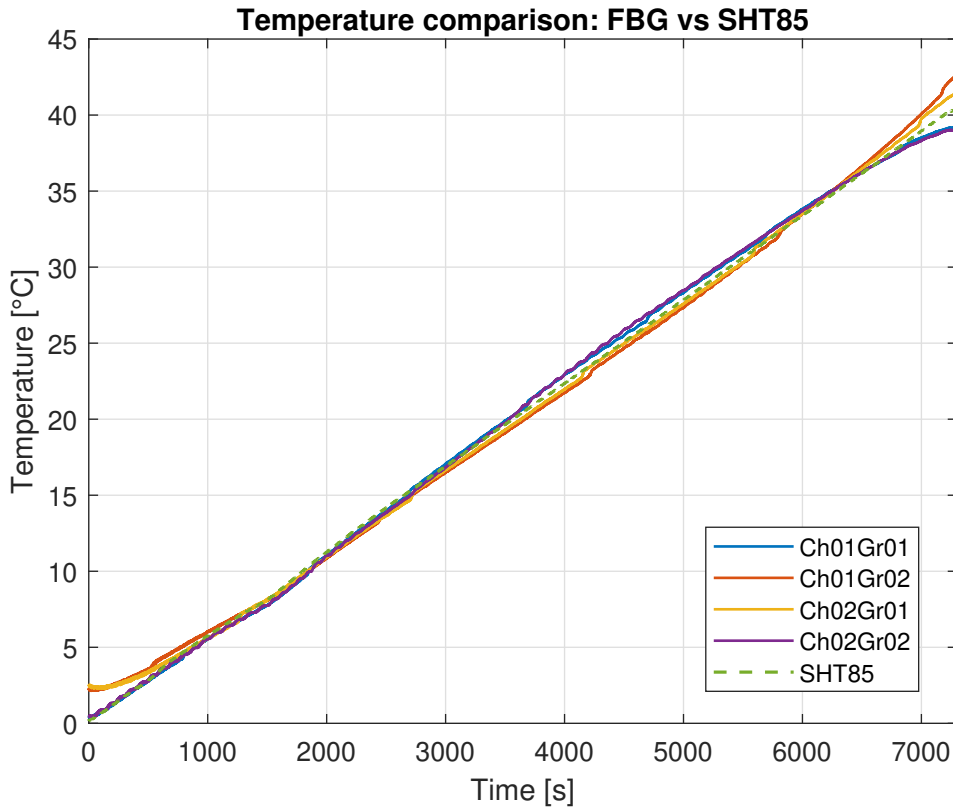


Figure 4.30: Specimen2 SHT85 vs FBG

A graphical comparison between the temperature perceived by the FBGs and measured by the SHT85 is shown in Figure 4.30. The graphical evolution of the FBGs-related quantities confirms a solid approximation of the real data, with a better results provided by the sensors Ch1Gr1 and Ch2Gr2.

4.2.2 Bending test at variable temperature (45°C/h)

The purpose of the test activity is to expose the Specimen 1 to 5 increasing load steps while letting the temperature vary cyclically, in order to examine if the temperature-induced effects on the FBG sensor can be removed even if using only optical systems. The temperature is acquired through Specimen 2.

In order to submit the test specimens to a controlled temperature variation, they were placed inside the climatic chamber. The test setup is composed by Specimen 1 and 2, which are positioned close to each other in order to avoid temperature gradients. An SHT85 sensor is employed as well, but for comparison purpose. The FBGs are connected to the optical interrogator for wavelengths acquisition, the SHT85 is positioned between the specimens to detect almost the same temperature, and a PC is used for data acquisition.

Both the specimens are clamped at one end on a 3D-printed support and located inside the climatic chamber in a useful position for load application. Specimen 2 was clamped on the support only to be at the same height of the other one.

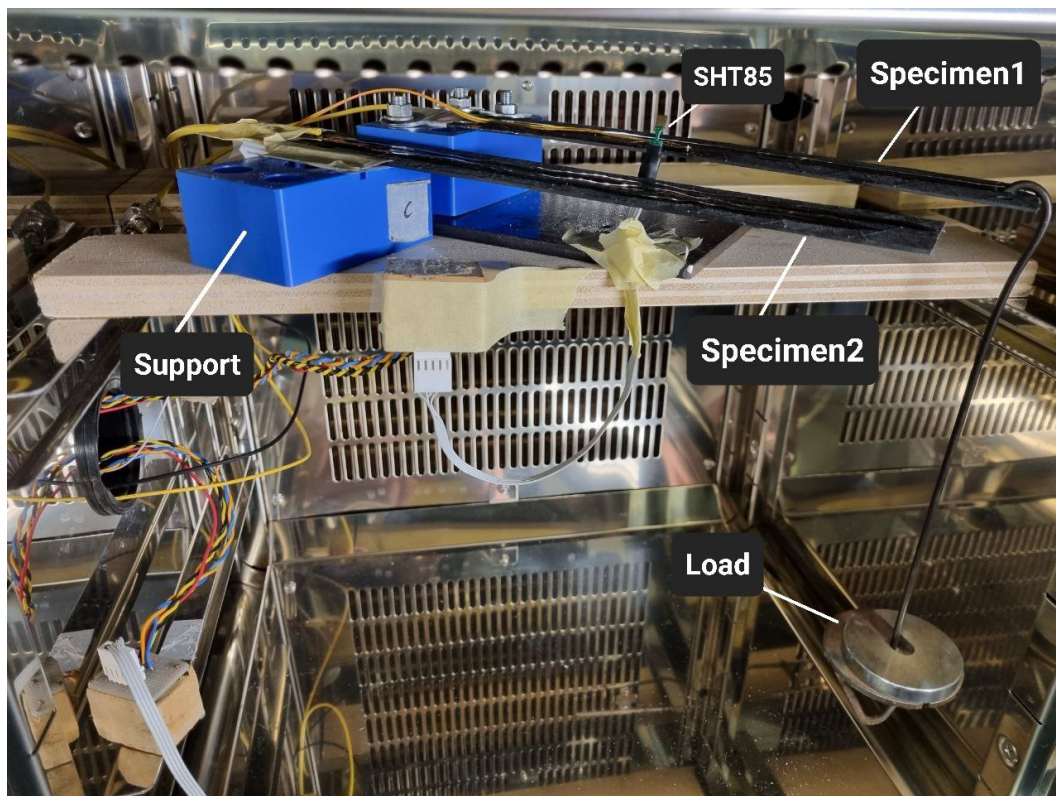


Figure 4.31: Climatic chamber setup for bending test

The test was designed so that the temperature varied by 15° for each load step and with a slope of 45°C/h , so 20 minutes of acquisition was collected for each load step, for an overall duration of roughly 1h 40min. A temperature range from $+5^\circ\text{C}$ to $+35^\circ\text{C}$ was chosen in order to be consistent with the previous tests. The load steps were: 0, 85, 180.2, 275.4, 376.4 [g], each applied close to the shear centre of Specimen1 with the aim to lead a pure-bending in the specimen, which was oriented to induce a tensile stress on the optical line.

The time evolution of temperature and loads is shown below:

Static bending test - 30°C/h		
Load [g]	Temperature [$^\circ\text{C}$]	Duration [min]
0	$20 \rightarrow 35$	20
85	$35 \rightarrow 20$	20
180.2	$20 \rightarrow 5$	20
275.4	$5 \rightarrow 20$	20
376.4	$20 \rightarrow 35$	20

Table 4.8: Characteristics of Specimen 1 bending test ($30^\circ/\text{h}$)

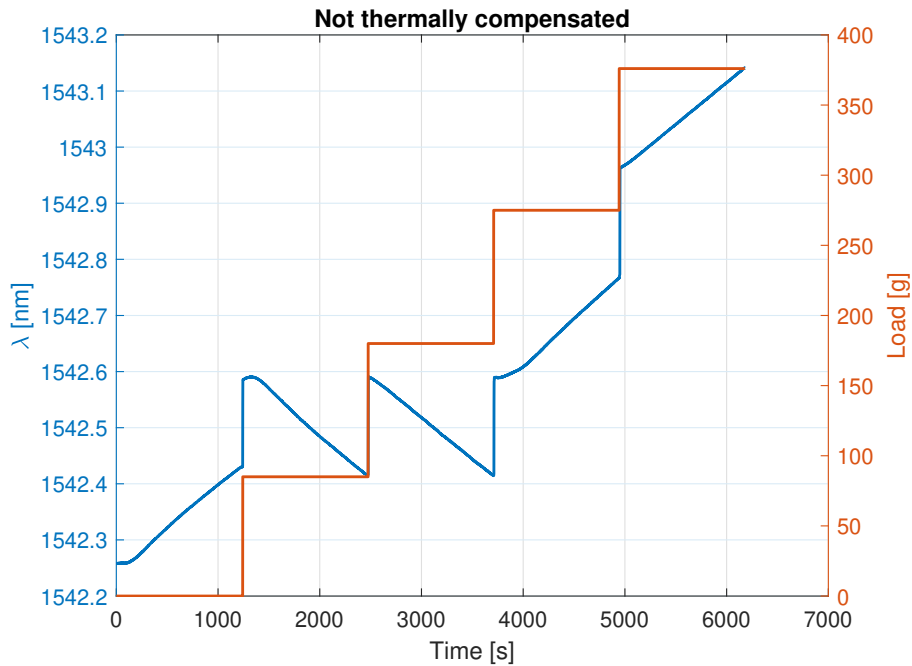


Figure 4.32: λ -time-load evolution for bending test at 45°C/h

In Figure 4.32 are plotted the time-evolution of: the measured wavelength of Specimen1 FBG (blue) and the temperature measured by the SHT85 (red), while in Figure 4.10 the same wavelength evolution (blue) is correlated with the load steps (red).

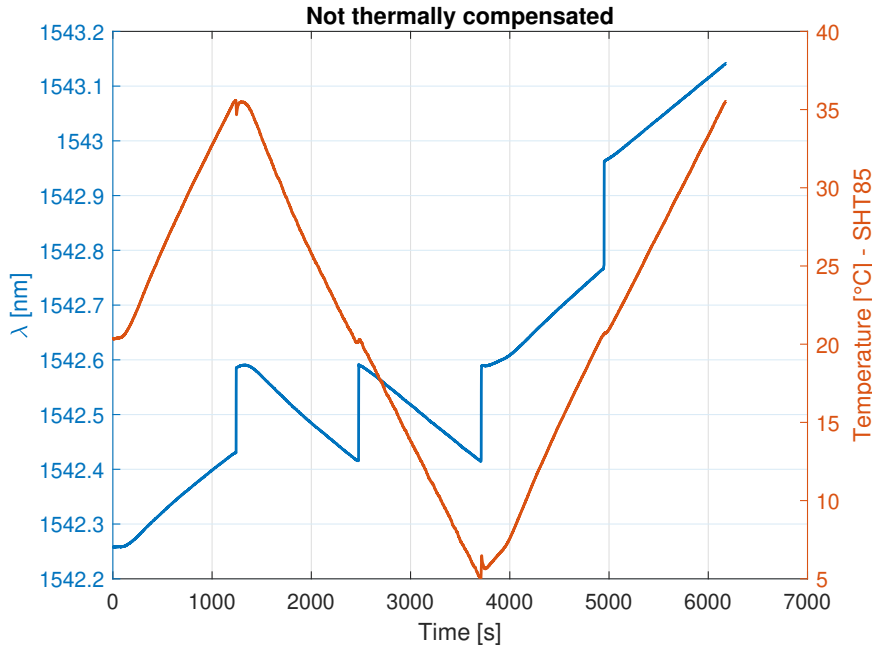


Figure 4.33: λ -time-T evolution for bending test at $45^{\circ}\text{C}/\text{h}$

When the load is still zero, the temperature increases (from 20 to 35°C), as does the wavelength. Once 35°C is reached, a load of 85 g is immediately applied and the temperature begins to decrease, so that an initial increase in wavelength is followed by a constant decrease due to the reduction in temperature. The same behaviour occurs during the third loading step.

When a temperature of 5°C is reached, on the other hand, a load is applied instantaneously but the temperature starts to increase. Thus, the FBG begins to experience not only an instantaneous increment in the reflected wavelength but also a constant increase due to the growing temperature, until it reaches 20°C . When this happens, a load is newly applied but the temperature continues to rise, so the same trend as just described is repeated. Once 35°C is reached, however, the acquisition ends.

There are also anomalous patterns near the temperature values at which a load is applied. This tendency is explained by the fact that, in order to physically apply a load to the specimen, it is necessary to open the climatic chamber door and manually insert the weight. Temperature fluctuations are greater the greater the

temperature difference between the inside of the climate chamber and the outside environment. At 20°C they are barely perceptible as the outside temperature was very similar.

The trend reported in the previous image, shows the temperature perceived by the SHT85, which is used only as a reference value. In Figure 4.34 a comparison between the reference SHT85 temperature value and the FBGs sensed one is reported.

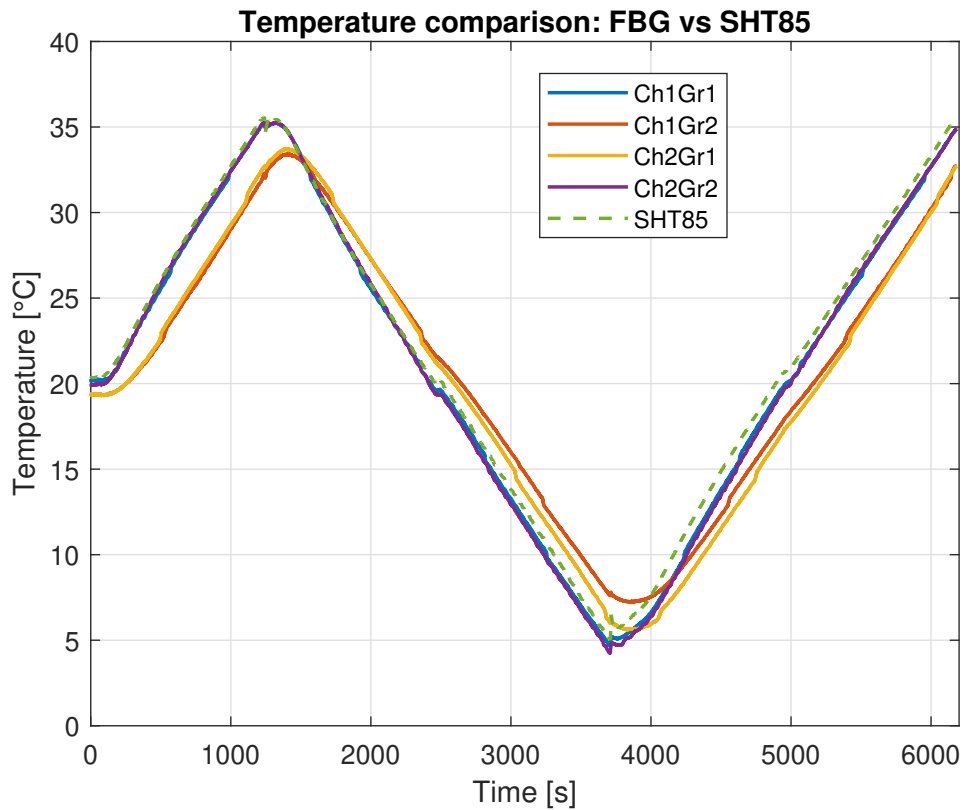


Figure 4.34: Temperature comparison: FBGs vs SHT85

The FBGs are numbered according to the same convention used in 4.2.1.

Temperature comparison				
	Ch1Gr1	Ch1Gr2	Ch2Gr1	Ch2Gr2
RMSE	0.6261	2.4521	2.4868	0.7564

Table 4.9: Temperature comparison: RMSE

An estimation of the quality of the results is given by the *Root Mean Square Error (RMSE)* which is reported in Table 4.9. As can be seen, the same behaviour highlighted in section 4.2.1 is experienced. In fact, only Ch1Gr1 and Ch2Gr2 provides an acceptable estimation of the temperature, which means that only such sensors can be used for thermal compensations.

Anyway, for the sake of completeness, a thermal compensation is carried out using all the FBGs. Using equation 4.10:

$$\Delta\lambda_\epsilon = \Delta\lambda_B - \Delta\lambda_T$$

it is possible to quantify the mechanical strain contribution $\Delta\lambda_\epsilon$ that the optical sensor on Specimen1 experiences.

In Figures 4.35 and 4.36 the time evolution of the mechanical contribution is reported and compared with the reference value that could have been obtained through the SHT85 temperature sensor.

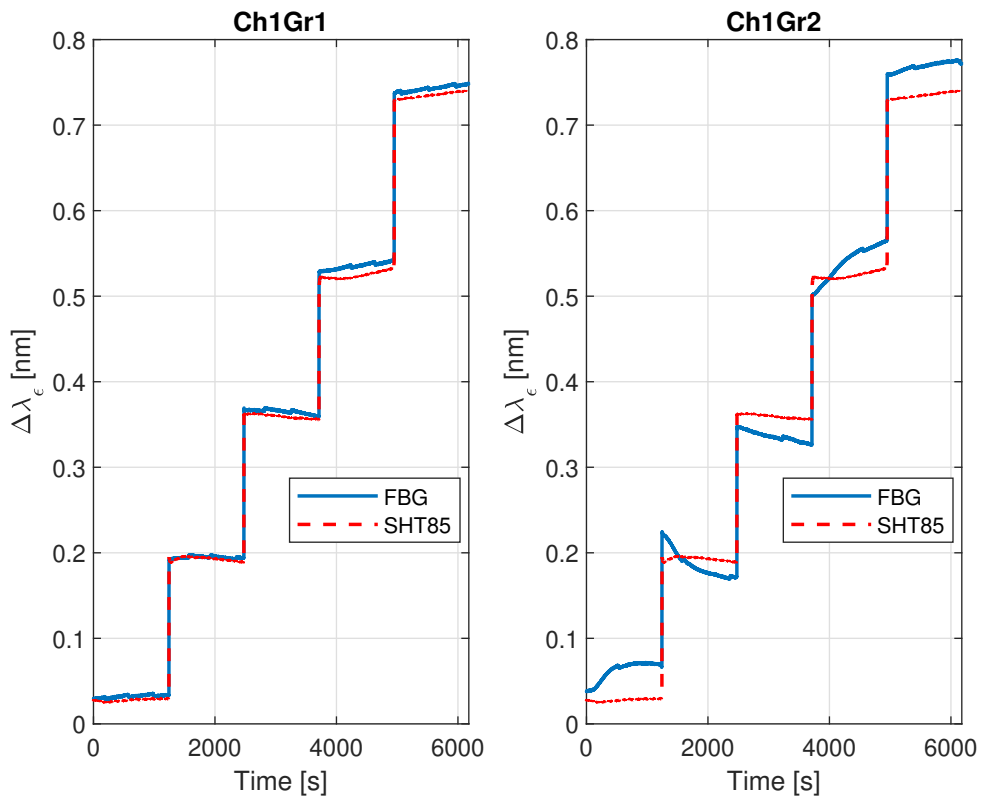


Figure 4.35: Thermal compensation: channel 1

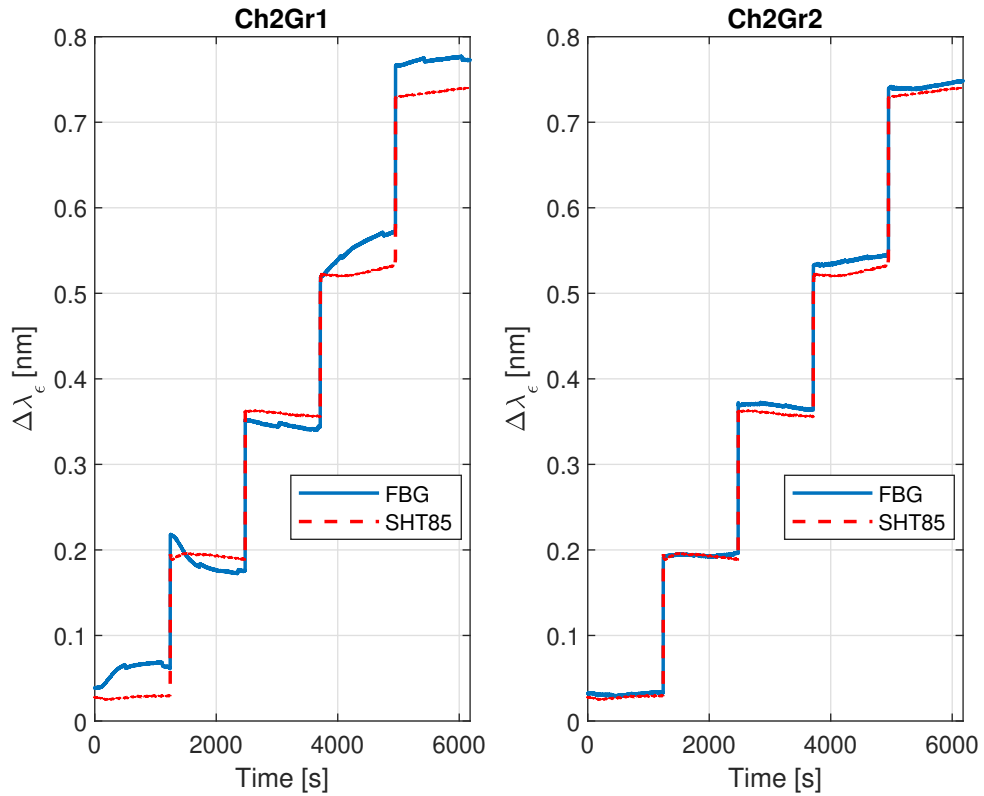


Figure 4.36: Thermal compensation: channel 2

Since the thermomechanical decoupling is deeply affected by the quality of the results of the thermal characterization, and so, by the quality of the estimation of the temperature, it is evident that Ch2Gr1 and Ch1Gr2 provides unacceptable results.

On the other hand, the FBGs located near the free end of Specimen2, i.e. Ch1Gr1 and Ch2Gr2, which have shown good results since the thermal characterization, are able to provide very good results also in terms of thermomechanical decoupling.

Finally, this optical-only system proved the feasibility of thermomechanical decoupling using only optical sensors, but at the same time highlighted the importance to carry out a reliable thermal characterization. As a corollary, in [Appendix B] the results of this test have been obtained using an less-reliable thermal characterization.

4.3 A unique fully-autonomous optical system

One of the advantages of using FBG sensors is the ability to integrate multiple functions into a single component, allowing for a transition from traditional sensors.

Architectures consisting of a digital-optical system and, later, two optical systems mechanically disconnected from each other were examined in previous chapters. After demonstrating the feasibility of using FBGs as mechanical deformation and temperature sensors, the goal is to develop and analyze an optical system composed of a single component that is completely independent of other types of sensors, since it would represent the main application possibility in the aerospace field.

The system in this context will be Specimen2, which will be subjected to static variable-load tests, in a variable temperature environment.

In order to decouple the effects, at least two FBGs need to be employed and exposed to the same temperature and strain conditions. Considering equation 4.3 for both sensors, the following linear system is obtained:

$$\begin{Bmatrix} \Delta\lambda_1 \\ \Delta\lambda_2 \end{Bmatrix} = \begin{bmatrix} K_{\varepsilon_1} & K_{T_1} \\ K_{\varepsilon_2} & K_{T_2} \end{bmatrix} \cdot \begin{Bmatrix} \Delta\varepsilon \\ \Delta T \end{Bmatrix} \quad (4.8)$$

Where:

- $\Delta\varepsilon$ and ΔT other than being the unknowns of the problem, represent the strain and temperature changes to which both sensors are subjected
- $K_{\varepsilon_{1,2}}$ and $K_{T_{1,2}}$ are the strain and temperature coefficients
- $\Delta\lambda_{1,2} = \lambda_{m_{1,2}} - \lambda_{0_{1,2}}$ represents the wavelength shift to which the FBGs are subjected

4.3.1 Determination of K_ε and $\Delta\varepsilon$

To be able to use the FBGs installed on Specimen2 as mechanical strain sensors and solving the linear system 4.8, it is necessary to know, other than the λ_0 and K_T coefficients (provided by the thermal characterisation at 4.2.1), also the $K_\varepsilon = \lambda_B(1 - p_E)$ coefficients.

For an FBG sensor installed on a polymethyl methacrylate optical fibre, which is not installed on any surface nor pre-loaded, a reference value can be obtained from Table 2.1. However, as already discovered for Specimen1, the theoretical value of the strain coefficient differs with the experimental one. Hence, an experimental determination needs to be carried out for Specimen2 as well, but since the previous analysis shown that only the optical sensors located near the free end provided a reliable temperature measure, the strain coefficients will be determined only for those two sensors.

The approach is the same as reported in 4.1.6 and consists in installing a strain gauge near the FBGs in order to measure the deformation to which they are subject when performing a static variable-load test, in order to find a correlation between the applied load and the mechanical strain.

With the aim of performing pure-bending load tests, Specimen2 was drilled close to the elastic axis so that the load could not induce any torsion. Then, a strain gauge was installed next to the FBG sensors, with the intention of measuring (almost) the same deformations as the optical sensors.

The following steps outline the installation procedure:

- Identification of the optimal sensor location
- Cleaning of the installation surface
- Adhesive gluing of the sensor with a specific glue
- Wire soldering
- Application of a protective layer of epoxy resin
- Setting up the connection to the control unit

Then, the strain gauge was powered by an HBM QuantumX MX1615B control unit which worked also as an interface between the sensor and the PC. Data acquisition was carried out using HBM's catman@Easy program and the acquisition frequency was set to 20 Hz, as close as possible to the FBGs one (25Hz).

The result (without the protective epoxy layer yet) is illustrated below:

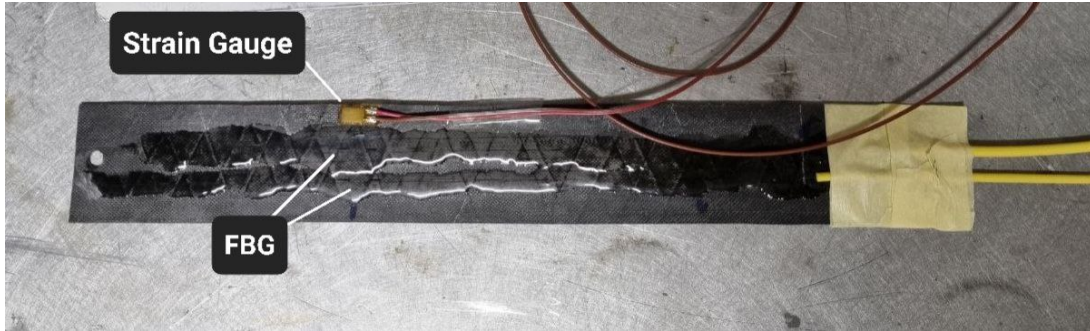


Figure 4.37: Strain Gauge configuration on Specimen 2

Bending test at constant temperature

The test consists of the application of 5 different load steps on Specimen 2 (0, 85, 180.2, 275.4, 376.4 [g]), at a constant temperature. The loads are applied every 2 minutes. The structure is clamped on an optical breadboard through a 3D-printed support and is oriented so that the load induce a tensile stress on the fiber.

The thermal decoupling was carried out according to the digital-optical strategy introduced in 4.1.2, and by means of the SHT85 digital sensor, which was placed near the FBGs in order to reduce as much as possible the temperature gradients.

Once the thermal effect is removed, it is possible to exploit the deformations measured by the strain gauge ($\Delta\varepsilon$) for each load step and find a correlation between $\Delta\lambda_\varepsilon$ and the relative deformation.

In fact, the K_ε coefficient can be determined according to the following relationship:

$$K_\varepsilon = \frac{\Delta\lambda_B - \Delta\lambda_T}{\Delta\varepsilon} \quad (4.9)$$

where λ_m is the wavelength measured by the SmartScan and $\Delta\lambda_T$ is the thermal contribution.

The test setup is shown below:

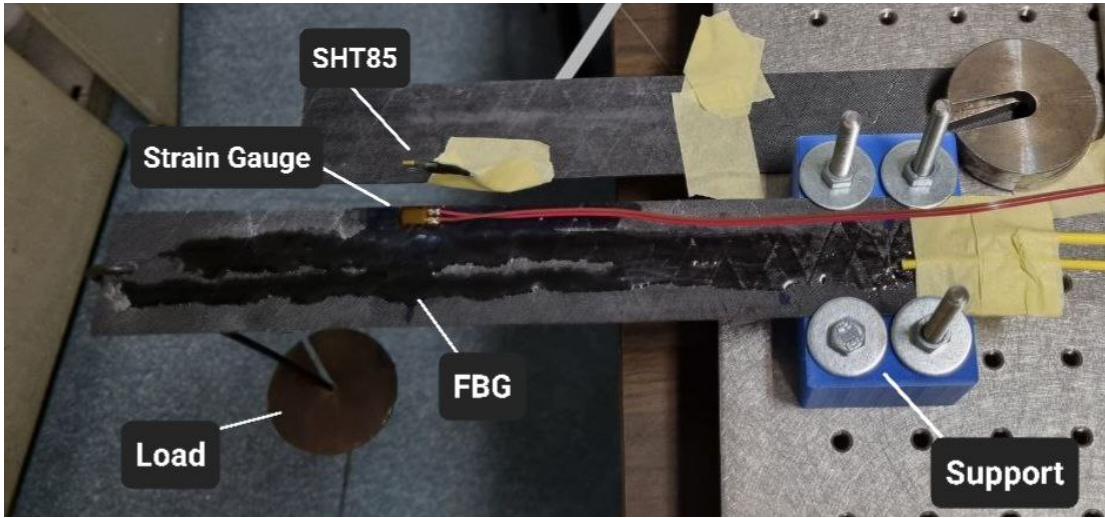


Figure 4.38: Specimen2 setup for bending test with strain gauge

The connection scheme between the FBGs and the optical interrogator is common to the previous test activities and is illustrated below:

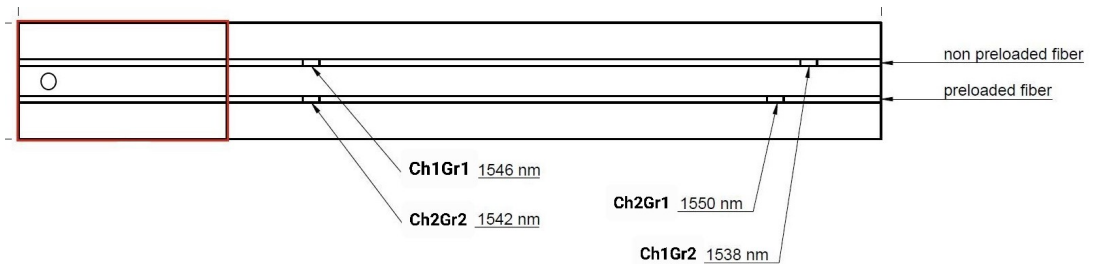


Figure 4.39: Specimen2 FBGs numbering

Sensors *Ch2Gr1* and *Ch1Gr2* are not considered in any of the following activities, since they provide less-reliable results.

As a first result in Figures 4.40 and 4.41 the time evolution of the measured wavelength (on the left) and the mechanical contribution $\Delta\lambda_e$ (on the right) are shown for *Ch1Gr1* and *Ch2Gr2*. As can be observed, the thermal contribution can be effectively removed from the measured wavelength also for Specimen2 FBGs.

However, an unusual behaviour can be detected for both the sensors regarding the first two load steps, when a slight wavelength decrease is experienced even if the load (so, the deformation) does not vary. For *Ch1Gr1*, load step number 5 is affected also by an abnormal oscillatory trend, which is not caused by a specimen oscillation, as confirmed by *Ch2Gr2*.

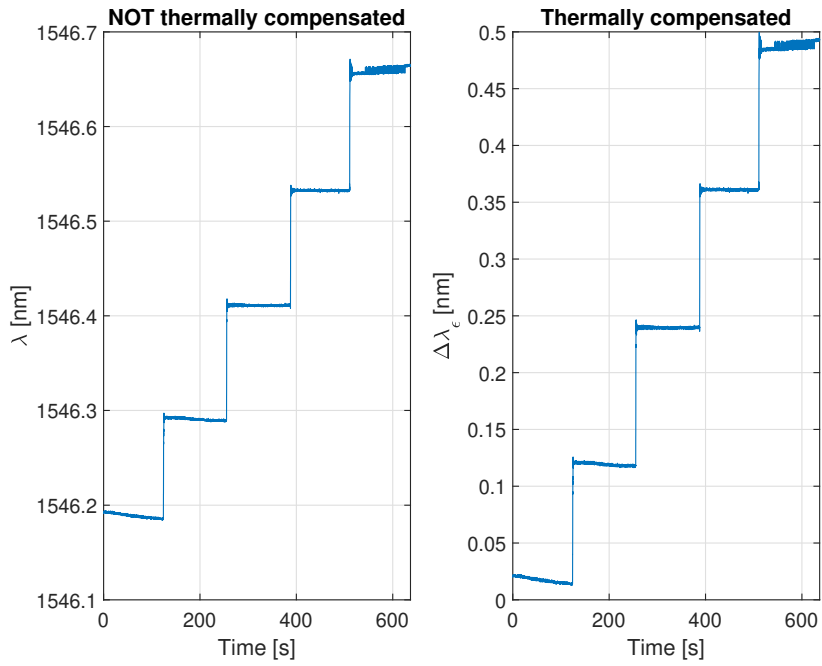


Figure 4.40: Specimen 2: Ch1Gr1 λ -time trend

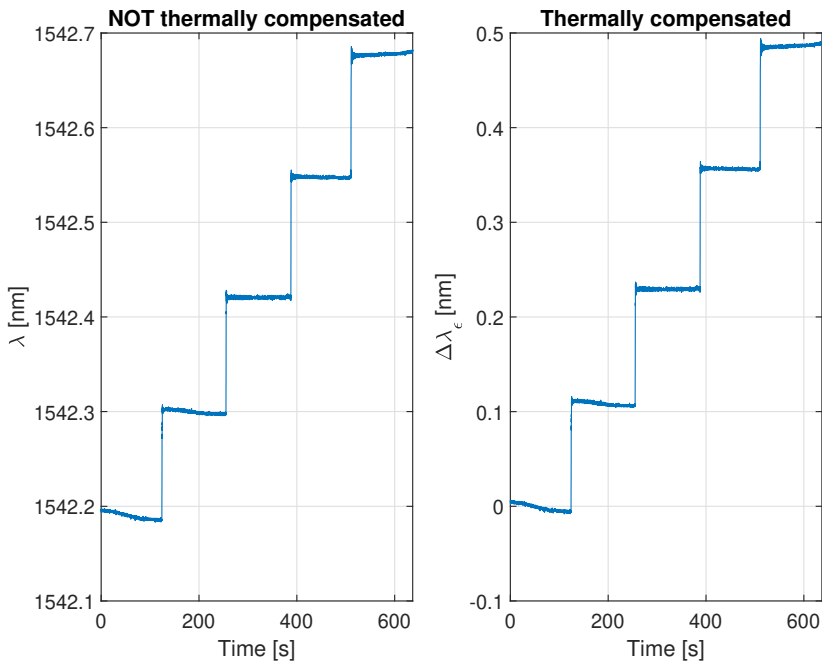


Figure 4.41: Specimen 2: Ch2Gr2 λ -time trend

The relationship between the mechanical contribution $\Delta\lambda_\epsilon$ and the strain measured by the strain gauge is shown in Figures 4.42 and 4.43 for both sensors. The data provided by a linear interpolation between those quantities has been included as a dashed straight line. A comparison between the two curves, real and interpolated, shows that no appreciable differences can be noticed. The linearity of the relationship between the two quantities is confirmed by a *Root Mean Square Error (RMSE)* of 0.2914 and 0.3016 for Ch1Gr1 and Ch2Gr2 respectively. This trend confirms the constant behaviour of K_ϵ as a function of the strain.

This characteristic justifies the introduction of the K_ϵ coefficient resulting from the linear interpolation:

$$\Delta\lambda_\epsilon = \Delta\lambda_{\epsilon,0} + K_\epsilon \cdot \Delta\epsilon \quad (4.10)$$

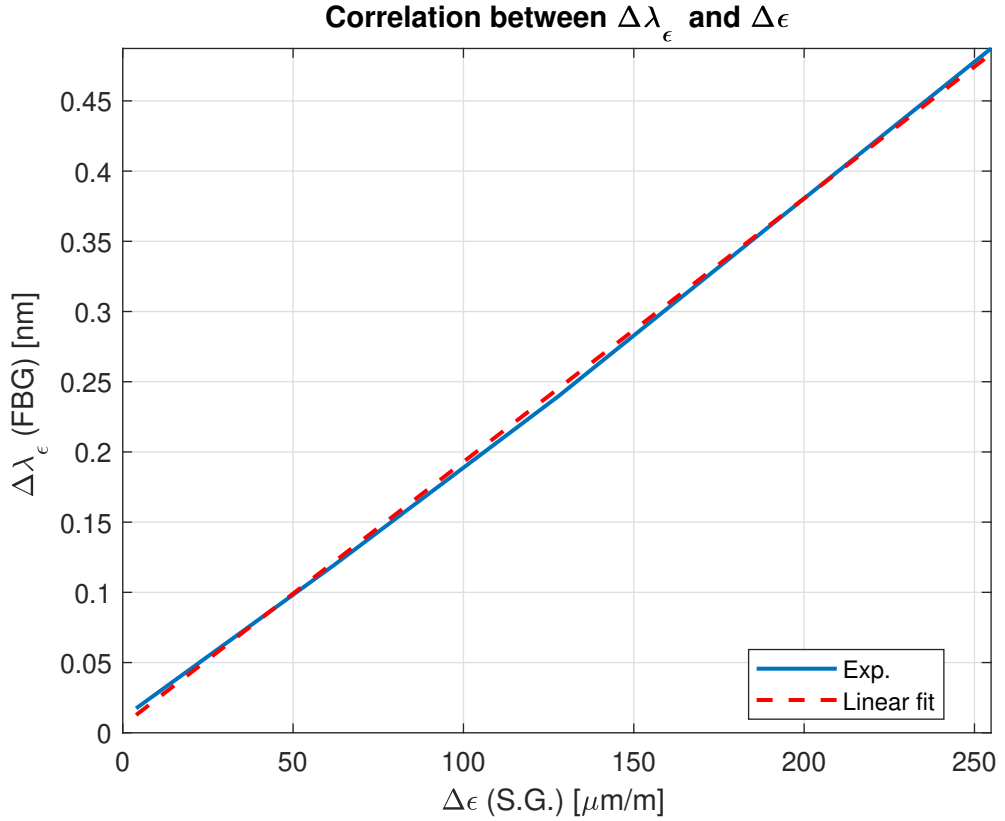


Figure 4.42: Ch1Gr1: correlation between $\Delta\lambda_\epsilon$ and $\Delta\epsilon$

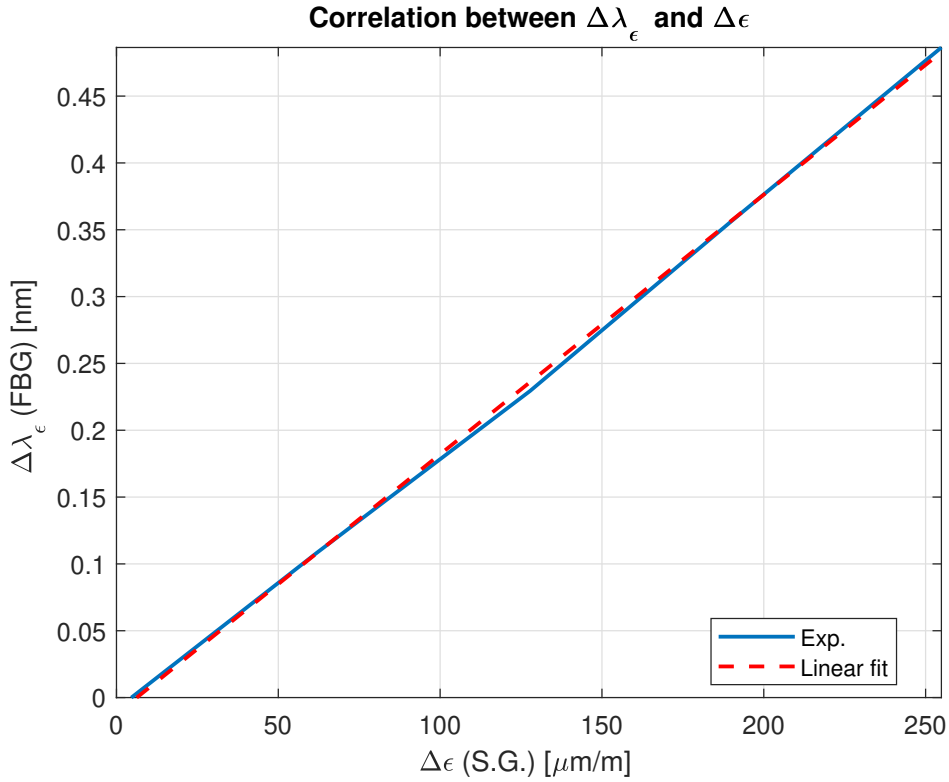


Figure 4.43: Ch2Gr2: correlation between $\Delta\lambda_\epsilon$ and $\Delta\epsilon$

The following results have been obtained:

Specimen 2		
	Ch1Gr1	Ch2Gr2
K_ϵ [nm]	1876.2032	1942.2120
$\Delta\lambda_{\epsilon,0}$ [nm]	0.0053	-0.0122

Table 4.10: Specimen 2: K_ϵ and $\Delta\lambda_{\epsilon,0}$

An analysis of the results indicates that the strain coefficient obtained for Specimen2 FBGs are greater than the value calculated for Specimen1 ($K_\epsilon = 1561$ [nm]). A difference between Channel 2 and Channel 1 can be appreciated as well, since the pre-loaded line returns a greater value compared to the simply supported one.

For the sake of clarity, the following image shows the relation between the strain coefficient and the pre-load for both specimens.

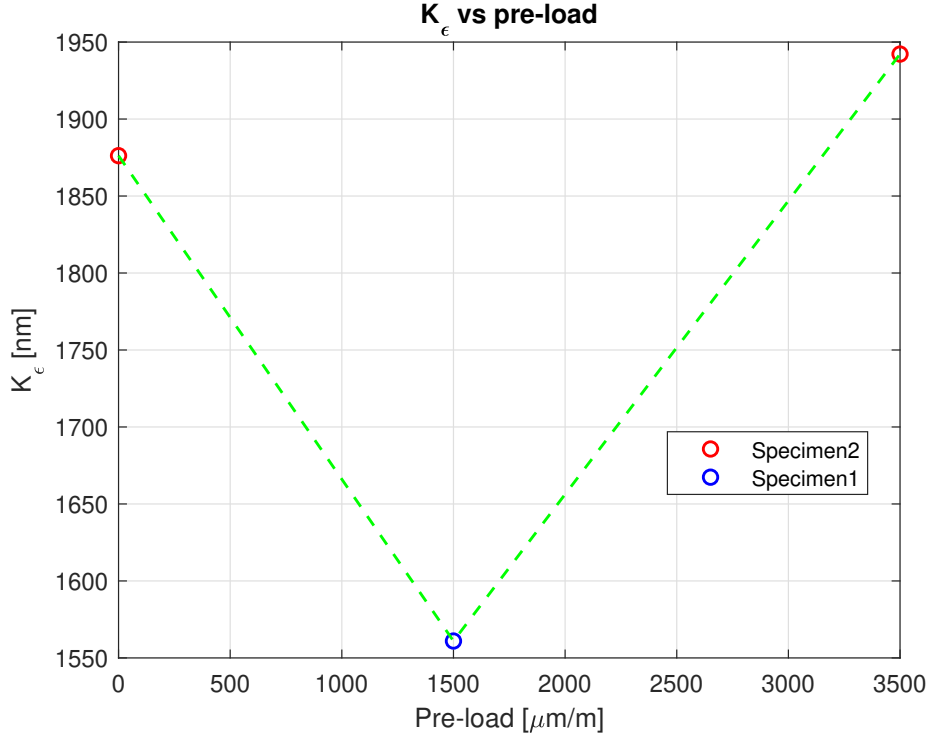


Figure 4.44: K_ϵ vs pre-load trend for both Specimens

As can be seen, the influence of the pre-load on the strain coefficient cannot be clearly identified. This unusual behaviour is surely influenced by the quality of the analysis carried out on the samples. A comparison of the RMSE for the $\Delta\lambda_\epsilon$ trend as a function of the $\Delta\epsilon$, obtained for Specimen 1 and Specimen 2, indicates that the results regarding Specimen1 are more reliable compared to Specimen 2. However, due to a lack of sufficient data to provide a valid explanation for this behavior, these features will not be further investigated.

In Figure 4.45, instead, is represented the trend between the mechanical contribution $\Delta\lambda_\epsilon$ (of each FBG), the applied load and the physical deformation $\Delta\epsilon$ sensed by the strain gauge.

These trends highlight a difference in the slope between the curves. In fact, the presence of a $K_\epsilon \neq 1$ causes a difference between the red and blue lines, while a different K_ϵ between the FBGs is the cause of the different slope of the blue lines.

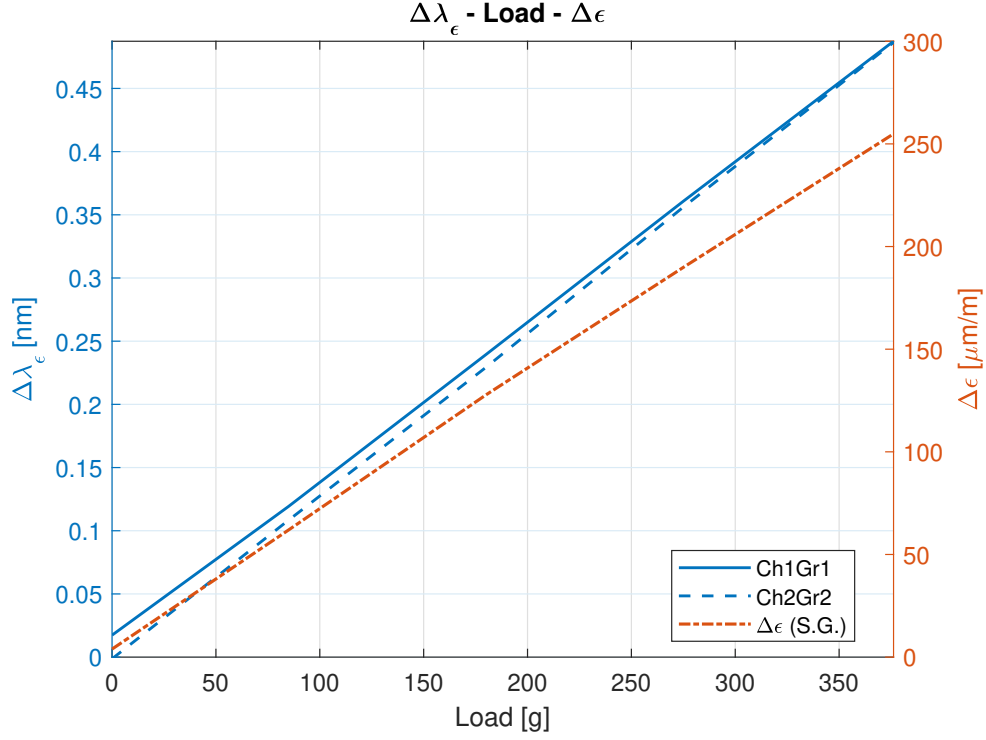


Figure 4.45: $\Delta\lambda_\epsilon$ -load- $\Delta\epsilon$ trend for Specimen2

Once the K_ϵ is known, it is possible to compute the strain measured by the FBG sensor. For this purpose, two different approaches are possible:

- 1 To calculate the deformation considering the raw value without removing the residual $\Delta\lambda_{\epsilon,0}$, so using the relation: $\Delta\epsilon = \frac{\Delta\lambda_\epsilon}{K_\epsilon}$
- 2 To calculate the deformation removing the residual $\Delta\lambda_{\epsilon,0}$, by using equation 4.7

The first strategy provides an accurate measurement of what the sensor captures, as the data is not altered in any way. However, the second approach compensates for errors that cause the presence of a residual strain and, in this way, provides an output that is more consistent with the real deformations. Even in this case, the second strategy was preferred.

A graphical comparison between the mean strain measured by the strain gauge and by the FBGs for each load steps is reported in Figure 4.46. As can be observed, the results provided by the sensors are very consistent to each other.

The average strain are also reported in the following table:

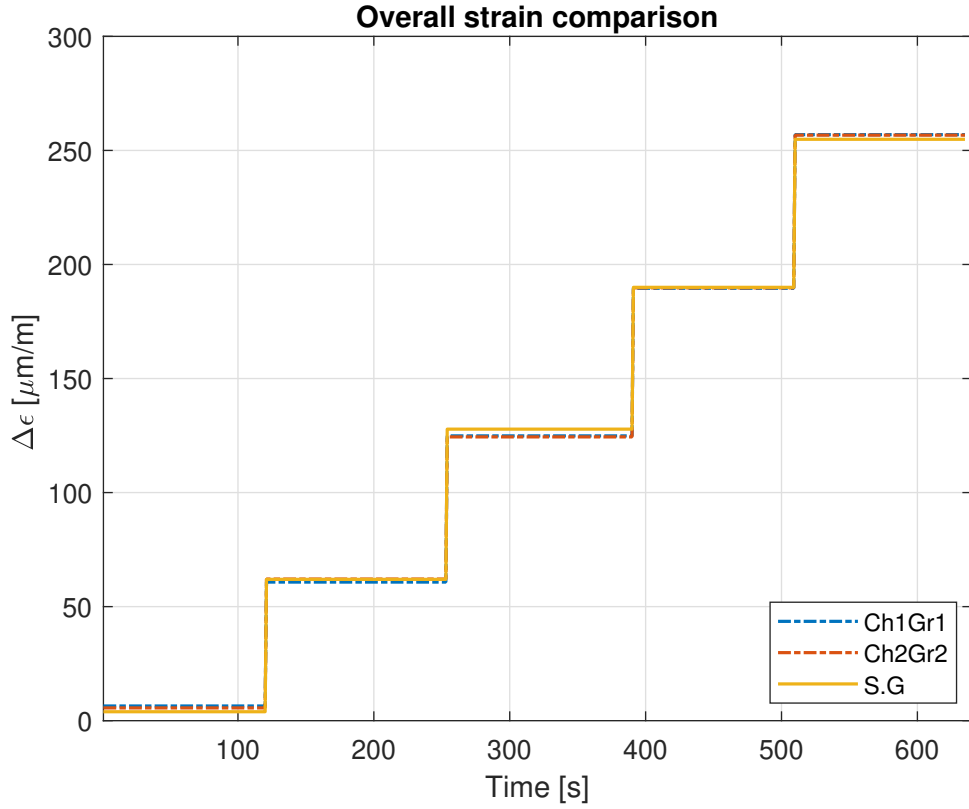


Figure 4.46: Specimen 2: overall strain comparison

Specimen 2: $\Delta\epsilon$ [$\mu\text{m}/\text{m}$]			
Load	SG	Ch1Gr1	Ch2Gr2
0g	3.9137	6.4352	5.5951
85g	61.955	60.758	62.089
180.2g	127.81	124.86	124.4
275.4g	189.98	189.57	189.76
376.4g	254.88	256.92	256.7

Table 4.11: Specimen 2: comparison between mechanical strain

These results demonstrated FBG sensors' capacity to be *mechanically calibrated* and yield strain estimates that are perfectly consistent with those of the strain gauge.

4.3.2 Bending test at variable temperature (20°C/h)

Once the K_ϵ coefficients for Ch1Gr1 and Ch2Gr2 have been obtained, it is finally possible to verify if the data elaborated are reliable enough to conduct a fully-optical and autonomous thermomechanical decoupling.

The purpose of the test is to expose Specimen 2 to 5 increasing load steps while letting the temperature vary cyclically, in order to verify if the optical sensors are able to autonomously provide the $\Delta\epsilon$ and ΔT to which they are subjected.

In order to submit the test specimen to a controlled temperature variation, it was placed inside the climatic chamber. The test setup is similar to the previous test activities and consists of the use of the optical interrogator for FBGs data acquisition, the climatic chamber, a PC for data acquisition and a SHT85 digital sensor to obtain a reference temperature value, useful for validating the results.

The specimen was clamped at one end on a 3D-printed support, and positioned inside the climatic chamber in a useful position for load application.

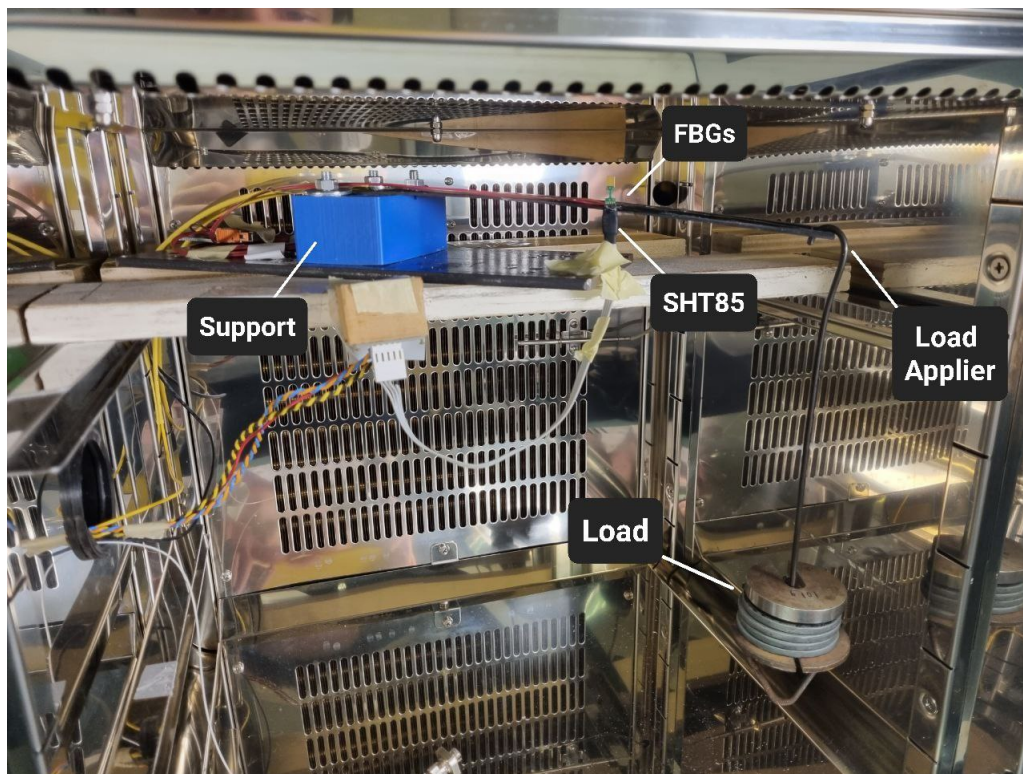


Figure 4.47: Climatic chamber setup for bending test

The test was designed so that the temperature varied by 15° for each load step and with a slope of 20°C/h. 45 minutes of acquisition was collected for each load step, for an overall duration of roughly 3h 45min. Considering that Specimen2 was successfully thermally characterised between 0°C and 40°C, a temperature range from +5°C to +35°C was chosen, as well as the same rate of change of 20°C/h. The load steps were: 0, 85, 180.2, 275.4, 376.4 [g], each applied close to the shear centre in order to lead a pure-bending in the specimen, which was oriented to induce a tensile stress on the optical line.

The time evolution of temperature and loads is shown below:

Static bending test - 20°C/h		
Load [g]	Temperature [°C]	Duration [min]
0	20 → 35	45
85	35 → 20	45
180.2	20 → 5	45
275.4	5 → 20	45
376.4	20 → 35	45

Table 4.12: Characteristics of Specimen 1 bending test (20°/h)

In Figure 4.48 are plotted the time-evolution of: the ratio of the measured wavelength to their average value for both FBGs (blue) and the temperature measured by the SHT85 (red), while in Figure 4.49 the same wavelength-ratio evolution (blue) is correlated with the load steps (red).

A detailed explanation of the wavelength time-evolution as a function of load and temperature can be found at 4.1.3 and 4.2.2.

Thermomechanical decoupling results

In order to obtain the ΔT and $\Delta \varepsilon$ to which Ch1Gr1 and Ch2Gr2 were subjected, the linear system 4.8 has been solved.

$$\begin{Bmatrix} \Delta \lambda_1 \\ \Delta \lambda_2 \end{Bmatrix} = \begin{bmatrix} K_{\varepsilon_1} & K_{T_1} \\ K_{\varepsilon_2} & K_{T_2} \end{bmatrix} \cdot \begin{Bmatrix} \Delta \varepsilon \\ \Delta T \end{Bmatrix}$$

Where:

$$\Delta \lambda_{1,2} = \lambda_{m_{1,2}} - \lambda_{0_{1,2}}$$

and subscripts 1 and 2 refers to Ch1Gr1 and Ch2Gr2, respectively.

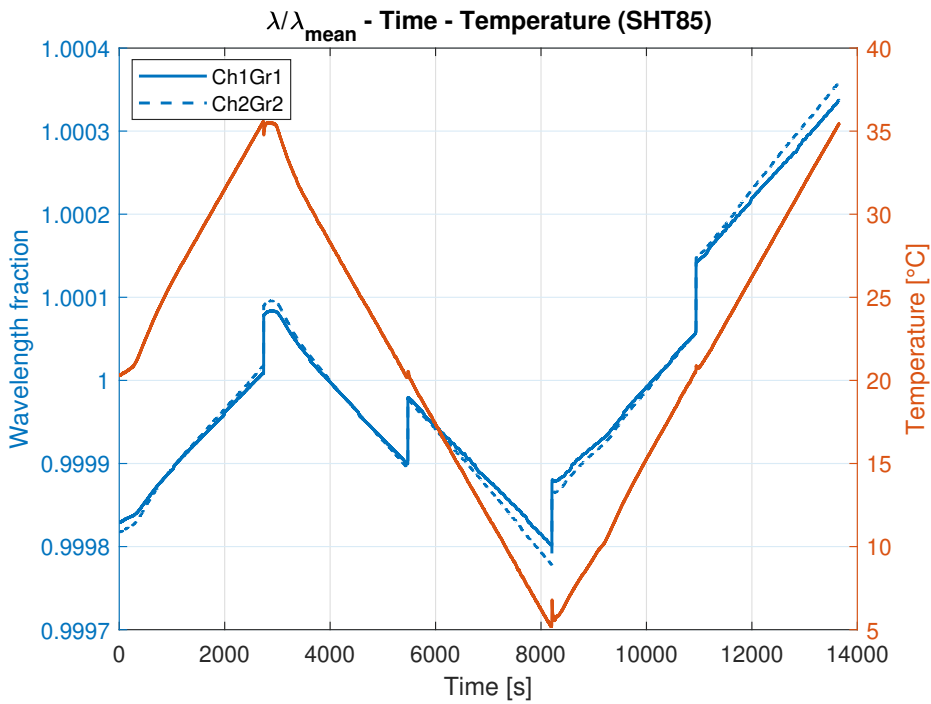


Figure 4.48: λ/λ_{mean} - time - temperature evolution

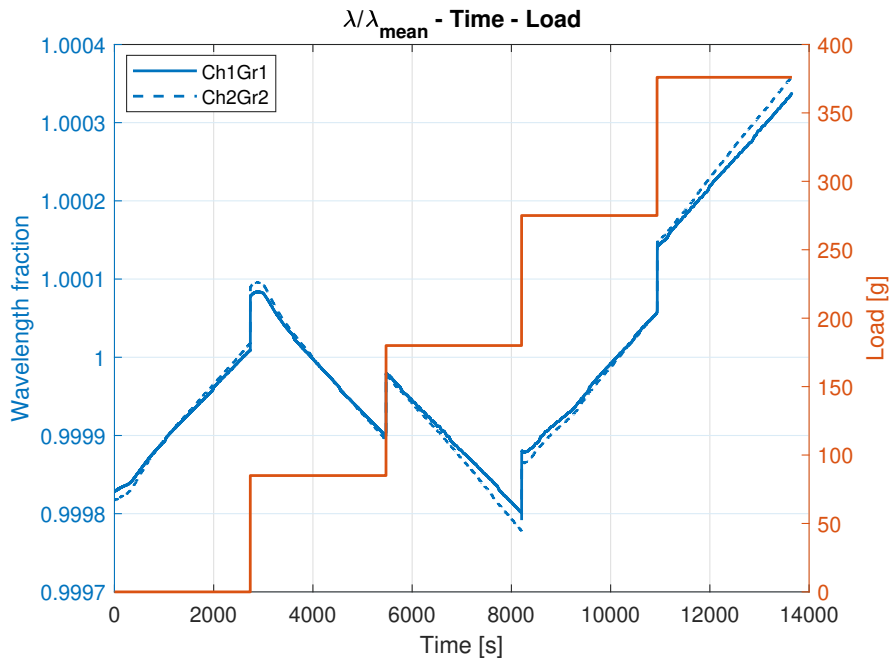


Figure 4.49: λ/λ_{mean} - time - load evolution

In Figure 4.50 is shown the time-evolution of the reference temperature (SHT85) and the one resulting from the resolution of the linear system.

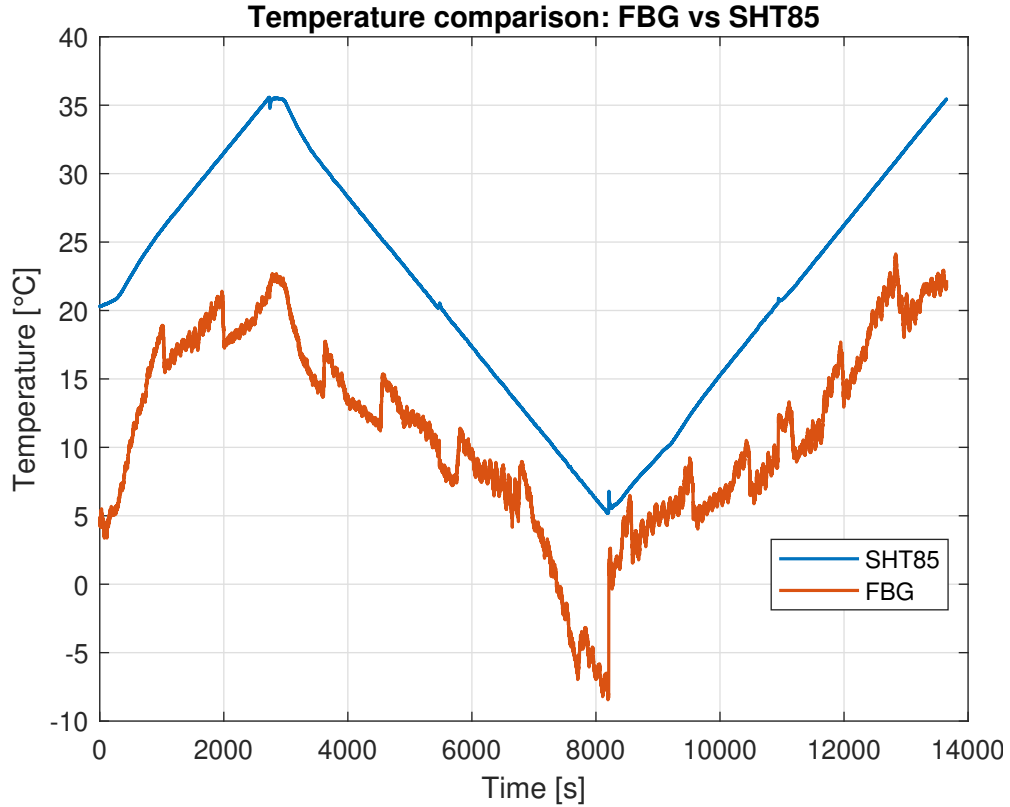


Figure 4.50: Temperature comparison: FBGs vs SHT85

As can be seen the results are characterized by a very high degree of inaccuracy, as confirmed by *Root Mean Square Error (RMSE)* of 11.0309 between the trends.

The same conclusions can be extended to the mechanical strain, whose time-trend is reported in Figure 4.51, including the load-evolution as well.

By limiting to the analysis of the results obtained, it would be concluded that the thermal decoupling strategy based on an optical-only system is not able to guarantee proper decoupling between the two phenomena.

However, it must be noted that what has been obtained is affected by an overlapping of errors of a different nature. In fact, starting from the thermal characterisation, a degradation in the quality of the results provided by the FBGs of Specimen2, compared to those of Specimen1, was highlighted, and inevitably it

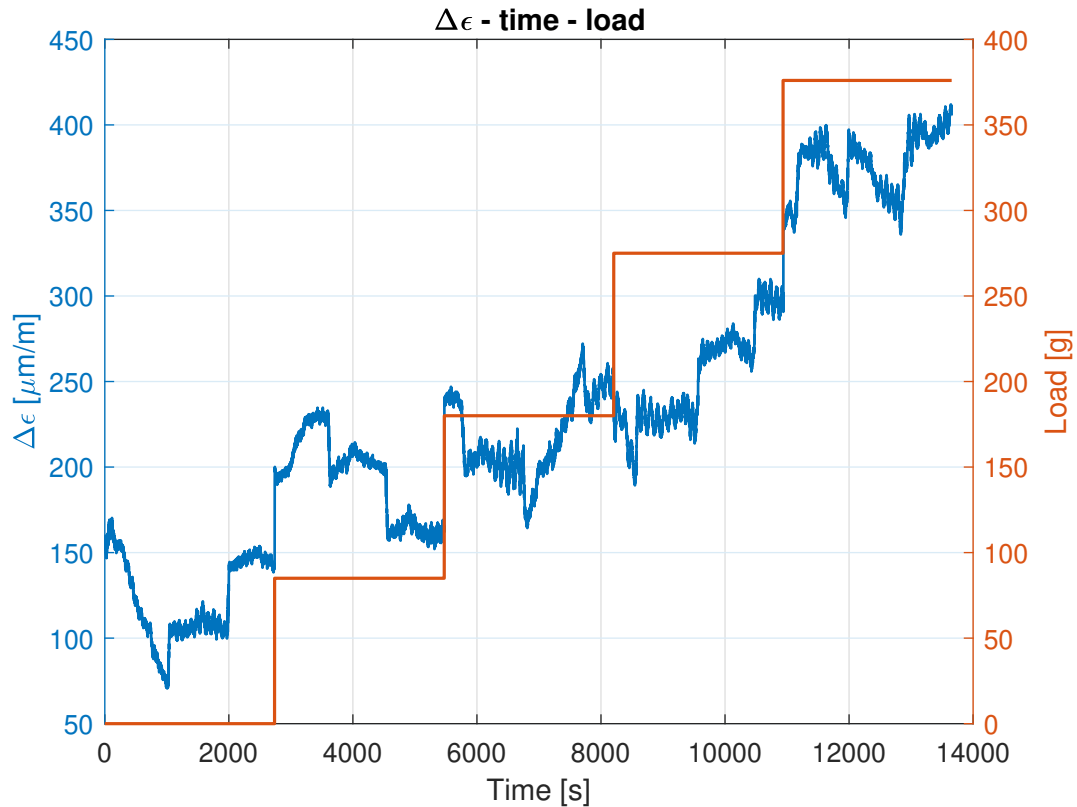


Figure 4.51: FBGs mechanical strain time-evolution

influenced the determination of the strain coefficients. Therefore, since the linear system 4.8 is deeply dependent on the K_ϵ and K_T coefficients, it leads to consequently unreliable results.

With a bit of imagination, however, it can be seen that the trends shown in the previous figures, although evidently different from the expected ones, show a temporal evolution that vaguely resembles the actual trend. In fact, the temperature trend slightly reminds SHT85's one, and, likewise, the temporal evolution of the mechanical strain follows an overall increasing trend, as generally does the applied load one.

Based on these considerations, it is believed that the thermomechanical decoupling strategy relying only to a single optical system, may be able to guarantee a correct decoupling between the thermal and mechanical phenomena, but at the same time needs a high accuracy in determining the temperature and strain coefficients. Therefore, a new purely-optical configuration should be developed with the aim of minimising the margin of error and demonstrating the feasibility of this approach.

Chapter 5

Conclusions

The results achieved in this thesis have enabled the validation of a thermomechanical decoupling methodology that can guarantee a concrete implementation possibility of FBG sensors on composite material structures. The presented solutions succeeded in decoupling thermal and mechanical phenomena, either through the use of a mix of optical and digital sensors, or through exclusively optical sensors. Depending on the type of application, the diversity of the proposed approaches allows a high degree of flexibility and the possibility of choosing the sensor configuration that best suits to the needs.

In particular, an optical-digital system (4.1) is the easiest approach to implement, and guarantees excellent results in terms of decoupling . Similarly, it has been verified that a system composed exclusively of optical sensors mounted on two mechanically-decoupled structures, one of which is not subject to mechanical deformation, can also lead to excellent results (4.2). The last system (4.3), on the other hand, which is completely optical and installed on a single structure, was not able to provide sufficiently reliable results. The cause of these anomalies is attributable to the low quality of the results of the related thermal characterisation and mechanical calibration procedures. Therefore, it is evident that as we move towards greater independence from non-optical sensors and as the degree of integration between sensors and the structure increases, a greater accuracy is required in FBG characterisation operations.

Although the proposed approach presents many benefits, it has its own limitations. In fact, since it refers to sensors which are installed on structures, it is necessary to carry out thermal characterisation and mechanical calibration steps. Even though these are simple procedures, they would become a major limitation if numerous sensors were considered or if these were deeply integrated into structures.

5.1 Possible improvements and future works

5.1.1 A new fully-optical system

A possible improvement concerns the fully-autonomous optical system (4.3). In fact, to verify if the lack of accuracy of the results is only dependent on Specimen2 (i.e. the sample considered for the analysis), a new optical system is proposed below.

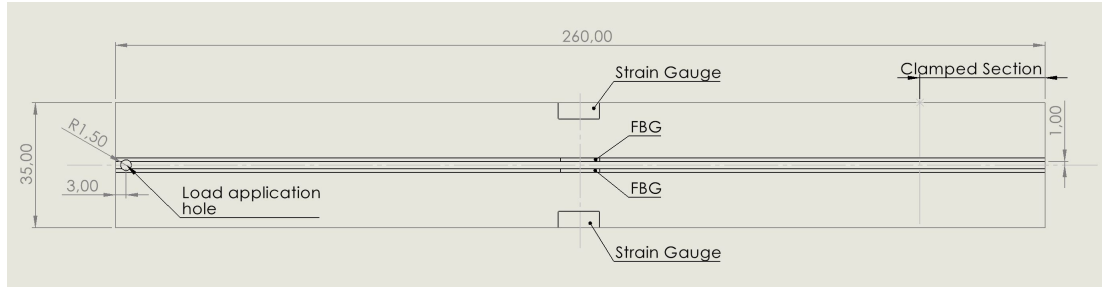


Figure 5.1: Fully-optical system improvement

The sample shares the same geometrical characteristics of the previous Specimen 1 and 2 (but it is not required) and is equipped with 2 optical lines, with an optical sensor for each line, and with 2 strain gauges. Those sensors are positioned at mid sample-length, and the optical lines are very close to each other and both 1 mm-spaced from the symmetry axis. The aim of positioning those lines so close to each other offers the possibility to cover both of them with a unique layer of epoxy resin. Furthermore, by placing the FBGs very close together along the sample width, by applying a not pure-bending load, the difference in the strain perceived by the sensors would be minimized and the results of the 4.8 linear system consequently improved.

The presence of the strain gauges is required to determine the deformation to which the optical sensors are subjected, and, then, determining the strain coefficients. They could be placed close to the two edges of the specimen in order to determine the deformation at the ends, and reconstructing its trend along the entire section. All the sensors, FBGs and strain gauges, must be placed in the same position along the length of the specimen.

5.1.2 An improved mechanical calibration phase

A further improvement concerns the mechanical calibration phase. This procedure is of central importance but at the same time it could represent a great limitation due to the constraint of installing as many strain gauges as optical sensors.

A possible improvement consists in carrying out this procedure without using physical sensors, but, instead, a finite-element model of the structure by means of which determining the state of deformation where the sensors are located. By doing so, the experimental determination of the K_ε coefficient and thus the entire process would become significantly simpler and faster to implement.

Appendix A

Arduino - SHT85 temperature sketch

Here follows the Arduino UNO sketch which allows to measure the temperature from the SHT85 sensor and print it to the serial monitor. The acquisition time length must be set as well as the intervals between the measures.

```
1 #include <Wire.h>
2 #include "SHTSensor.h"
3 SHTSensor sht;
4
5 // To use a specific sensor instead of probing the ...
6 // bus use this command:
7 // SHTSensor sht(SHTSensor::SHT3X);
8
9 void setup() {
10     Wire.begin();
11     Serial.begin(9600);
12     delay(1000); // let serial ...
13     console settle
14
15     if (sht.init()) {
16         //Serial.print("init(): Tutto ok!\n"); //Il ...
17         //sensore funziona/ i collegamenti sono ok
18     } else {
```

```
18     Serial.print("init(): Errore sensore! ...  
        Controllare i collegamenti e/o lo stato di ...  
        salute del sensore.\n");  
19 }  
20  
21  
22     sht.setAccuracy(SHTSensor::SHT_ACCURACY_MEDIUM); ...  
        // only supported by SHT3x  
23 }  
24  
25  
26 int durata=600; //This value must be set manually. ...  
    It represents the duration of the measurement, ...  
    in second  
27  
28  
29 int misurazione=1; //Control variable to stop the ...  
    program  
30  
31 int t=0; //Initialising the time  
32 String Tempo="t: ";  
33 String Temp="Temp: ";  
34 void loop() {  
35  
36         if(!misurazione){ //If I ...  
            have reached the ...  
            predetermined duration ...  
            then I interrupt the ...  
            programme.  
37         return;  
38         }  
39     if (sht.readSample()) {  
40         /*Serial.print("  Hum: "); //This is a comment. ...  
            Humidity is not a required output  
41         Serial.print(sht.getHumidity(), 2);  
42         Serial.print("\n"); */  
43  
44         Serial.print(sht.getTemperature(), 2);  
45         Serial.print("\n");  
46         t++;
```

```
47 } else {
48   Serial.print("Errore di lettura\n");
49 }
50 if (t>durata){ //If I have reached the ...
    predetermined duration then:
51   //Serial.print("Fine misurazione! \n");
52   misurazione=0;
53 }
54
55 delay(1000); // Intervals between the measure ...
    (1000 ms)
56 }
```


Appendix B

Thermomechanical decoupling using an inaccurate thermal characterization

The effects of the thermal characterization on the thermomechanical decoupling are discussed in this chapter. The results refer to the system presented in 4.2, based on two optical system mechanically independent each other.

This thermal characterization was carried out as a first attempt to determine the K_T and λ_0 coefficient for Specimen2, in order to employ it as a temperature sensor for the next variable-temperature load test.

The activity was executed according to the usual steps:

- Setting up Specimen 2 on a flat surface inside the climatic chamber
- Connecting the FBGs with the SmartScan
- Positioning the SHT85 sensor in close proximity to the FBGs, in order to capture as accurately as possible the same temperature perceived by the optical sensors
- Setting the temperature interval in the climatic chamber and its rate of change ($^{\circ}\text{C}/\text{h}$)
- Simultaneous start of the climate chamber cycle and the acquisition of the temperature and the FBG wavelengths
- End of acquisitions and temperature cycle
- Data storage and post-processing

The climatic chamber setup is shown below:

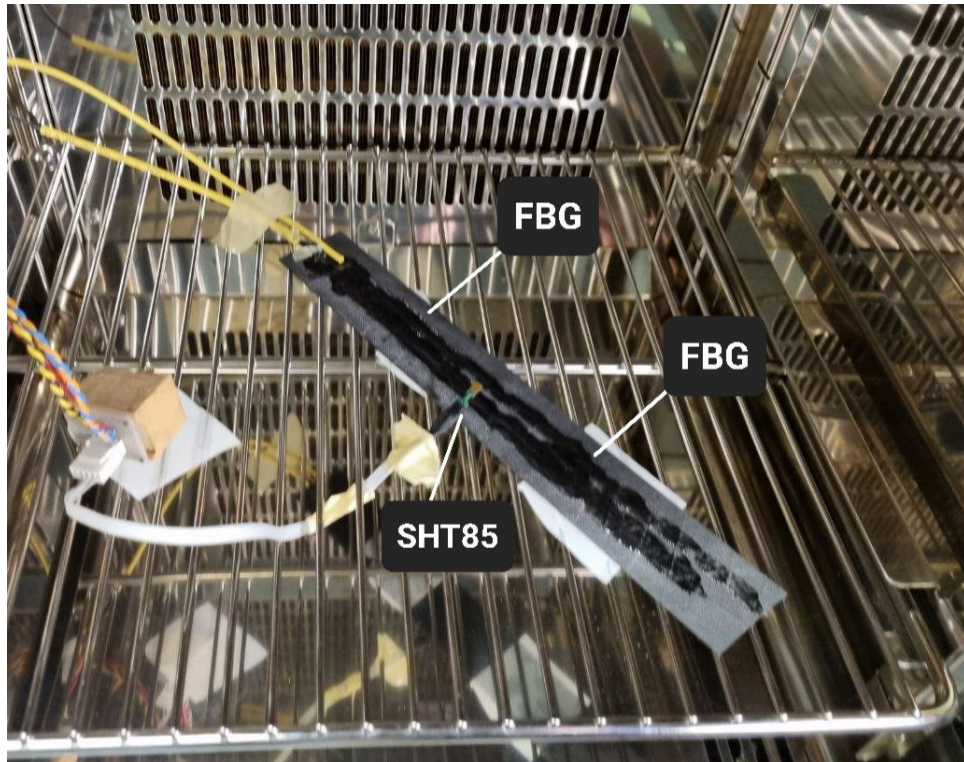


Figure B.1: Specimen 2 setup for thermal characterization

Since the previous activity regarding Specimen1 provided good results and was conducted within a temperature interval of $[-40 +40]$ °C, the same temperature range was adopted for Specimen2, using a rate of change of 30°C/h. The FBGs numbering is the same as in section 4.2.1.

In Figure B.2 is represented the λ -Temperature trend for Channel 1, and a linear fit is included as well. As can be observed, a not-perfectly linear behaviour characterises the correlation between the two quantities. Nevertheless, a *Root Mean Square Error (RMSE)* of 0.0304 and 0.0185 for Ch1Gr1 and Ch1Gr2 respectively, confirms an overall good quality of the fit.

Almost the same conclusions can be extended to the λ -Temperature trend for the FBGs on Channel2, which is shown in Figure B.3. In this case, a *Root Mean Square Error (RMSE)* of 0.0131 and 0.0251 for Ch2Gr1 and Ch2Gr2 respectively is obtained. A great deviation from the linear trend occurs near the upper and lower temperature limits, i.e. -40°C and +40°C. The better overall results are related to the pre-loaded optical line.

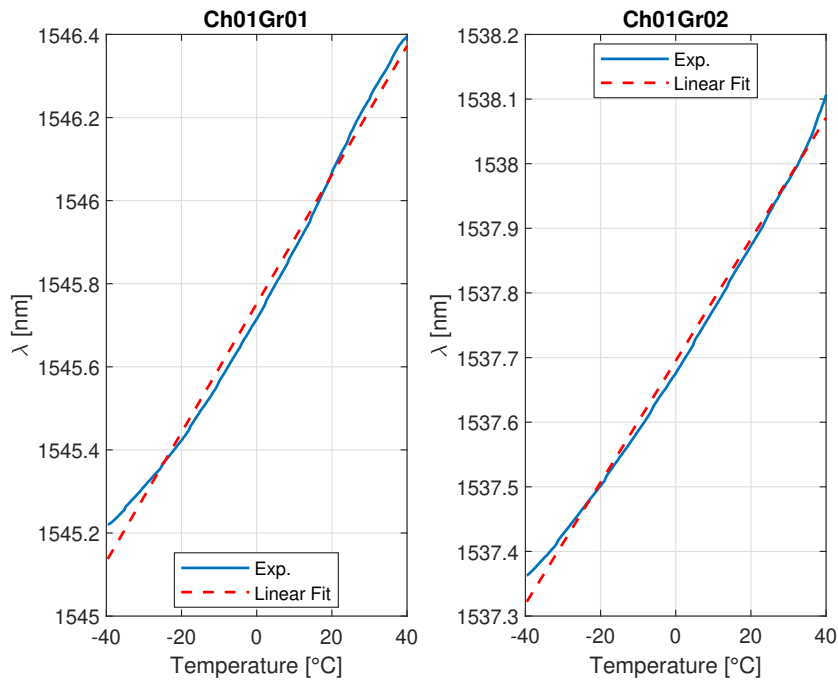


Figure B.2: Specimen2 Channel 1 λ -Temperature

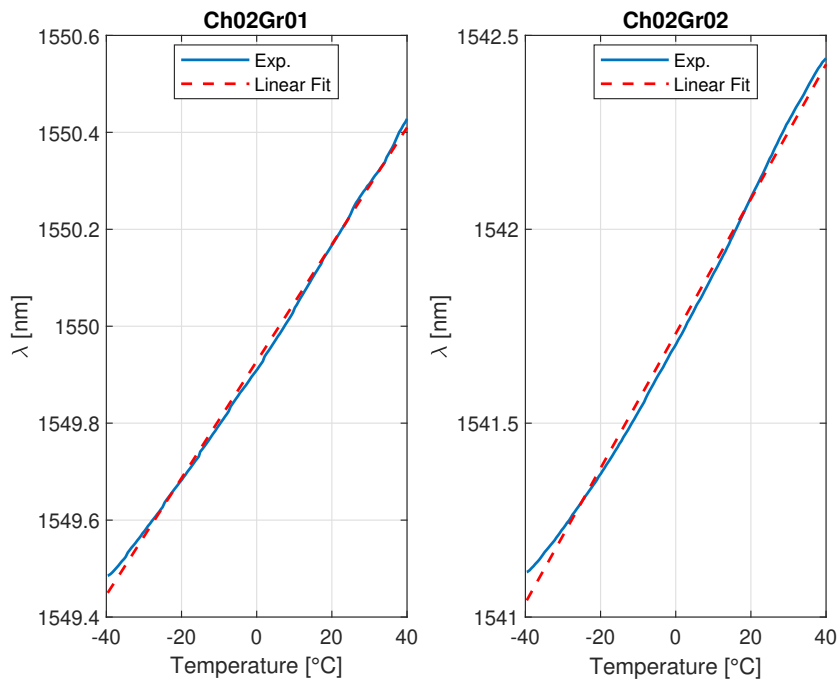


Figure B.3: Specimen2 Channel 2 λ -Temperature

Linear interpolation leads to the following results:

Specimen 2: T.C. [-40 40]°C				
	Ch1Gr1	Ch1Gr2	Ch2Gr1	Ch2Gr2
K_T	0.0155	0.0094	0.0121	0.0174
λ_0 [nm]	1545.75	1537.69	1549.93	1541.73

Table B.1: Specimen 2: T.C. [-40 40]°C

Finally, it is possible to estimate the temperature perceived by the FBG as:

$$T = \frac{\lambda_m - \lambda_0}{K_T}$$

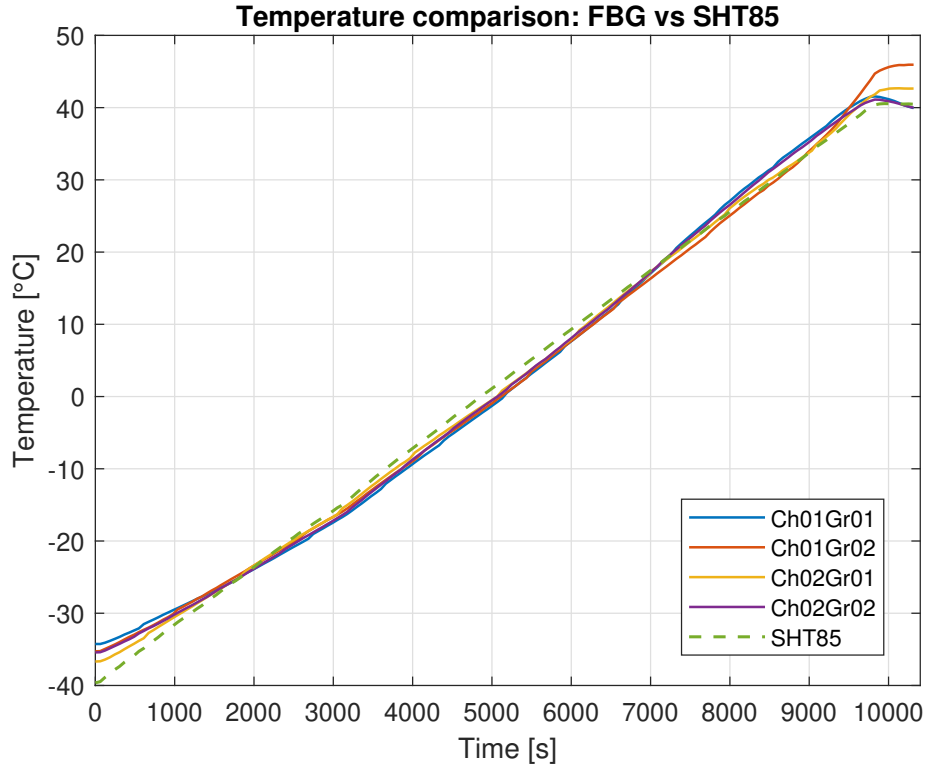


Figure B.4: Specimen2 SHT85 vs FBG

A graphical comparison between the temperature perceived by the FBGs and measured by the SHT85 is shown in Figure B.4. The graphical evolution of the FBGs-related quantities is affected by the quality of the linear interpolation. Even

in this case the major differences with the real value given by the SHT85, occurs close to the upper and lower temperature limits.

Now the results related to the variable-temperature load-test are presented. The load test is exactly the same as 4.2.2 so its structure is not re-discussed here.

In Figure B.5 a comparison between the reference SHT85 temperature value and the FBGs sensed one is reported.

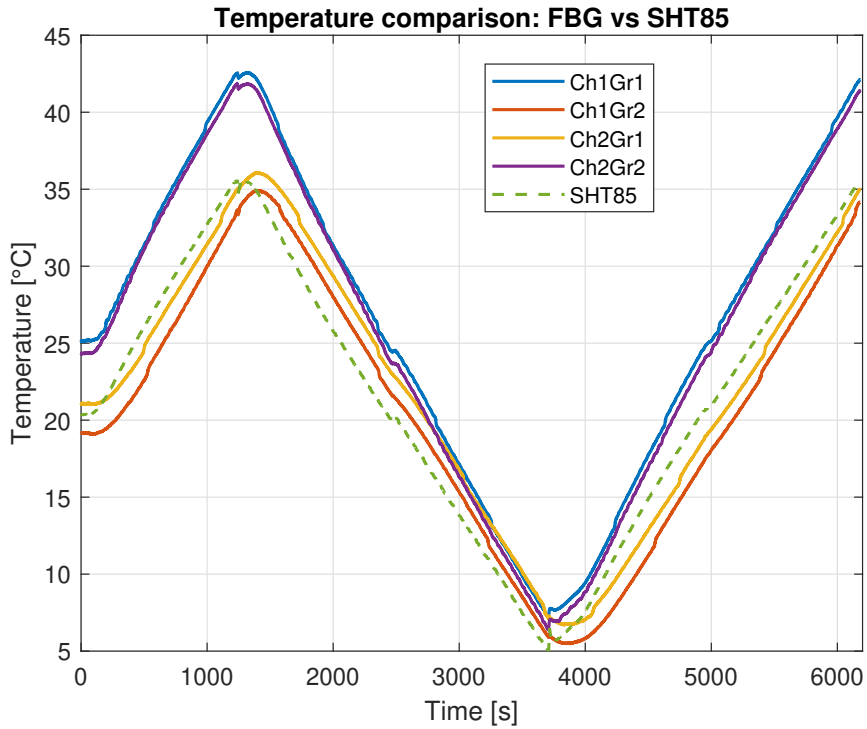


Figure B.5: Temperature comparison: FBGs vs SHT85

Temperature comparison				
	Ch1Gr1	Ch1Gr2	Ch2Gr1	Ch2Gr2
RMSE	4.8402	2.3515	2.1102	4.2765

Table B.2: Temperature comparison: RMSE

An estimation of the quality of the results is given by the *Root Mean Square Error (RMSE)* which is reported in Table B.2.

Then, the results of the thermal compensation using all the 4 FBGs are shown:

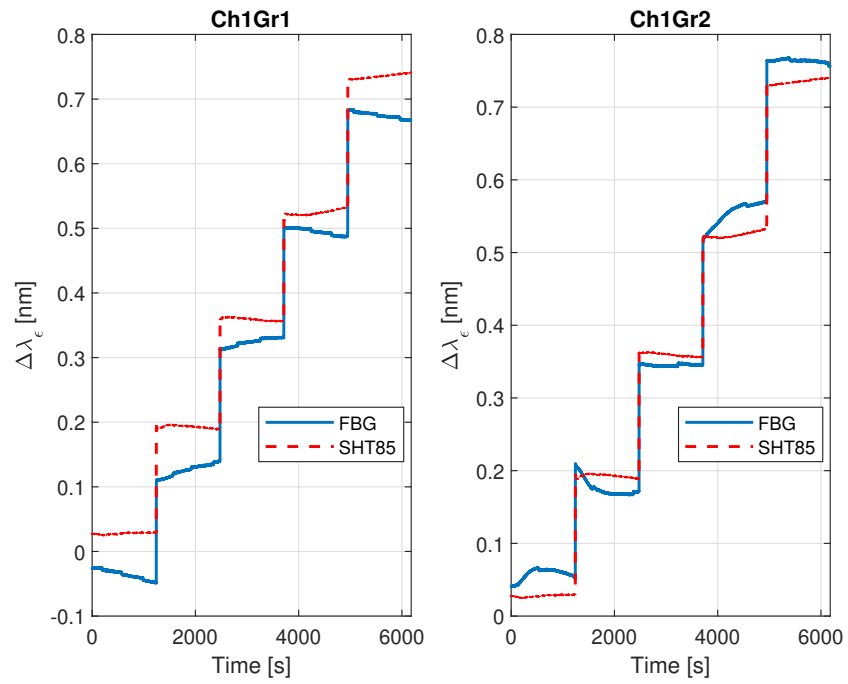


Figure B.6: Thermal compensation: channel 1

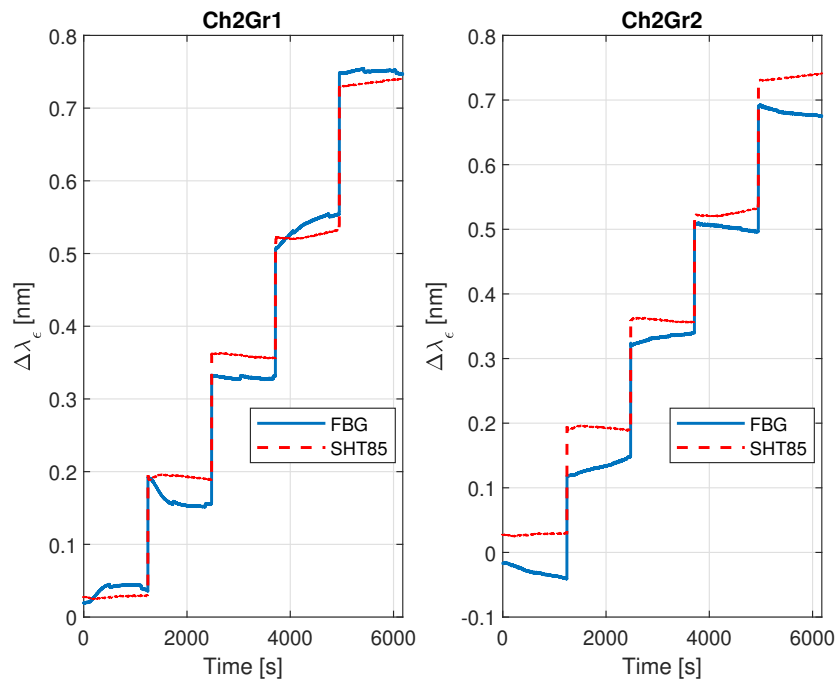


Figure B.7: Thermal compensation: channel 2

In Figures B.6 and B.7 the time evolution of the mechanical contribution is reported and compared with the reference value that could have been obtained using the temperature acquired by the SHT85.

As can be seen, none of the FBGs is able to provide a reliable temperature measure, and so none of them can be used to determine the mechanical contribution $\Delta\lambda_\epsilon$ in an accurate way. By comparing this results with the one presented in 4.2.2, it is clear the importance of conducting a good thermal characterization in order to obtain reliable responses.

Bibliography

- [1] P. Maggiore A. Aimasso M.D.L. Dalla Vedova and G. Quattrocchi. “Study of FBG-based optical sensors for thermal measurements in aerospace applications”. In: (XXIX A.I.VE.LA. National Meeting, Dec. 2021) (page 10).
- [2] Matteo Dalla Vedova, Pier Berri, and Alessandro Aimasso. “Environmental Sensitivity of Fiber Bragg Grating Sensors for Aerospace Prognostics”. In: Sept. 2021. DOI: 10.3850/978-981-18-2016-8_634-cd (page 12).
- [3] Cristian Secci. "*Monitoraggio strutturale con sensori Fibre Bragg Grating*". Master Thesis. December 2019 (page 14).
- [4] Marco Bertucelli. "*Monitoraggio termico con sensori Fiber Bragg Grating*". Master Thesis. December 2021 (pages 4, 5).
- [5] Giuseppe Francesco Impicciatore. "*Implementazione di sensori FBG per il monitoraggio strutturale di un velivolo sperimentale*". Master Thesis. December 2021 (pages 4, 5, 17).
- [6] Zhen Ma and Xiyuan Chen. “Fiber Bragg Gratings Sensors for Aircraft Wing Shape Measurement: Recent Applications and Technical Analysis”. In: (2019). URL: <https://www.mdpi.com/1424-8220/19/1/55> (page 8).
- [7] Minh Song, Sang Bae Lee, Sang Sam Choi, and Byoung-ho Lee. “Simultaneous Measurement of Temperature and Strain Using Two Fiber Bragg Gratings Embedded in a Glass Tube”. In: *Optical Fiber Technology* 3.2 (1997), pp. 194–196. ISSN: 1068-5200. DOI: <https://doi.org/10.1006/ofte.1997.0215>. URL: <https://www.sciencedirect.com/science/article/pii/S1068520097902157> (page 12).
- [8] R Montanini and L D’Acquisto. “Simultaneous measurement of temperature and strain in glass fiber/epoxy composites by embedded fiber optic sensors: I. Cure monitoring”. In: *Smart Materials and Structures* 16.5 (Aug. 2007), pp. 1718–1726. DOI: 10.1088/0964-1726/16/5/026. URL: <https://doi.org/10.1088/0964-1726/16/5/026> (page 13).
- [9] Y. Hattori. “Temperature compensation technique for fibre Bragg gratings using liquid crystalline polymer tubes”. English. In: *Electronics Letters* 33 (5

BIBLIOGRAPHY

- Feb. 1997), 417–419(2). ISSN: 0013-5194. URL: https://digital-library.theiet.org/content/journals/10.1049/el_19970289 (page 14).
- [10] Whitten L. Schulz, Eric Udd, John M. Seim, and Galen E. McGill. “Advanced fiber-grating strain sensor systems for bridges, structures, and highways”. In: *Smart Structures and Materials 1998: Smart Systems for Bridges, Structures, and Highways*. Ed. by S.-C. Liu. Vol. 3325. International Society for Optics and Photonics. SPIE, 1998, pp. 212–221. DOI: 10.1117/12.310610. URL: <https://doi.org/10.1117/12.310610> (page 14).

Sitography

- [11] URL: <https://val-center.com/en/product/climatic-chamber-kambic-kk-50-chlt> (page 22).
- [12] URL: <https://create.arduino.cc/projecthub/sd9martins/sht85-arduino-temperature-and-humidity-sensor-6e727d> (page 23).
- [13] URL: <https://www.smartfibres.com/products/smartsan> (pages 24-26).
- [14] URL: <https://it.rs-online.com/web/p/estensimetri/2236464> (page 49).